ANUL XLV **2000**

S T U D I A
UNIVERSITATIS BABEŞ-BOLYAI
PHYSICA
2

Editorial Office: 3400 CLUJ-NAPOCA, Gh. Bilaşcu no. 24 ♦ Phone:064-40.53.52

SUMAR - CONTENTS

STUDIA UNIVERSITATIS BABEŞ-BOLYAI, PHYSICA, XLV, 2, 2000

SPARK AND GLOW DISCHARGE ATOMIC EMISSION SPECTROMETRY– NONDESTRUCTIVE METHODS FOR SOLID SAMPLES ANALYSIS

S. D. ANGHEL[1], A. SIMON[1], T. FRENTIU[1], E. A. CORDOS[2]

***ABSTRACT*.** This paper presents the analytical results obtained by nondestructive analysis of steel samples via spark atomic emission spectrometry and glow discharge atomic emission spectrometry. The analytical results were obtained using as reference standards low–alloyed steel and steel samples with unknown concentrations of elements. The following elements were analyzed: C, Mn, S, P, S, Cr, Mo, Ni, Cu and V. The analytical results obtained were statistically compared using the "t" test and linear regression. The degrees of recovery are in the range of 94 ± 6–122 ± 6 % and the relative standard deviations (RSDs) are in the range of 0.88–9.10 % when the glow discharge source was used. In the case of the spark source, the degrees of recovery are in the range of 95 ± 6–125 ± 11 %, while RSDs are in the range of 1.11–10.61 %. The analytical results are not significantly different between the two methods.

Introduction

Many samples, which must be analyzed in chemical laboratories, occur naturally in solid state. The elemental spectrochemical analysis of these samples can be achieved by two techniques: indirect and direct analysis. In the case of indirect analysis the solid samples are usually dissolved in acids and then pneumatically nebulized and introduced into the spectral source. The potential disadvantages for the indirect procedure includes incomplete dissolution of the sample, precipitation of insoluble analytes, loss of the volatile analytes in during heating, contamination of the sample in during preparation. Also, the sample preparation is the most time-consuming step and necessitates high-purity reagents. Many of these

[1] Faculty of Physics, Babes–Bolyai University, M. Kogalniceanu 1, 3400 Cluj, ROMANIA
[2] Faculty of Chemistry, Babes–Bolyai University, Arany J. 11, 3400 Cluj, ROMANIA

disadvantages are substantially reduced when the solid samples are directly analyzed. Also, the direct analysis of solid samples allows: the improvement of the detection limits, analysis of microsamples, the surface analysis for lateral distribution of elements and depth gradients analysis for comparing surface and bulk constituents.

Without any doubt, the most important advantage of the direct sampling is separation and independently optimization of sample vaporization, atomization and excitation steps. The direct techniques may be divided in two groups: 1) direct insertion of samples into the plasma and 2) methods that convert solid samples into an aerosol or a vapour, which then are transported into the plasma. In the first category can be included: arc and spark sources [1], direct insertion of the sample on the support graphite or tungsten rod into the inductively coupled plasma (ICP) [2], capacitively coupled radiofrequency plasma (r.f.CCP) [3], capacitively microwave plasma (CMP) [4]. The sample is thermally vaporized through heating by the plasma and the atoms are excited into the same plasma. In the second category, the "in situ" ICP laser ablation can be included [5]. In this method a solid sample is placed in the torch, just below the plasma "fireball". When a laser beam is focused onto the surface of the sample, an atomic vapor cloud is generated which is then excited into the plasma. As a consequence, the sample transport efficiency into the plasma is virtually 100 %, yielding an extremely intense but very brief signal. In all these techniques the signal is detected by atomic emission spectrometry (AES) or mass spectrometry (MS).

The second category of methods are combining nondestructive methods: arc and spark ablation with excitation in ICP (arc/spark ablation–ICP-AES) [6–8], laser ablation with ICP–AES or ICP–MS (LA–ICP–AES, LA–ICP–MS) [9–11] and glow discharge atomic emission spectrometry or mass spectrometry (GD–AES and GD–MS) [12–15]. These techniques could be used for the characterization of surface and depth concentration gradients, which are very important aspects of the concentration of natural and manufactured materials.

Other nondestructive methods for the study of surfaces are: secondary ion mass spectrometry (SIMS) [16, 17], laser microprobe mass analysis (LAMMA), electron spectroscopy for chemical analysis (ESCA) and Auger electron spectroscopy [18–20].

In this paper, two representative methods for nondestructive analysis of steel samples are presented: spark–AES and GD–AES. Both methods are based on the sample vaporization at surface, but by different mechanism, followed by atomic excitation in an Ar plasma obtained at atmospheric (spark) or reduced (GD) pressure.

Experimental

Reference standard of low-alloyed steel samples

The calibration curves were obtained using as reference standard low-alloyed steels (ICEM 103, ICEM 104, ICEM 107 and ICEM 108 (manufactured by Institute of Metrology Bucharest) and BS 51 E, BS 53 E, BS 55 E, BS 56 E, BS 57 E, BS 52 D, BS 54 C, BS 59 B, BS 62 B and BS 64 B (manufactured by Brammer Standard Company USA). For the statistical characterization of the results, the reference standard low-alloyed steel (ICEM 102) and steel samples with unknown concentration were used. The concentration range for the reference standard of low-alloyed steels is: 0.045–1.070 % C; 0.370–2.370 % Mn; 0.050–1.620 % Si; 0.006–0.067 % P; 0.006–0.038 % S; 0.014–1.650 % Cr; 0.006–0.980 % Mo; 0.017–3.200 % Ni; 0.016–0.450 % Cu and 0.020–0.590 % V.

Instrumentation

The experimental determinations were made using two simultaneous spectrometers: Quantometer ARL 34000 (ARL Switzerland) and LECO GDS–1000 (LECO–Germany). The Quantometer ARL 34000 uses an Ar spark source operated at atmospheric pressure. The steel sample is the target electrode and the counter electrode is a W rod (6 mm in diameter). The energy of the spark discharge heats the surface of the sample. The microsampling vaporization, atomization and excitation of the analytes follow this heating. An UV–VIS simultaneous spectrometer (spectral range 170–800 nm and focal length 1 m) equipped with photomultiplier tubes was used for the detection of the spectral radiation. More details about the spectral system are given in Table1.

Table 1.

Constructive characteristics of the spectral systems

Equipment	ARL 34000	LECO-GDS 1000
Spectral source	Argon spark discharge. The target electrode is the sample and the counter electrode is a W rod (6 mm diameter). Surface area exposed at vaporization: 60 mm^2	Argon glow discharge source with cathode plate and hollow–anode. Surface area of sputtering : 12 mm^2
Spectrometer	Simultaneous type, Paschen–Runge mount, concave grating 2160 grooves mm^{-1}, focal length 1 m, spectral range 170–800 nm, width entrace slit 20 μm, width exit slits 50 μm, exhausted, optical detection with photomultiplier tubes	Simultaneous type, Paschen–Runge mount, concave grating 2160 grooves mm^{-1}, spectral range 130–430 nm, focal length 1 m, width entrace slit 20 μm, width exit slits 50 μm, exhausted ($3 \cdot 10^{-2}$ hPa), optical detection with photomultiplier tubes

The simultaneous spectrometer LECO GDS–1000 uses a glow discharge source, which is a low pressure Ar plasma, obtained with two electrodes in contact with this plasma. The cathode is the sample mounted outside of the body of the source and it has a planar surface. The other electrode is a hollow- anode, which is the body of this source. The hollow – anode extends into the cathode dark space, defining the area of the sample, which is sputtered (about 12 mm^2). The key to success of the glow discharge is the easiness with which it creates the atomic cloud of the sample material directly from solid state. There is a region very close to the cathode (cathode dark space) where the Ar ions are accelerated towards the surface of the sample and sputtering the atoms of the sample. The atomic cloud spreads to the negative glow, where the atoms of the sample are excited by collisions with electrons or metastable Ar atoms. For the optical detection a simultaneous spectrometer, with a 130–430 nm spectral range was used. Details about the experimental setup are presented in Table1. The working conditions for spark source and GD source are presented in Table2.

Table 2.

Working conditions for spark and GD source

Source	Parameter							
	Sample	Pressure	Flow rate / l min^{-1}	Exhaust time / s	Preburning time / s	Integration time / s	Voltage / V	Sparking Frequency / s^{-1}
Spark	Compact polished piece	Argon	3	-	120	10	1000	25
GD	Compact polished piece	Argon vacuum 1.6 hPa	0.5	20	30	10	1000	-

Results and discussion

The calibration curves for C, P, S, Mn, Cr, Mo, Ni, Cu, V and Si were obtained using reference standard of low–alloyed steel samples. The correlation coefficients for these curves are in the range of 0.991–0.999, the lower values are in the case of P and S and the highest for C, Cr, Si, Ni and V.

The accuracy and precision of these techniques were verified using the degree of recovery (R) and relative standard deviation (RSD %) for ten concentrations in some reference standards of low–alloyed steel. The degree of recovery and RSD (5 successive measurements) for ICEM 102 reference standard are given in Table3.

Data from Table3 shows a similar accuracy for both techniques (degree of recovery is in the range 94–125 %), but the precision in the case of GDS 1000 is better than that for ARL 34000. The RSD values for GDS 1000 source are in the range 0.88–9.10 %, lower than those obtained with ARL 34000 (1.11–10.61 %). The higher stability of GDS 1000 source can be explained on the base of the sputtering phenomena, which is easier to control comparatively to thermic vaporization in the spark discharge. The mean results obtained by two methods were compared using the "t" test (Table3).

As shows the Table3, the calculated values of "t" ($t_{calculate}$) are lower than the critical value ($t_{95\ \%;\ \nu\ =\ 4}$ = 2.776) for all ten elements for both techniques, excepting Mn analyzed by GDS 1000 ($t_{calculate}$ = 4.44 > 2.776). These data demonstrate that there are no significantly differences between the results obtained by ARL 34000 and GDS 1000 with the reference standards of low–alloyed steel.

In order to compare the results obtained by ARL 34000 and GDS 1000 we resorted to the regression coefficient. The results are presented in Fig. 1.

Table 3.

The certificate contents, the found contents, grades of recovery and relative standard deviation for the metals concentration in ICEM 102 reference standard low–alloyed steel (5 successive measurements)

Metal	Certificated concentration / %	Founded concentration / %		Recovery / %		RSD / %		$t_{calculated}$	
		ARL	GDS	ARL	GDS	ARL	GDS	ARL	GDS
C	0.450	0.044±0.005	0.045± 0.004	98±1	99±1	1.11	0.88	0.89	0.45
P	0.033	0.035± 0.002	0.031± 0.002	106±6	94±6	6.10	6.10	0.45	0.45
S	0.038	0.040± 0.003	0.039± 0.002	105±8	103±5	7.89	5.26	0.29	0.22
Mn	1.050	1.176± 0.021	1.219± 0.015	112±2	116±2	2.00	1.42	2.25	4.44
Si	1.070	1.017± 0.060	1.050± 0050	95±6	98±5	5.61	4.67	0.39	0.18
Cr	0.140	0.150± 0.008	0.150±0.008	107±6	110±4	5.71	3.57	0.60	1.34
Mo	0.660	0.830± 0.070	0.805±0.070	125±11	122±9	10.61	9.10	1.09	1.08
Cu	0.230	0.240± 0.010	0.244±0.010	104±5	106±5	4.34	4.34	0.45	0.63
Ni	2.740	3.070± 0.120	2.918±0.110	112±5	106±4	4.38	4.01	1.23	0.72
V	0.300	0.308± 0.011	0.297±0.006	103±4	99±2	3.66	2.00	0.33	0.22

The equation of the regression line for ten points and an uncertainty quoted at 95 % probability is:

$$ARL\ 34000 = -\ 0.021 \pm 0.055 + (1.043 \pm 0.052)\ GDS\ 1000$$

The slope is not significantly different from unity nor is the intercept significantly from zero. The correlation coefficient is 0.999.

In Table4 the results obtained for steel samples with unknown metal concentrations are presented. The average results obtained by ARL 34000 and GDS 1000 were compared using the regression method. The equations of the linear regressions for seven steel samples are presented in Table5.

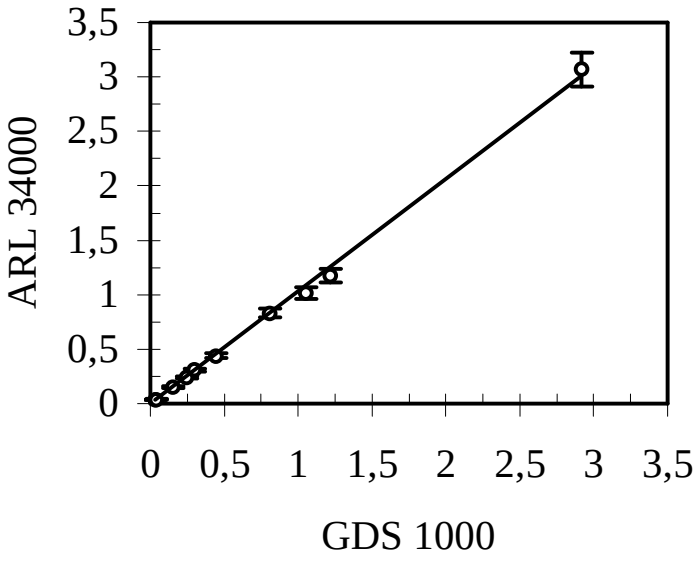

Fig.1. ICEM 102 reference standard low–alloyed steel plot (10 points) and 95 % probability, r = 0.999, m = 1.043±0.052, a = -0.021±0.055.

Table 4.

Analytical results obtained at analysis of the steel samples with ARL 34000 and GDS 1000 spectrometers (5 successive measurements)

Element & Method		Sample concentration / mean ± standard deviation						
		S1	S2	S3	S4	S5	S6	S7
C	ARL 34000	0.450± 0.004	0.200± 0.002	0.430± 0.002	0.340± 0.004	0.450± 0.003	0.160± 0.001	0.280± 0.004
	GDS 1000	0.447± 0.003	0.170± 0.001	0.409± 0.001	0.318± 0.003	0.443± 0.003	0.180± 0.001	0.274± 0.005
Mn	ARL 34000	0.740± 0.008	0.510± 0.002	0.850± 0.001	1.222± 0.003	0.650± 0.003	1.370± 0.008	1.280± 0.009
	GDS 1000	0.752± 0.009	0.541± 0.002	0.950± 0.001	1.287± 0.003	0.694± 0.002	1.481± 0.007	1.304± 0.007
Si	ARL 34000	0.267± 0.003	0.210± 0.003	0.332± 0.002	0.280± 0.003	0.230± 0.002	0.280± 0.003	0.350± 0.003
	GDS 1000	0.287± 0.002	0.219± 0.001	0.341± 0.001	0.289± 0.002	0.244± 0.001	0.305± 0.002	0.333± 0.001
S	ARL 34000	0.015± 0.002	0.027± 0.004	0.029± 0.002	0.022± 0.003	0.020± 0.002	0.020± 0.001	0.032± 0.002
	GDS 1000	0.016± 0.001	0.027± 0.003	0.023± 0.001	0.019± 0.003	0.017± 0.001	0.021± 0.001	0.024± 0.001
P	ARL 34000	0.020± 0.001	0.005± 0.001	0.020± 0.002	0.019± 0.004	0.018± 0.002	0.018± 0.002	0.030± 0.002
	GDS 1000	0.015± 0.001	0.008± 0.001	0.013± 0.001	0.014± 0.003	0.016± 0.001	0.016± 0.001	0.020± 0.001
Cr	ARL 34000	0.121± 0.002	0.110± 0.004	0.120± 0.002	0.170± 0.003	0.180± 0.002	0.195± 0.002	0.200± 0.003
	GDS 1000	0.116± 0.001	0.125± 0.003	0.140± 0.002	0.186± 0.002	0,221± 0.002	0.227± 0.001	0.210± 0.001
Ni	ARL 34000	0.014± 0.001	0.081± 0.006	0.051± 0.002	0.108± 0.003	0.120± 0.002	0.125± 0.002	0.078± 0.001
	GDS 1000	0.016± 0.001	0.072± 0.003	0.061± 0.002	0.089± 0.002	0.098± 0.001	0.101± 0.002	0.089± 0.001
Cu	ARL 34000	0.112± 0.002	0.170± 0.002	0.170± 0.001	0.200± 0.001	0.180± 0.001	0.160± 0.002	0.200± 0.002
	GDS 1000	0.117± 0.001	0.175± 0.003	0.159± 0.001	0.175± 0.001	0.197± 0.001	0.165± 0.001	0.189± 0.001
Mo	ARL 34000	0.025± 0.002	0.040± 0.003	0.030± 0.007	0.030± 0.003	0.040± 0.003	0.040± 0.004	0.040± 0.005
	GDS 1000	0.017± 0.001	0.029± 0.002	0.033± 0.006	0.036± 0.004	0.044± 0.002	0.034± 0.003	0.034± 0.003
V	ARL 34000	—	—	—	0.190± 0.002	—	—	0.150± 0.006
	GDS 1000	0.011± 0.001	0.013± 0.002	0.013± 0.003	0.197± 0.001	0.017± 0.001	0.013± 0.002	0.149± 0.005

In Table 4, the results obtained for steel samples with unknown metal concentrations are presented. The average results obtained by ARL 34000 and GDS 1000 were compared using the regression method. The equations of the linear regressions for seven steel samples are presented in Table5.

Table 5.

The regression equations ARL 34000 = $a \pm t \cdot s_a + (m \pm t \cdot s_m)$ GDS 1000 for seven steel samples (95 % probability)

Sample	Equation	Correlation coefficient	Number of points
S1	ARL = -0.015±0.055 + (1.003±0.038)GDS	0.992	9
S2	ARL = 0.008±0.055 + (0.938±0.110)GDS	0.996	9
S3	ARL = 0.011±0.038 + (0.927±0.093)GDS	0.997	9
S4	ARL = 0.011±0.023 + (0.965±0.051)GDS	0.999	10
S5	ARL = 0.003±0.031 + (0.945±0.110)GDS	0.996	9
S6	ARL = 0.004±0.017 + (0.989±0.038)GDS	0.996	9
S7	ARL = 0.007±0.013 + (0.987±0.031)GDS	0.999	10

a = intercept; s_a = standard deviation of intercept; m = slope;
s_m = standard deviation of slope

The data from Table5 show that the slope is not significantly different from unity nor is the intercept from zero. The correlation coefficients are in the range 0.996–0.999 for all seven steel samples. It has been concluded that the results obtained for steel samples by ARL 34000 (spark AES) show no bias against those obtained by GDS 1000 (GD–AES).

REFERENCES

1. J. Mika, T. Torok., *Analytical Emission Spectroscopy,* Akademiai Kiado, Budapest, 1973.
2. W. E. Pettit, G. Horlick, *Spectrochim. Acta, Part. B.,* **41B**, 699, (1986).
3. S. D. Anghel, T. Frentiu, A. M. Rusu, L. Bese, E. A. Cordos, *Fresenius j. Anal. Chem.,* **354**, 252, (1996).
4. H. Ali, K. C. Ng, J. D. Winefordner, *J. Anal. At. Spectrom.,* **6**, 211, (1991).
5. R. X. Liu, G. Horlick, *Spectrochim. Acta, Part. B,* **50B**, 537, (1995).
6. D. A. Rusak, R. L. Litteral, B. W. Smith, J. D. Winefordner, *Talanta,* **44**, 1987, (1997).
7. G. Coedo, M. T. Dorado, B. Fernandez, *J. Anal. At. Spectrom.,* **10**, 859, (1995).
8. E. A. Cordos, T. Frentiu, M. Ponta, A. M. Rusu, A. Fodor, *Analiza prin Spectrometria Atomica,* Institutul National de Optoelectronica, Bucuresti, 83–92, (1998).
9. E. R. Denoyer, K. J. Fredeen, J. W. Hager, *Anal. Chem.,* **63**, 445A, (1991).
10. S. S. Alimpiev, M. E. Belov, S. M. Nikiforov, *Anal. Chem.,* **65**, 3194, (1993).
11. E. F. Cromwell, P. Arrowsmith, *Anal. Chem.,* **67**, 131, (1995).
12. W. W. Harrison, C. M. Barshick, J. A. Klinger, P. H. Rattiff, Y. Mei, *Anal. Chem.,* **62**, 943A, (1990).
13. R. K. Markus, *J. Anal. At. Spectrom.,* **8**, 935, (1993).
14. C. R. Shick Jr, P. A. DePalma Jr, R. K. Markus, *Anal. Chem.,* **68**, 2113, (1996).
15. Y. Mei, W. W. Harrison, *Anal. Chem.,* **68**, 2135, (1996).
16. N. Winograd, *Anal. Chem.,* **65**, 622A, (1993).
17. C. Benninghoven, B. Hagenhoff, E. Niehuis, *Anal. Chem.,* **65**, 630A, (1993).
18. J. A. Gardella Jr, *Anal. Chem.,* **61**, 589A, (1989).
19. N. H. Turner, *Anal. Chem.,* **62**, 113R, (1990).
20. K. W. Nebesny, B. L. Maschhoff, N. R. Armstrong, *Anal. Chem*., **61**, 469A, (1989).

STUDIA UNIVERSITATIS BABEŞ-BOLYAI, PHYSICA, XLV, 2, 2000

VERY LOW POWER RADIOFREQUENCY CAPACITIVELY COUPLED PLASMA SUSTAINED IN AIR FOR LIQUID AND SOLID SAMPLE ANALYSIS BY ATOMIC EMISSION SPECTROSCOPY

S. D. ANGHEL[1], A. SIMON[1], T. FRENTIU[1], E. A. CORDOS[2]

***ABSTRACT*.** The very low power radiofrequency capacitively coupled plasma sustained in air at atmospheric pressure is described with the aim of using it as spectral source for atomic emission spectroscopy of pneumatically nebulised liquid samples and the direct analysis of non–conductive solid samples. The plasma was generated at a frequency of 13.56 MHz, absorbed RF powers of 20–70 W and air flow rates of lower than 1 l/min. The plasma is the intrinsic part of the resonant circuit of a free–running oscillator. The liquid samples were pneumatically nebulized using a Meinhard nebulizer and introduced into the plasma via a 4–roller peristaltic pump. The rotational temperature and the intensity ratio of ion to atom lines for Ca were determined experimentally. Detection limits were determined using the "3σ method" given by Boumans for 11 elements (Ag, Ca, Cr, Cu, Mg, Mn, Na, Li, Ba, Pb, Sr) at an RF power of 50 W and air flow–rate of 0.7 l/min. The same plasma was used for the direct analysis of non–conductive solid samples. All measurements have been carried out on cylindrical sample pellets of chalk (pressed in a steel press at a pressure of $87 \cdot 10^5$ Pa), at an RF power of 40 W and air flow–rate of 0.5 l/min.

Introduction

Over the last few decades, plasma excitation sources at atmospheric pressure for analytical atomic emission spectrometry (AES) have been well characterised as sensitive spectral sources. Most of these sources are inductively coupled plasmas (ICPs). Historically, the radiofrequency (RF) capacitively coupled plasma (CCP) as physical phenomenon, was studied before ICPs. The principle of capacitive coupling to generate a plasma has been known since late 1920s. In 1941, Cristescu and Grigorovici [1] reported that an RF CCP could be obtained at

[1] Faculty of Physics, Babes–Bolyai University, M. Kogalniceanu 1, 3400 Cluj, ROMANIA
[2] Faculty of Chemistry, Babes–Bolyai University, Arany J. 11, 3400 Cluj, ROMANIA

atmospheric pressure between two electrodes, one of them being a platinum tip. Between 1949 and 1961 they made the first steps in consecrating the CCP sustained at atmospheric pressure as excitation source for spectral analysis [2, 3].

The interest on plasma spectral sources was shifted to the ICPs in the early 1960s, when Greenfield and al. [4] reported almost simultaneously with Wendt and Fassel [5] the successful application of an argon ICP in spectrochemical analysis. Since then, until the mid 80's the world of spectrochemical analysis was dominated by the ICPs. After 1988, Blades et al. [6–10] "rediscovered" the RF CCP in different electrode geometries for spectrochemical analysis. Probably they were attracted by both low RF power and argon consumption compared to the ICPs.

Independently from the electrode geometry, from a spectroscopic point of view, the CCP is a fairly good spectral source: it could be maintained in various noble gas atmospheres (usually Ar or He) or their mixture with Air (usually Ar and Air in various proportions); the spectral gas consumption is low (less than 1 l/min); it could be maintained at various industrial RF frequencies (generally at 13.56 or 27.12 MHz) at very low (less than 100 W) or low and medium (between 100–500 W) RF power levels. From practical point of views, the advantages of this kind of plasma are mainly economical: low operating costs versus fairly good detection limits.

Thus, in the last decade, our attention was directed to the construction of RF generators able to generate CCPs at low and very low absorbed RF powers. Firstly, we have built [11] an RF generator for maintaining an argon CCP at atmospheric pressure. The working frequency was 27.12 MHz and the RF powers were in the range of 100–300 W. Two electrodes configurations have been used to maintain the plasma: tip–ring and tube–ring electrode geometries. This generator was coupled with a sequential monochromator, resulting an atomic emission spectrometer. It has been used for analysis of liquid samples introduced into the plasma by pneumatic nebulization and of conductive solid samples. The obtained results were promising [12–18]. Secondly, the RF generator built with the aim of studying the CCP in argon and air at atmospheric pressure at very low RF powers (20–70 W and 13.56 MHz) [19] was used to generate an argon plasma as spectral source for direct analysis of non–conductive samples [20].

In the present work, the second RF generator is used to maintain an air CCP at atmospheric pressure. This plasma is studied as atomisation and excitation source for liquid samples introduced into the plasma by pneumatic nebulization and as possible sampling and excitation source for non–conductive solid samples. Two kind of plasma devices are presented. A torch with two electrodes (the sustaining tip of the plasma and a tip like

grounded counterelectrode) for analysis of liquid samples and a device for direct analysis of non–conductive samples. The second device, a sputtering chamber, was built by modifying the previous torch to provide the in–situ sampling and the excitation conditions for the non–conductive solid samples.

Instrumentation

Experimental setup

The construction of the RF generator used for sustaining the very low power capacitively coupled plasmas at atmospheric pressure, is described elsewhere [19]. The plasma was generated at a frequency of 13.56 MHz, at various absorbed RF power levels (20–70 W). The main characteristic of our capacitively coupled plasma is that it is an intrinsic part of the tuned circuit of the radiofrequency generator. The oscillator is one of the inductive reaction type having the tuned circuit placed in the control grid network of the active element (pentode tube). The presence of the adjustable inductive coupling in the reaction circuit offers the possibility of the maximisation of the RF power transferred to the plasma. It was experimentally proved that this plasma could be successfully used for the analysis of liquid samples [15, 17] by atomic emission spectroscopy technique and for the direct analysis of both conductive [14] and non–conductive solid samples [20].

The experimental setup, for both techniques, is schematically outlined in Fig.1. and Fig.2. Details of the equipment used and the operating conditions are provided in Table1.

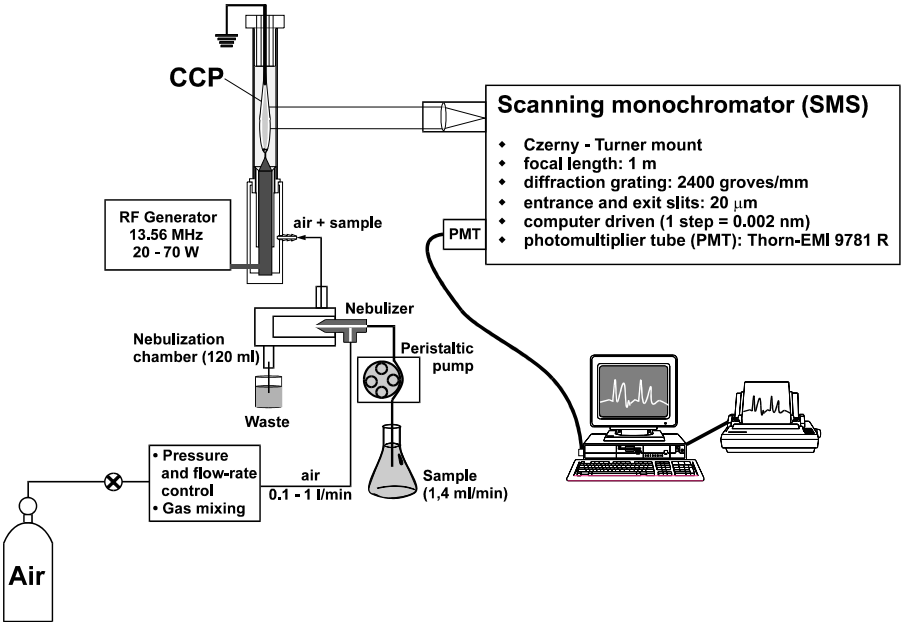

Fig. 1. The experimental set–up for liquid sample analysis by atomic emission spectroscopy

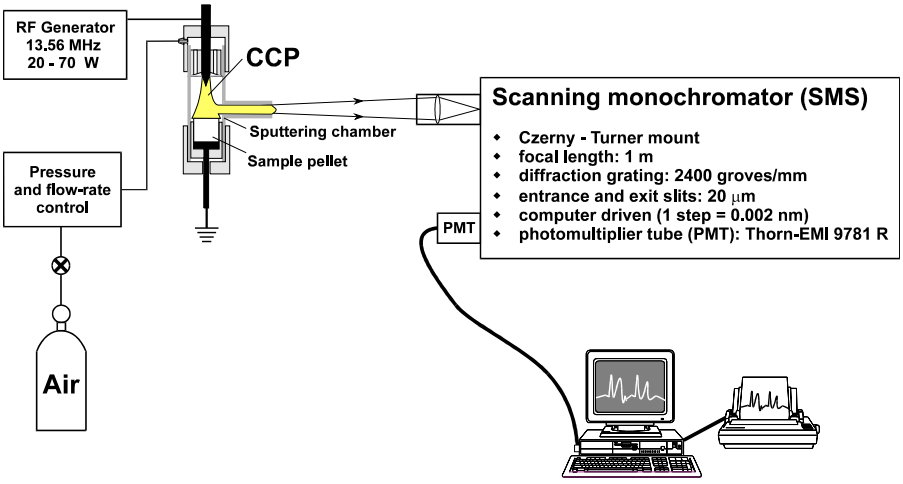

Fig. 2. The experimental set–up for the direct analysis of non–conductive solid sample by atomic emission spectroscopy

Internal calibrations were performed with an Al hollow cathode lamp and the corrections for the spectral response of the spectrometric system (optics and photomultiplier) were made with an EPI 1604 type spectral irradiance standard lamp.

The CCP torch. Liquid sample preparation

The low power CCP for liquid sample analysis is sustained on a kanthalum tip (composition: 20–24 % Cr, 5–6 % Al, 2 % Co, 68–73 % Fe). For a greater stability of the plasma the presence of the second (counter)electrode is required. The tip is part of the CCP torch presented in Fig.3.

The main parts of the CCP torch are: a quartz tube ① (14 mm i.d., 16 mm o.d., 150 mm length); a brass electrode ⑤ as support of a kanthalum tip ② (0.8 mm in diameter and 4 mm in length); an electrode holder made out of PTFE ③ (with 12 concentric holes of 1 mm in diameter, providing the sample entrance to the plasma) and a PTFE chamber ④ (volume = 10 ml); RF coupling ⑦ and the air and sample introduction inlet ⑥. The counter electrode is grounded and made out of copper ⑨ (2 mm thickness and 100 mm length). A PTFE electrode holder ⑧ (with 6 concentric holes of 2.5 mm in diameter for gas outlet) is providing the joining with the remain of the torch. The plasma gas is air, and flows in a laminar motion through the quartz tube with a flow–rate of 0.1–1 l/min. At these flow–rates the plasma has a candle flame–like with an orange like colour.

Stock solutions (1000 μg/ml element) were prepared by dissolution of the high–purity metals or their salts in HNO_3 (1+1) or in HCl (1+1) (FLUKA). Single element working standard of 50 μg/ml were obtained by diluting the stock solutions with high purity 2 % v/v HNO_3. These solutions were used for the analysis of liquid samples by atomic emission spectroscopy technique. A blank solution of 2 % (v/v) HNO_3 was used.

Table 1.

Equipment and operating conditions

Plasma generation	RF oscillator (13.56 MHz; 20–60 W). Laboratory constructed. *Babes–Bolyai University, Faculty of Physics, Cluj, Romania* Stabilised Power Supply BS 452 E type (2 × 500 V; max. 400 mA). *TESLA, Czech Republic* Stabilised Power Supply I 4104 type (40 V; 5 A). *IEMI, Bucharest, Romania*
Plasma torch	Laboratory constructed (Fig.3.)
Sputtering chamber	Laboratory constructed (Fig.4.)
Plasma support gas	High purity, compressed air (0.1–1 l/min)

Optics	110 mm focal length, 30 mm diameter fused silica lens
Monochromator	Computer driven scanning type (1 step = 0.002 nm), 1 m focal length, Czerny–Turner mount, with 2400 groves·mm^{-1} diffraction grating and 20 μm slits (internal wavelength calibration with an Al hollow cathode lamp). *ICIA, Cluj, Romania*
Detector	9781 R photomultiplier tube operated at 700 V. *Thorn EMI Ltd.*, *England*
Data acquisition and processing	Digital data acquisition and monochromator driving carried out by an IBM–PC equipped with a laboratory constructed interface (64 μs data acquisition time); data processing with an appropriate in–house software. *ICIC, Cluj, Romania*

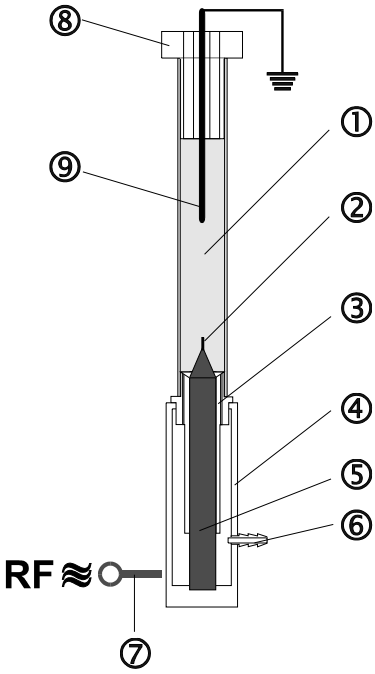

Fig. 3. The CCP torch

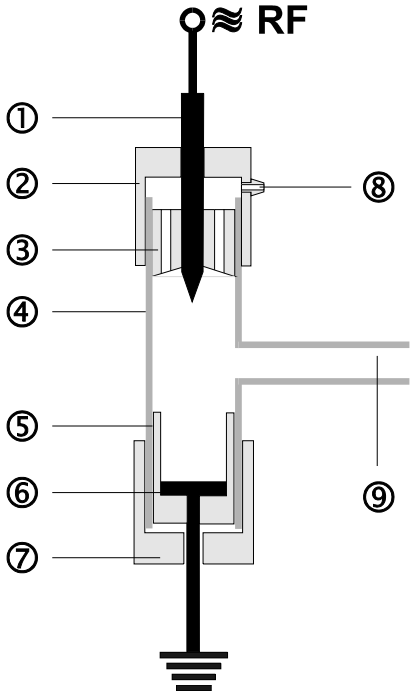

Fig. 4. The sputtering chamber

The sputtering chamber . Sample pellet preparation

The capacitively coupled plasma used for RF sputtering of non–conductive solid samples was obtained inside of a tubular quartz chamber ④ (14 mm i.d., 100 mm length, with a lateral port, 5 mm i.d., 50 mm length) on a tungsten electrode ① (4 mm in diameter, with the tip sharpened at 45^{o})

(see Fig.4.). The plasma gas was introduced inside the chamber via a gas inlet ⑧ and a PTFE electrode holder ③ (12 concentric, 1 mm i.d. holes). The sample pellet was placed inside of a PTFE sample holder cup ⑤ on plate brass counter electrode ⑥. The RF electrode and the sample holder were placed at the opposite sides of the quartz tube and fixed with two PTFE lids ② and ⑦. The plasma viewing is insured by the lateral port ⑨.

The experimental measurements were carried out on cylindrical sample pellets of chalk ($CaCO_3$). The raw materials necessary for pellet preparation were mixed with 30 ml ethyl alcohol in a mortar and stirred until homogeneity. This procedure was done until the whole quantity of the added alcohol was evaporated and this procedure was repeated twice. Drying at 105 ^oC was followed by 7 h of sintering in furnace at 1000–1100 ^oC. After a new set of grinding and sifting, the sample was homogenised again. A quantity from the powders obtained this way was pressed in a steel press at a pressure of $87 \cdot 10^5$ Pa for 10 minutes. The resulting analytical sample pellets had cylindrical shape, with a 11 mm diameter and were used for the direct analysis of non–conductive solid samples.

Results and Discussion

The study of physical and analytical properties (temperatures, line intensity ratios, signal to background ratios, dynamic range, detection limits) of a plasma discharge represents a very important preliminary step toward understanding the mechanisms and processes that occur within the plasma used as spectral source and provides for the possible users an indication as to whether samples at low levels can be analysed with some desired level of precision.

Physical properties

As far as the plasma support gas was air, the rotational temperature (T_{rot}) seems to be the most important physical property of this type of plasmas. It was calculated via the Boltzmann plot method, from the slope of a regression line fitted to the appropriate data according to Eqn.1, using six lines from the R2 branch of the (0,0) transition of the OH radical (307.1; 307.3; 307.4; 307.7; 308.4 and 308.9 nm).

$$\log\left(\frac{I}{g \cdot A \cdot 2 \cdot (J+1)}\right) \sim \frac{E_{rot}}{k_B \cdot T_{rot}} \qquad (1)$$

where: I = relative intensity of the OH line; g = statistical weight; A = transition probability; k_B = Boltzmann constant, E_{rot} = excitation energy of a rotational level. The spectroscopic data were taken from the paper of Kornblum and De Galan [21].

The temperature measurements were performed at an RF power of 50 W and air flow–rate of 0.7 l/min, in two situations: for pure but not dried air plasma without distilled water, and for an air plasma with pneumatically nebulised distilled water, introduced via devices described in Fig.1. and Table 1., respectively. Thus, temperatures of 2240 K and 2210 K were obtained, respectively. This results and the plasma spectra in those two situations, presented in Fig.5a. and Fig.5b., demonstrate that the water provides extra OH radicals, meaning higher relative intensities in the band and has a coolant action , lowering the rotational temperature.

The intensity ratio of ion to atom lines for a certain element (Ca in our case) is an indicator of the existing species (ions, atoms or both) within a plasma discharge. This intensity ratio depends on the electron number density, ionization temperature and ionization potential of the elements in question. For our spectral source, the ratio was determined experimentally using the 393.367 nm ionic and the 422.673 atomic lines of Ca and was found to be 1 : 13. Thus, our plasma contains more atomic species than ions.

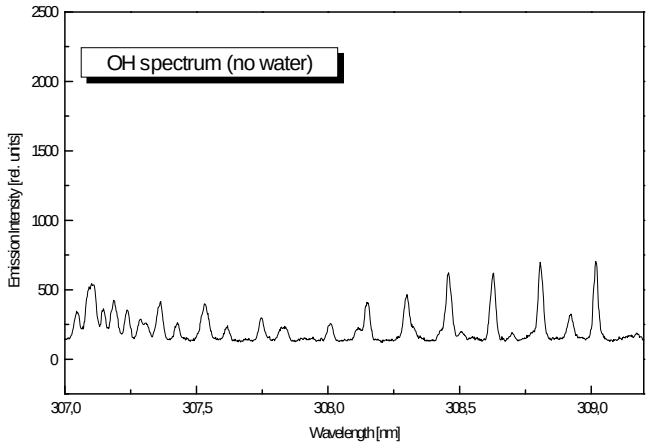

(a)

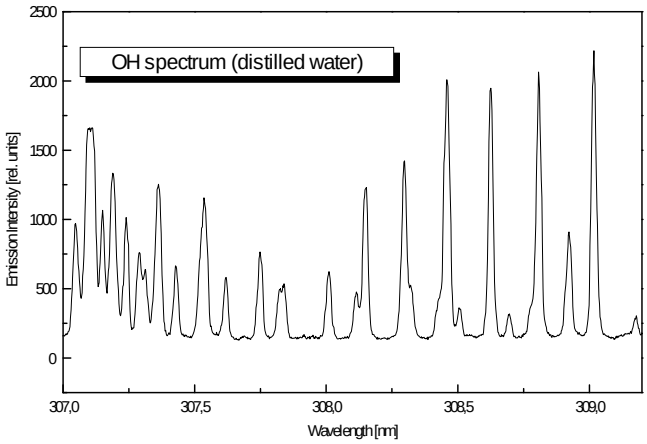

(b)

Fig. 5. The R2 branch of the (0,0) transition of the OH radical

Analytical properties

Without any doubt, the most important analytical characteristic of a spectral source is the detection limit. The detection limit of the concentration (LOD or c_L) according to Boumans [22] is:

$$c_L = k \cdot \frac{\sigma_B}{x_B} \cdot \frac{c_o}{x_A / x_B} = k \cdot 0.01 \cdot RSDB \cdot \frac{c_o}{SBR} \qquad (2)$$

where: x_A= net analyte signal; x_B = net analyte signal; SBR = x_A / x_B = signal–to–background ratio (SBR); σ_A = standard deviation of the background signal; RSDB = relative standard deviation of the background signal and k = const.

If $k = 2\sqrt{2}$ (≈ 3) the formalism presented above is called "3σ method" and it is the most commonly used technique of detection limit determination. By using this method the SBR and LOD for a number of 11 elements (Ag, Ba, Ca, Cr, Cu, Li, Mg, Mn, Na, Pb and Sr) were determined at an observation height of 10mm above the tip by introducing 50 μg/ml aqueous working standard solutions of each element. These result are presented in Table 2., in comparison with the results for the same elements, obtained with an Ar plasma, operated at the same RF power and gas flow–rate parameters [23].

The detection limits listed in Table 2. for the air CCP at 40 W were found to be in the range of 0.014–66 μg/ml. These results are comparable of those of the low power Ar CCP. For alkali metals (Na and Li) the

detection limits are better in the air plasma. The results from Table 2. are in a good agreement with the theory according to what a molecular plasma, the low power air CCP in our case, is better for the analysis of a refractory element (e.g., Ba) than an Ar plasma.

Table 2.

Detection limits for the low power air CCP

Element	Analytical wavelength [nm]	LOD [µg/ml]	
		air CCP 40 W	argon CCP 40 W
Na	588.90	0.014	0.107
Ca	422.67	0.650	0.170
Pb	405.78	28.920	1.400
Ag	328.07	1.670	0.114
Cu	324.75	24.100	0.166
Mg	285.21	5.850	0.100
Cr	425.43	42.400	4.200
Mn	403.08	1.310	0.520
Ba	493.41	66.100	142.000
Sr	460.70	1.310	0.078
Li	670.79	0.063	0.130

The dynamic range of the plasma source was determined by plotting a calibration curve for Ag. It is about 3 orders of magnitudes. The correlation coefficient for the calibration curve is about 0.999 for this dynamic range and the standard deviation of its slope is 2.8 % (Fig.6.)

The influence of RF power on the background and on the emission intensity was studied for Na doublet (588.995 nm/589.59 nm) and the dependencies are presented in Fig.7. A linear increase of the emission intensities and a constant background could be concluded.

The behaviour of Na atoms in a plasma spectral source could provide some other important information about that source. The self–absorption is a phenomenon which occurs when on its path through the plasma the emitted radiation is absorbed by the atoms in ground state. It is estimated as the ratio of the two emission intensities of the Na doublet, DI/DII. In the absence of this phenomenon this ratio has to be 2, and below 2 when the self–absorption is present. For our plasma source the ratio was found to be between 1.9 and 2.0. These results shows that the self–absorpiton is lower compared to the reference value of 1.8, the self–absorbtion constant in an arc source [24].

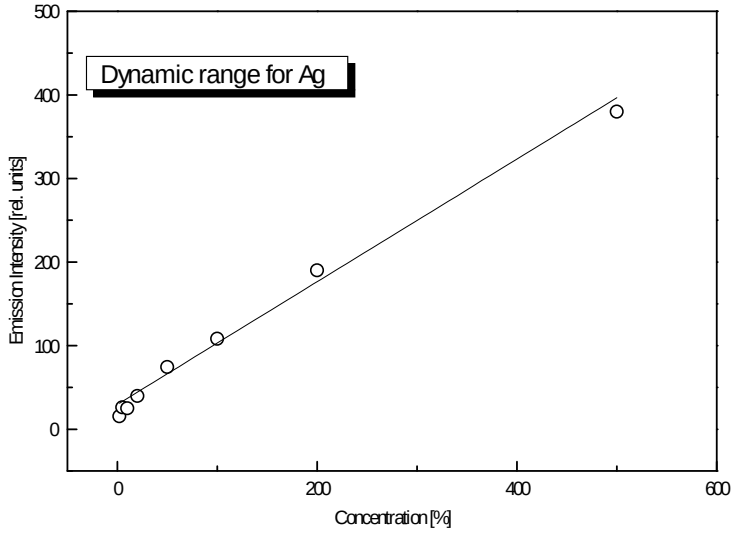

Fig. 6. Dynamic range for Ag

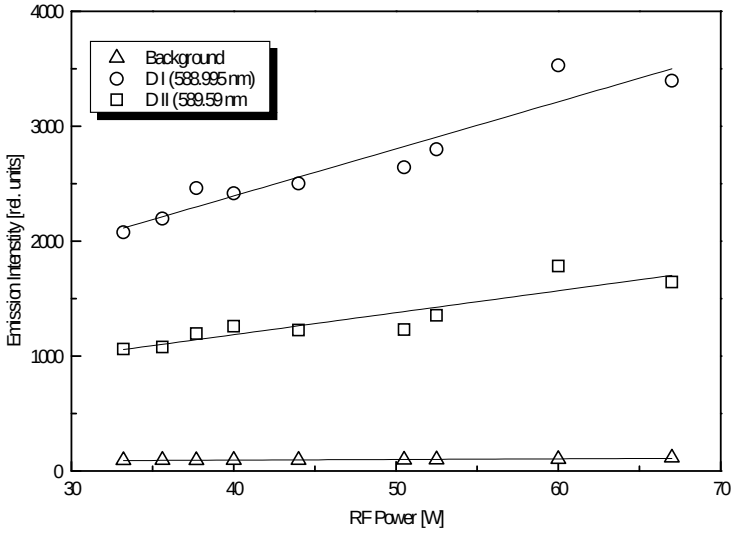

Fig. 7. Effect of RF power on background and signal

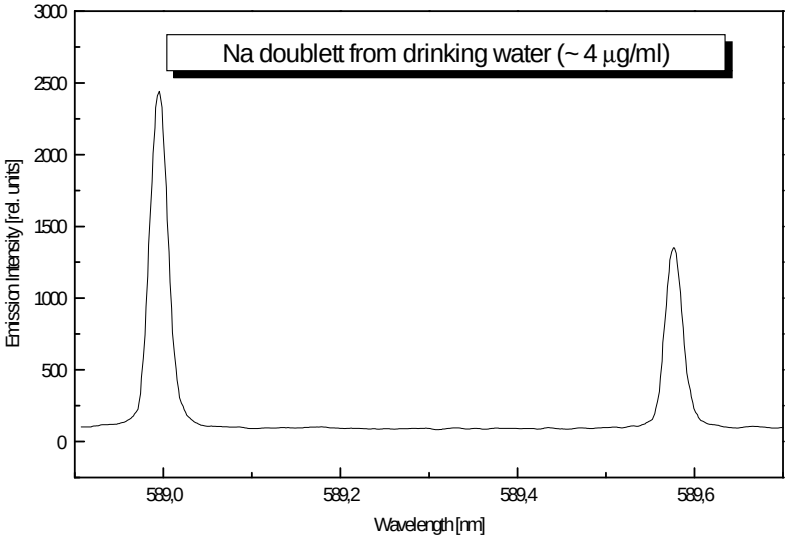

Fig. 8. Na doublet in drinking water

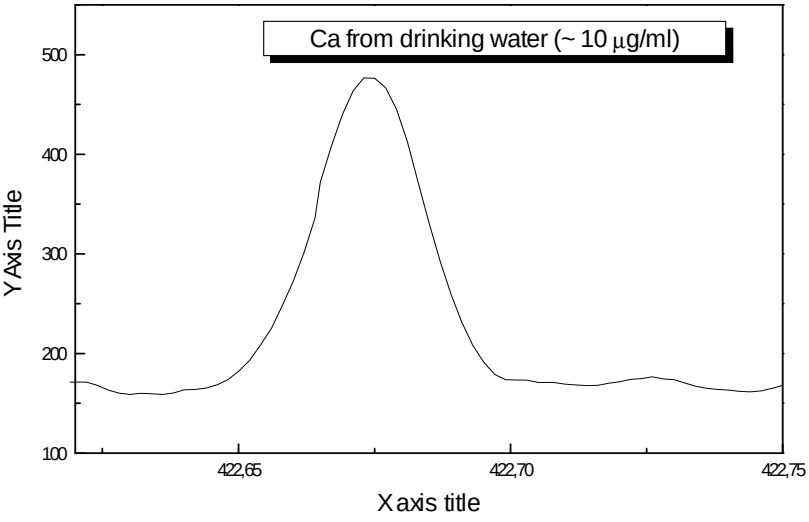

Fig. 9. Ca atomic line in drinking water

The low power air CCP is a versatile tool for real liquid sample analysis. The emission lines for Na and Ca from drinking water are presented in Fig.8. and Fig.9.

The possibility of using a capacitively coupled plasma for RF sputtering of non–conductive solid samples was one of the purposes of our research work and the preliminary results are presented in this paragraph. The main characteristic of our low power capacitively coupled plasma is that it is an intrinsic part of the tuned circuit of the radiofrequency generator (Fig.10.).

The automatic grid bias network (R_gC_g) develop a negative voltage on the grid in the range of 150–200V. Its value is function of the anode positive bias. Over this negative dc component, the RF component is superimposed, the amplitude of oscillation being 15–20% greater than the dc potential of the control grid. Because the oscillator works under resonant conditions, the amplitude of the RF oscillations on the sustaining electrode of the plasma is in the range of 2000–3000V. Due to the DC component the RF wave is translated toward negative values, its form being asymmetric with respect to ground. During a full cycle of the RF wave, the plasma sustaining electrode has a negative potential a time interval longer than a half–cycle. This fact, combined with the lower mobility of the positive ions relative to the electrons, cause an accumulation of positive charge greater than the negative charge close to the sustaining plasma electrode. This accumulation of positive charge has two consequences: (a) – an excess of negative charge that appears toward the free end of the plasma where the sample is placed, and (b) – the electrostatic shielding of the sustaining electrode of the plasma. Consequently, an internal DC electric field appears in the plasma.

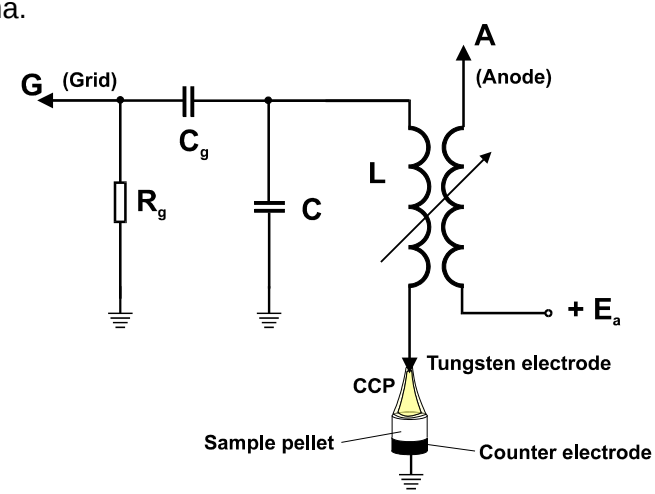

Fig. 10. The CCP intrinsic part of the RF oscillator's tuned circuit

At a critical distance between the plasma electrode and the sample (about 2–4 mm) the electrical field is sufficiently intense to accelerate the positive ions towards the sample and to induce sputtering of the sample, causing sample atomisation. Sputtered atoms are then available to enter the plasma for subsequent excitation and ionisation. At sufficiently high RF powers (above 50 W in the case of an air plasma), the heating of the sample is so high that it is tending to incandescence. We suppose that the increase of the sample temperature causes the thermal evaporation on its surface. This can be a supplementary atomisation mechanism which will cause an increase in the number of the sample atoms in the plasma. These affirmations are supported by the plots from Fig.11., Fig.12. and Fig.13.

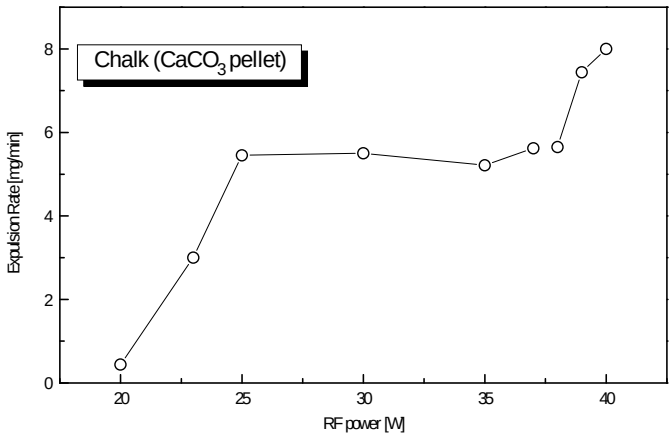

Fig. 11. Expulsion rate as function of RF power

Fig.11. presents the dependence of the expulsion rate on the RF power absorbed by the plasma. The expulsion rate was calculated as being the difference between the chalk sample weight before and after exposure to collisions with ions. Nine replicate sample pellets were used. At powers lower than 20 W, the sputtering rate is low since the intensity of the dc internal field is low. In the range of 20–40 W, the sputtering rate is nearly constant which means the intensity of the accelerating field remains nearly constant. An explanation of this phenomenon could be the complementary effects of the increase of the RF voltage amplitude and of the electrostatic shielding, respectively. In this power range the sample atomisation is produced only by the sputtering process. At powers higher than 50 W, the

thermal evaporation will be present because of heating of the sample by energised ions. Such, an increase of the atomisation rate appears.

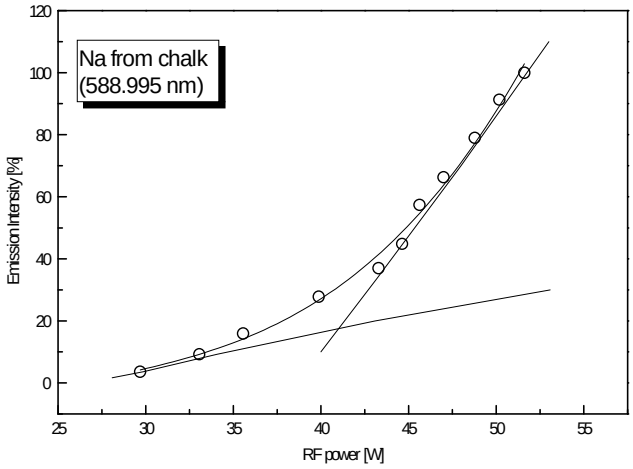

Fig. 12. Effect of RF power on the Na emission intensity

In Fig.12. the effect of RF power on the emission intensities of Na (588.99 nm) from the $CaCO_3$ matrix is presented. As one can notice, each plot is composed of two straight lines with different slopes. The first line corresponds to the sputtering mechanism and the second to the combination of sputtering and thermal evaporation. Observing that the increase of the slope takes place an the RF power of 42–45 W which is the same as when the atomisation rate begins to increase, the thermal evaporation assumptions seem to be plausible.

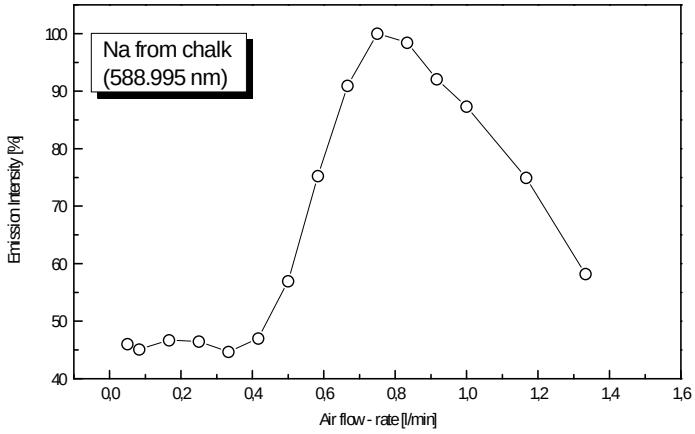

Fig. 13. Effect of air flow–rate on the Na emission intensity at an RF power of 40 W

In Fig.13., the effect of the gas flow rate on the Na (588.99 nm) emission line from the $CaCO_3$ matrix is presented, at an RF power of 40 W is shown. The plot has a maximum at a gas flow rate that can be considered optimum (0.5 l/min). At this gas flow rate, the number of sputtered atoms entering the plasma, where the excitation and atomisation processes take place, are maximal. At gas flow rates greater than the optimum, the residence time of atoms in the plasma decreases, and as a result, the net intensities of the emission line decrease too. Mg impurities were found in the chalk. The Mg emission line (285.21 nm) is presented in Fig.14.

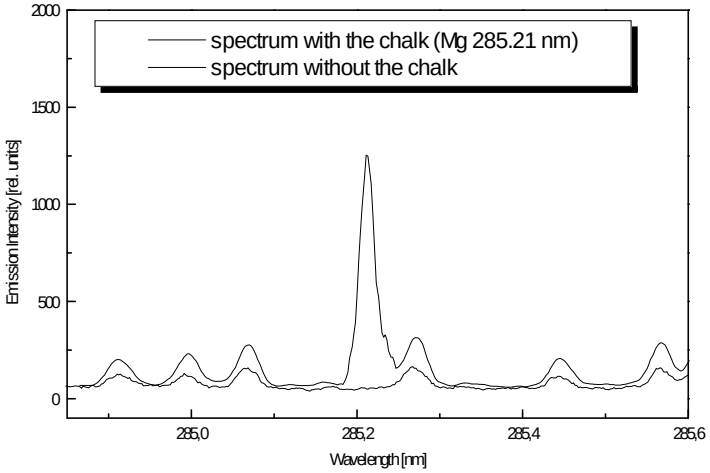

Fig. 14. Emission line of Mg from chalk

Conclusions

It has been shown that an air RF CCP operated at atmospheric pressure and very low power could be a valuable spectral source for atomisation and excitation of liquid samples and for sampling and excitation of non–conductive solid samples. A very stable air plasma could be maintained at a power of 50 W and a gas flow–rate of 0.7 l/min. The LODs for liquid samples were in the 0.014 ppm to 66 ppm range. Fore some elements they are comparable or better than the LODs obtained in the Ar RF CCP at the same power. If some constructional and functional optimisation will be make, the air RF CCP obtained with the described sputtering chamber could be successfully used as spectral source for trace element determination in chemical reagents and geological samples. The main advantage of this spectral source is the very low price of the plasma gas.

Acknowledgements

The authors wish to thank to Dr. A. Popescu and C. Dem for their valuable help in the experimental work. They are also indebted to H. Mioscu and I. Marginean for the interface and the in–house software. This research was supported by Research Grant no. 32575/1999, CNCSIS 117.

REFERENCES

1. G. D. Cristescu and R. Grigorovici, Bull. Soc. Roum. Phys. 42, 37–51 (1941).
2. G. D. Cristescu and R. Grigorovici, R. Rev. Phys. 1, 103–126 (1956).
3. G. D. Cristescu and R. Grigorovici, Com. Acad. RPR 5, 515–520 (1955).
4. R. H. Wendt and V. A. Fassel, Anal.Chem. 37, 920–922 (1965).
5. S. Greenfield, I. L. Jones and C. T. Berry, Analyst 89, 713–720 (1964).
6. D. C. Liang and M. W. Blades, Anal. Chem. 60, 27–31 (1988).
7. D. C. Liang, D. Huang, and M. W. Blades, J. Anal. At. Spectrosc. 4, 789 (1991).
8. D. Huang and M. W. Blades, J. Anal. At. Spectrosc. 6, 215–219 (1991).
9. D. C. Liang and M. W. Blades, Spectrochim. Acta. 44B, 1059–1063 (1989).
10. B. M. Patel, J. P. Deavor and J. D. Winefordner, Talanta 35, 641–645 (1988).
11. S. D. Anghel, Studia Univ."Babes–Bolyai" Cluj, Physica, XXXVIII, nr.1, pp. 39–51 (1993).
12. E. A. Cordos, S. D. Anghel, T. Frentiu, and A. Popescu, J. Anal. At. Spectrom 9, pp. 635–641 (1994).
13. S. D. Anghel, E. Darvasi, T. Frentiu, A. M. Rusu A. Simon, and E. A. Cordos, Fresenius Journ. Anal. Chem. 355, pp. 250–251 (1996).
14. S. D. Anghel, T. Frentiu, A. M. Rusu, L. Bese, and E. A. Cordos, Fresenius Journ. Anal. Chem. 355, pp. 252–253 (1996).
15. T. Frentiu, A. M. Rusu, M. Ponta, S. D. Anghel, and E. A. Cordos, Fresenius Journ. Anal. Chem. 355, pp. 254–255 (1996).
16. E. A. Cordos, T. Frentiu, A. M. Rusu, S. D. Anghel, A. Fodor, and M. Ponta, Talanta 48, pp. 827–837 (1999).
17. S. D.Anghel, T. Frentiu, A. M. Rusu, A. Popescu, A. Simon, and E. A. Cordos, Acta Chimica Hungarica–ACH Models in Chemistry 136, pp. 131–148 (1999).
18. T. Frentiu, A. M. Rusu, S. D. Anghel, A. Popescu, S. Negoescu, A. Simon, and E. A. Cordos, Acta Chimica Hungarica–ACH Models in Chemistry 136, pp. 119–129 (1999).
19. E. Tataru, S. D.Anghel, and I. I. Popescu, Rev. Roum. Phys. 39, pp.29–44, 1991.
20. S. D. Anghel, E. A. Cordos, T. Frentiu, A. Popescu, and A. Simon, J. Anal. At. Spectrom 14, pp. 541–545 (1999).
21. G. R. Kornblum and L. de Galan, Spectrochim. Acta. 29B, 249–261 (1974).
22. P. W. J. M. Boumans, Spectrochim. Acta. 46B, 431–445 (1991).
23. S. D. Anghel, A. Simon, T. Frentiu and E. A. Cordos, to be published.
24. Tablitsi Spektralnikh Linii, Izdatelstva Nauka, Moskow (1977).

STUDIA UNIVERSITATIS BABEŞ-BOLYAI, PHYSICA, XLV, 2, 2000

MAGNETIC SUSCEPTIBILITY INVESTIGATION OF V_2O_5-B_2O_3-PbO GLASSES

I. ARDELEAN[1], GH. ILONCA[1], V. SIMON[1], S. FILIP[2], C. CEFAN[2] AND S. SIMON[1]

ABSTRACT. The temperature dependence of the magnetic susceptibility of $xB_2O_3 \cdot (1-x)[V_2O_5 \cdot PbO]$ glasses with $0.05 \leq x \leq 0.8$ has been investigated. This dependence denotes a Curie-type behaviour in the entire composition range and indicates that the V^{4+} ions do not participate to the superexchange interactions. From these data and considering that only V^{4+} and V^{5+} ions occur in the studied glasses we have estimated the V^{4+} ions content as well as the $N_{V^{4+}}/N_{V_{total}}$ ratio. The fraction of the V^{4+} ions which are favored to exist in these glasses increases with the V_2O_5 content.

Introduction

The V^{4+} ions incorporated in oxide glasses as spectroscopic probes have been studied by several researchers [1-6]. Because of their semiconducting behaviour, the electrical properties of these glasses were also investigated [6-8]. All these studies evidenced for oxide glasses containing V_2O_5 the presence both of V^{4+} and V^{5+} ions [7-10].

The magnetic properties of oxide glasses with V^{4+} ions were less studied. In earlier works we reported the magnetic properties of $xV_2O_5 \cdot (1-x)[2B_2O_3 \cdot PbO]$ [5], $xV_2O_5 \cdot (1-x)[2B_2O_3 \cdot Li_2O]$ [11] and $xV_2O_5 \cdot (1-x)[2P_2O_5 \cdot PbO]$ [12] glasses with $x \leq 0.55$, $x \leq 0.5$ and ≤ 0.5, respectively.

In the present work is investigated the magnetic behaviour of $xB_2O_3 \cdot (1-x)[V_2O_5 \cdot PbO]$ glasses with $0.05 \leq x \leq 0.8$ and the distribution of the vanadium ions in the V^{4+} and V^{5+} valence states.

Experimental

Glasses of the system $xB_2O_5 \cdot (1-x)[V_2O_3 \cdot PbO]$ have been prepared by using reagent grade purity V_2O_5, PbO and H_3BO_3. The mixtures, in suitable proportions corresponding to the designed concentration of x, were

[1] Faculty of Physics, Babes-Bolyai University, 3400 Cluj-Napoca, Romania
[2] Faculty of Science, Physics Department, University of Oradea, Romania

mechanically homogenized and melted in sintered corundum crucibles at 1250°C. The molten materials was kept at this temperature for 10 minutes, then quenched at room temperature by pouring onto a stainless steel plate. The samples were analyzed by means of X-ray diffraction and did not show an crystalline phase.

The magnetic data were obtained using a Faraday type balance in the temperature range 80-300 K.

Results and discussion

The temperature dependences of the reciprocal magnetic susceptibility of some glasses from the investigated glass system are presented in Fig. 1. These dependences show a Curie-type behaviour in the entire composition range. The results suggest that the vanadium ions are isolated but they may be involved in dipole-dipole type interactions according to the EPR data [13]. Therefore, in these glasses the vanadium ions behave magnetically similar to lead [5] and lithium [11] borate oxide glasses. In the case of V_2O_5-P_2O_5-PbO glasses [12] the V^{4+} ions participate to the negative superexchange interactions for x > 0.03.

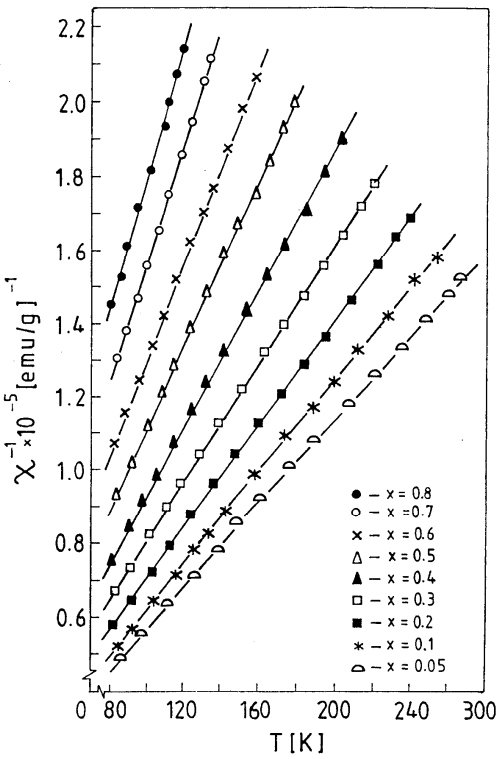

Fig. 1. The temperature dependence of the reciprocal magnetic susceptibility

The composition dependence of the experimental molar Curie constant is given in Table 1. The experimental C_M values are lower than the expected ones, assuming that all vanadium ions are in V^{4+} valence state. Therefore, we suppose both V^{4+} and V^{5+} ions to be present. The occurrence of the V^{4+} ions was evidenced in all investigated samples by EPR studies [13], which indicate that the V^{4+} ions content increases with V_2O_5 concentration. In this case, considering that the V^{5+} ions are diamagnetic and having in view that the atomic magnetic moment of V^{4+} ions is $\mu_{V^{4+}} = 1.73\,\mu_B$, which was generally reported for paramagnetic salts [14], we can estimate in a first approximation [5] the molar fraction of V^{4+} ions, y, using the relation

$$y = \frac{\mu_{\exp}^2}{\mu_{V^{4+}}^2}(1-x),$$

where $\mu_{\exp}$ is the atomic magnetic moment estimated from molar Curie constant values. The obtained results are presented in Table 1. One can observe from these data that in the investigated glass system the molar fraction of V^{4+} ions ($V_2^{4+}O_5$) increases with V_2O_5 content (Fig. 2).

Table 1.

The molar Curie constant, molar fraction of V4+ ions and y/(1-x) ratio

x	C_M [uem/mol]	y	y/(1-x)
0.8	0.07637	0.10	0.5
0.7	0.1083	0.15	0.5
0.6	0.15649	0.21	0.53
0.5	0.2116	0.28	0.56
0.4	0.2888	0.39	0.65
0.3	0.3753	0.51	0.73
0.2	0.4780	0.64	0.80
0.1	0.5936	0.80	0.89
0.05	0.6807	0.91	0.96

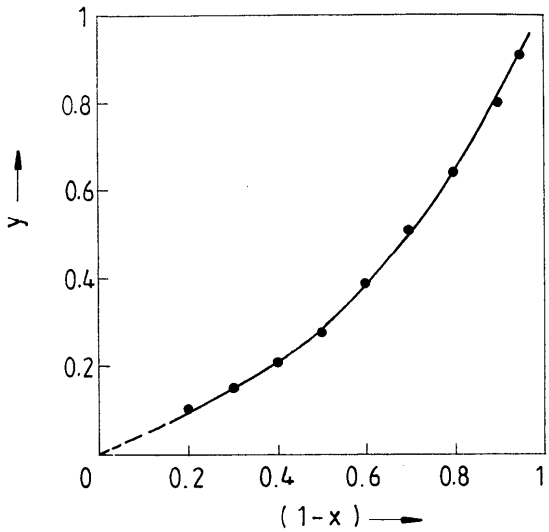

Fig. 2. The molar fraction of V^{4+} and ions versus V_2O_5 content.

We also estimated the $N_{V^{4+}}/N_{V_{total}}$ ratios for the investigated glass samples. These ratios increase when x is decreased an for x = 0.05 it takes the value 0.96, indicating that for this sample 96 % of the vanadium ions are favored to exist in V^{4+} valence state. In case of $2B_2O_3{\cdot}PbO$ [5] and $2P_2O_5{\cdot}PbO$ [12] glass matrices, these ratios are around 0.12±0.1 and respectively 0.27±0.1 for all composition range studies glasses, being smaller than the values obtained for this system. The same ratio for $2B_2O_3{\cdot}Li_2O_3$ glass matrix [9] decrease from 0.58 for x = 0.03 to 0.074 for x = 0.5. The investigation of $xV_2O_5(1\text{-}x)PbO$ [13] glass system prepared in the same conditions like the samples studies in this work evidenced that for $x \geq 0.5$ the V^{4+} ions participate to superexchange magnetic interactions, although their molar fraction is approximately the same ($x_1 \cong 0.25$ for $xV_2O_5(1\text{-}x)PbO$ respectively y = 0.28 for $xB_2O_3(1\text{-}x)[V_2O_5{\cdot}PbO]$, as x = 0.5). The comparative analyse of the results obtained for these systems is different and complex because the preparation conductions for the two systems are different. For example, in the case of $xV_2O_5{\cdot}(1\text{-}x)[2B_2O_3{\cdot}PbO]$ system [5] first was prepared the matrix and then were added

corresponding amounts of V_2O_5 and the final admixtures were melted at 1150^oC for 1 hour. The results obtained for all these systems indicate that the nature of the components, the temperature and time of melting play an essential role in the distribution of vanadium ions in the valence states V^{4+} and V^{5+} reflected by their different magnetic behaviour.

Conclusions

From magnetic susceptibility data we have established that in $xB_2O_3 \cdot (1-x)[V_2O_3 \cdot PbO]$ glasses with $0.05 \leq x \leq 0.8$ both V^{5+} and V^{4+} ions are present, the fraction of the last ones decreases from 0.50 for x = 0.8 to 0.96 for x = 0.05 from the total vanadium content. The temperature dependence of the magnetic susceptibility denotes a Curie-type behaviour in the entire composition range and indicates that the V^{4+} ions are isolated and do not participate to the superexchange interactions.

REFERENCES

1. H. G. Hecht, T. S.Johnston, J. Chem. Phys. 46 (1967), p. 23.
2. L. D. Bogomolova, T.F.Dolgolenko, V.N.Jachkin, V.N.Lazukin, J. Magn. Res. 15 (1974), p. 283.
3. H. Hosono, H. Kawazoe, T. Kanazawa, J. Non-Cryst. Solids, 37 (1980), p. 427.
4. J. M.Dance, J. P. Darnandery, H. Baudry, M. Monneraye, Solid State Commun. 39 (1981), p. 199.
5. O. Cozar, I. Ardelean, Gh. Ilonca, Mat. Chem. 7 (1982), p. 775.
6. O. Cozar, I. Ardelean, V. Simon, V. Mih, N. Vedean, J. Magn. Magn. Mat. 196-197 (1999), p. 169.
7. T. Allersma, J. D. Mackenzie, J. Chem. Phys. 47 (1967), p. 1406.
8. M. Sayer, A. Mansingh, Phys. Rev. B 6 (1972) p. 4629.
9. B. D. Jordan, C. Calvo, Can. J. Phys. 55 (1977), p. 437.
10. R. Singh, J. S. Chakravarthi, Phys. Rev. B 55 (1997) p. 5550.
11. O. Cozar, I. Ardelean, I. Bratu, Gh. Ilonca, S. Simon, Studia Univ. Babes-Bolyai, Physica, XXXIV, 1 (1989) p. 94.
12. I. Ardelean, Gh. Ilonca, V.Simon, O. Cozar, V. Mih, Studia Univ. Babes-Bolyai, Physica, XLIV (1999), p. 13.
13. I. Ardelean, O. Cozar, V. Simon, S. Filip, C. Cefan, Gh.Ilonca (to be published).
14. L. M. Mulay, Magnetic Susceptibility, Interscience, New York, 1973, p. 1773.

STUDIA UNIVERSITATIS BABEŞ-BOLYAI, PHYSICA, XLV, 2, 2000

RADIOECOLOGICAL STUDY OF THE INTEREST ZONES IN SOMES RIVER HYDROGRAPHIC BASIN

L. DARABAN[1], C. COSMA[1], LAURA DARABAN[2], V. ZNAMIROVSCHI[1]

ABSTRACT. Our research refers to the transfer of radioelements from water and mud to talophitae and unicellular algae organism. The measurement of these elements was made for delimiting the radioactive zones of interest in the hydrographic basin of Somes. We demonstrated that the algae are biological indicators of the radioactivity in a river basin.

A series of samples were examined then by high-resolution gamma spectroscopy in our laboratory and at VUB Cyclotron Brussels with a Ge-Re detector for intercomparing.

Were analyzed the uranium and its descendents, also ^{137}Cs resulted from the Chernobyl fallout, which we refund accumulated in the mud of mountains lakes.

It was noticed a migration of the radionuclides from old barren deposits of old polimetalic mines in the Somes river basin.

Introduction

We previously studied the radionuclides transfer, especially ^{137}Cs from the environment in vegetation [1,2]. The research was then extended also on natural radionuclides by a radioecological study of a hydrographic basin of a long river from Transylvania region [3], in purpose to delimit the most radioactive zones of interest.

The samples were processed to measure first the beta global radioactivity by using a low-level system of gas counters, set in anticoincidence and having the minimum detectable activity at 0.01 Bq/sample for 200 minutes counting time. The tables with these measurements were published in [3].

Experimental

The β-global radioactivity values measured by us for surface waters samples are in a range between 0.40 Bq/l and 0.82Bq/l, so under the

[1] Faculty of Physics, Babes-Bolyai University, 1 Kogalniceanu, 3400-Cluj-Napoca, Romania
[2] History Museum of Transylvania, Cluj-Napoca, Romania

maximum admitted concentration which is 1.11 Bq/l. Concerning the β global radioactivity of the mud, the values of the specific activity is situated between 4.1 Bq/g and 1.2 Bq/g. The γ spectrometric measurements for the radionuclides identification were made in 2 laboratories: one from our university, with a Ge(Li) detector KOVO type and for intercomparison one with a detector type ReGe from the cyclotron of the VUB Belgium (Fig.1).

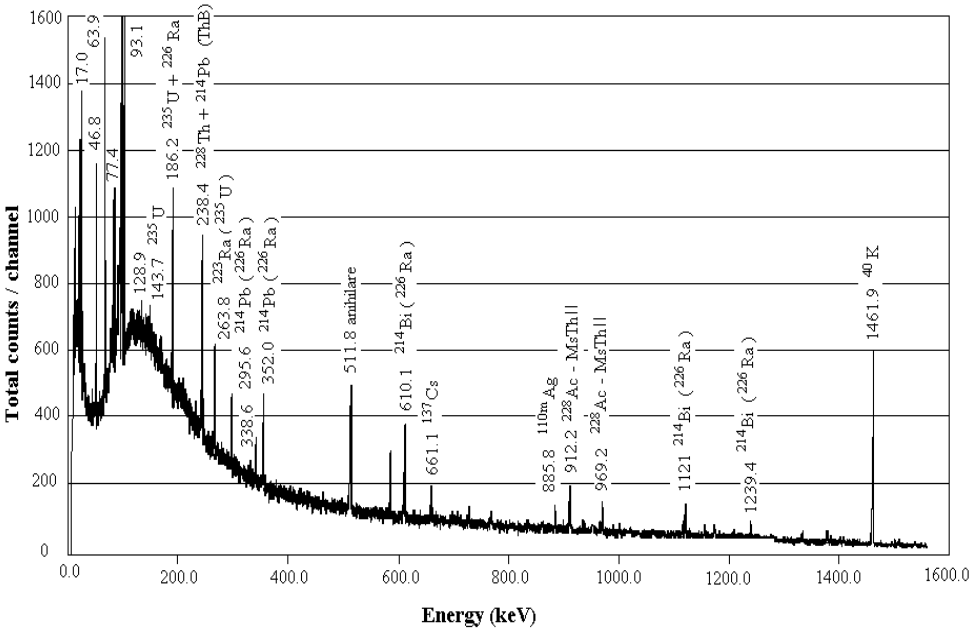

Fig.1. The gamma spectrum for a moss sample from Sant village

In the last case was used a shell-proof board of iron with the thickness of 10 cm, covered with a foil of copper with the thickness of 1 mm to reduce the background. The calibration in efficiency of the detectors, in both cases, was made with well-known sources of ^{152}Eu (Fig.2).

With this, for any sample introduced for measuring, the computer program calculates the peaks area at each energy and gives, after a correction with ε, the absolute activity over the photopeak as in Table No.1.

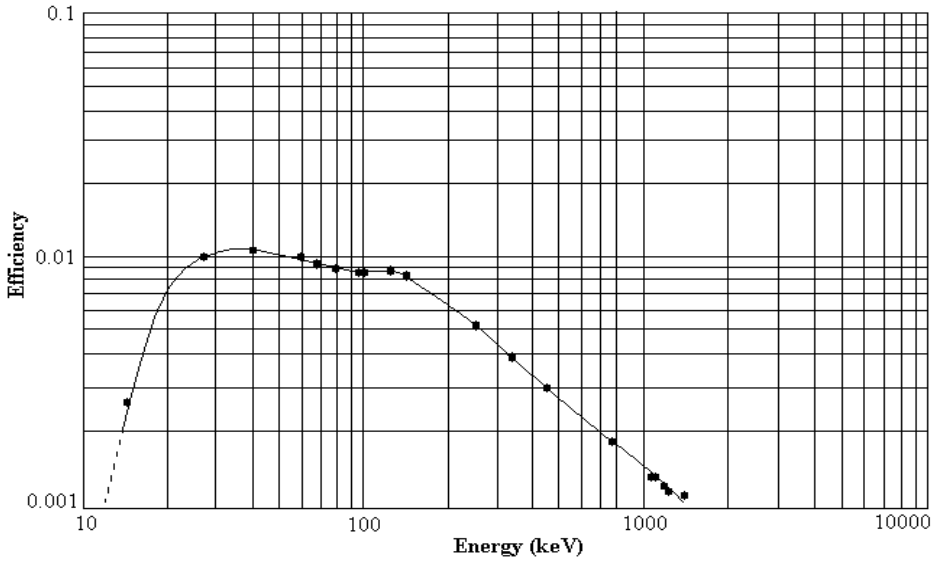

Fig. 2. Efficiency curve for Re-Ge detector

Conclusions

From the γ spectrometric measurements we notice the following: all the samples contain descendents from uranium family and from ^{137}Cs, provided from the Chernobyl accident and gathered more in sediments washed by precipitations. In this way we detected ^{137}Cs also in the mud from the lake of accumulation Gilau, which is a source of drinking water for Cluj-Napoca town.

Table1

Somme γ activity values for radionuclides from the sample from Sant village:

The radionuclide	Confidence degree	Energy (KeV)	Quantic emission probability (%)	Activity μCi/kg)
K-40	0.970	1460.81	10.67	0.3869
		661.65	85.12	0.0041
Cs-137		77.11	17.50	0.0664
Pb-212	0.982	238.63	44.60	0.0361
		300.09	3.41	
		609.31	46.30	0.0396
Bi-214	0.792	1238.11	5.94	0.0604

From β-global measurements was emphasized a radioactivity higher in the region of Rodna mountains and Gilau, where it is known that exist ores of polimetalic sulfides and arseniurs and also sterile halides, so it is not excluded an effect of uranium and its descendents washing from these deposits, so substantial contribution of telluric activity.

We followed the phenomenon of transfer and concentration of the radionuclides from water and mud in algae and fishes.

The results obtained show that the beta global activity of the talophytae algae ashes of 6.22 Bq/g is significantly higher besides the values corresponding to the phylamentous algae (of 2.49 Bq/g) in the source point Gilau. The explanation is that the talophytae algae presents roots, which absorb radionuclides from the sapropelic mud in which they grow, while the phylamentous algae being floating on water surface, absorb and metabolize only the radionuclides vehicled in the water. The different way of feeding of algae has consequences on the transfer processes of radionuclides. From this point of view we notice that the talophytae algae represents a main biological indicator for level of radioactivity of a mellow basin.

In the zones of interest for us, with a higher radioactivity in general, the talophytae algae and especially the mud from these two zones presents high values of radioactivity, which indicates a high accumulation rate of radionuclides in these compartments of aquatic ecosystem.

In the two zones of interest, we point out the presence of uranium and descendents, washed from mining secular deposits. In this way it was studied the transfer from water-mud-algae system, the talophytae algae presenting higher values than the filamentous algae [4].

REFERENCES

1. I.Chereji, L.Daraban, J.Radioanal.Nucl.Chem.Lett., **145** (1990), 293.
2. I. Chereji, L. Daraban, S. Dreve, S. Boscaneanu, C. Cosma, E. Nagy-Vari, J.Radioanal.Nucl.Chem.Lett., **212** (1996) 85.
3. Marta Bayer, T. Fiat, L. Daraban, L. Floca, Laura Daraban, Balkan Phys.Lett., **5** (1997) 1797.
4. L. A. Floca, O. Cozar, M. Trifu, L. Daraban, T. Fiat, Marta Bayer, L. Berkesy, Studia Univ. B-B., ser. Biologia, **41** (1996) 135.

STUDIA UNIVERSITATIS BABEŞ-BOLYAI, PHYSICA, XLV, 2, 2000

DIFFERENTIAL THERMAL ANALYSE OF LEAD-BISMUTHATE OXIDE GLASSES

R. POP[1], V. SIMON[2], E. DOGARU[3]

ABSTRACT. Glass transition, nucleation temperatures as well as exothermal and endothermal processes established from differential thermal analysis (DTA) on $xBi_2O_3 \cdot yPbO$ glass matrices ($0.5 \leq x/y \leq 4$) are reported. The obtained results indicate the occurrence of structural changes from short range to long range order depending on the x/y ratio between Bi_2O_3 and PbO content.

Introduction

The heavy metal glasses have attracted considerable attention due to their interesting physical properties leading to different applications like radiation shielding windows, scintillation counters, optical transmission devices, ultrafast optical switches [1-3]. It has been reported that the glasses in the system Bi_2O_3-PbO can be obtained only at high cooling rates [4]. An attractive reason in studying these glasses also consists in the fact that they do not contain any conventional glass formers such as SiO_2, B_2O_3, P_2O_5, GeO_2, etc

In this paper we present the results obtained for $xBi_2O_3 \cdot yPbO$ systems, where $0.5 \leq x/y \leq 4$, from differential thermal analysis, as function of the ratio between Bi_2O_3 and PbO content.

Experimental

The starting materials used to prepare $4Bi_2O_3 \cdot PbO$, $3Bi_2O_3 \cdot 2PbO$ and $Bi_2O_3 \cdot 2PbO$ matrices were analytically pure reagents $(BiO)_2CO_3$ and PbO. The suitable mixtures were melted in sintercorundum crucibles in an electric furnace, in air, at 1100^oC for 10 minutes. The melts were quenched between two stainless steel plates at room temperature. The as prepared samples are slightly opaque.

Thermal analysis measurements were carried out using a MOM derivatograph. The TG, DTG and DTA curves were recorded from powder samples, with a rate of 10^oC/min.

[1] Technical University of Constructions, Bucarest, Romania
[2] Babes-Bolyai University, 3400 Cluj-Napoca, Romania
[3] Research and Projection Institute for Mines, 3400 Cluj-Napoca, Romania

Results and discussion

The TG and DTG curves recorded from as quenched samples do not evidence any weight loss up to 1000°C (Fig.1). The data obtained from the DTA curves are summarised in Table 1, wherein the T_g temperature is assigned to the quasi-endothermic peak due to the glass transition [5] and characterises the beginning of the structural transformations, T_n temperature is the nucleation temperature at which the crystallisation starts, T_{exo} are the temperatures of the exothermic crystallisation maxima and T_{endo} correspond to endothermic peaks assigned to structural arrangement changes of the crystalline phases previously developed, i.e. to reconstructive reactions inside the existing crystalline phases [6, 7]. The lack of endothermal events in the DTA curve of $Bi_2O_3 \cdot 2PbO$ sample denotes the structural stability, at least up to 1000°C, of the crystalline phases grown in this matrix.

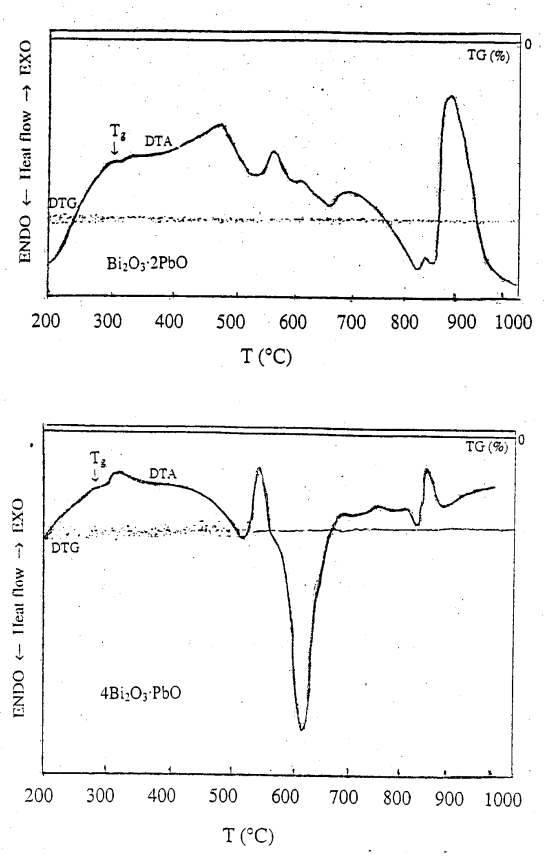

Fig. 1. Differential thermal analysis curves for $xBi_2O_3 \cdot yPbO$ samples (x/y = 0.5 and 4).

Table 1.
Glass transition, nucleation, crystallisation and endothermic peak temperatures for $xBi_2O_3 \cdot yPbO$ samples.

Sample	x/y	T_g	T_n	T_{exo}	T_{endo}
$Bi_2O_3 \cdot 2PbO$	0.5	300	320	333 470 562 613 690 840 894	
$3Bi_2O_3 \cdot 2PbO$	1.5	280	300	318 550 695	590 625
$4Bi_2O_3 \cdot PbO$	4	275	295	310 540 676 747 848	620 738

As the samples crystallise, they become opaque as a consequence of random light scattering [8]. Even before crystallisation there might be a possible change in the sample appearance due to nucleation and/or phase separation [7], which was also the case of the investigated samples.

We also suppose that the investigated samples could be characterised by an intermediate-range order, perhaps associated with strained units, as observed in other oxide glasses [9]. In order to support this assumption further spectroscopic investigations are necessary.

Conclusions

The glass matrices $xBi_2O_3 \cdot yPbO$ were obtained in a large composition range ($0.5 \leq x/y \leq 4$). The slight opaque appearance of the as prepared samples could be assigned to nucleation and/or phase separation even before the crystallisation. We assume that the investigated samples could be characterised by an intermediate-range order, potentially associated with strained units.

The increase of glass transition temperature with PbO content points out a lower mobility and consequently a diminished long-range order arrangement ability of lead ions in comparison to the bismuth ones in the lead-bismuthate samples.

Endothermic peaks associated in this case to structural destroy or rearrangement of previously developed crystalline phases are observed only for x/y = 4:1 and 3:2 while they are lacking for x/y = 1:2, that denotes the high structural stability of the crystalline phases developed in $Bi_2O_3 \cdot 2PbO$ matrix up to 1000^oC.

REFERENCES

1. Karmalov, R.M. Almeida, J. Heo, J. Non-Cryst. Solids, 202, 233 (1996).
2. J. Fu, H. Yatsuda, Phys. Chem. Glasses, 36, 211 (1995).
3. J. Fu, Phys. Chem. Glasses, 37, 84 (1996).
4. Y. B. Dimitriev, V.T. Mihailova, J. Matter. Sci. Lett., 9, 1251 (1990).
5. R. Sato, T. Komatsu, K. Matusita, J. Non-Cryst. Solids, 181, 64 (1995).
6. L. Barbieri, A.B. Corradi, C. Leonelli, C. Siligardi, T. Manfredini, G.C. Pellacani, Mat. Res. Bull., 32, 6, 637 81997).
7. J. M. Jewell, M.Spess, R.L. Ortolano, J.E. Shelby, J. Am. Ceram. Soc., 74, 92 (1991).
8. A. K. Varshneya, Fundamentals of Inorganic Glasses, Academic Press,London, p.61 (1994).
9. R. K. Brow, D. R. Tallant, J.J. Hudgens, S.W. Martin, A.D. Irwin, J. Non-Cryst. Solids, 177, 221 (1994).

STUDIA UNIVERSITATIS BABEŞ-BOLYAI, PHYSICA, XLV, 2, 2000

ABSORPTION PROPERTIES OF DNA IN A MICROWAVE FIELD

CRISTINA M. MUNTEAN[1], ANDREI IOACHIM[2], ONUC COZAR[3], DUMITRU MOLDOVEANU[4]

ABSTRACT. In this work, microwave characteristics of insertion loss and return loss have been measured between 7.3-12.4 GHz, for aqueous solutions of chromosomal and total DNA and for the corresponding buffer, respectively. Starting with the physics analysis of insertion loss and return loss, we have calculated the relative electric-field attenuation constants and the percentage of the microwave power attributed from this data analysis to DNA-hydration layer systems.

Introduction

The direct absorption of moderate-to-low-frequency nonionizing electromagnetic radiation in DNA molecules, is a potential source of biological effects [1,2].

A variety of microwave measurements of aqueous solutions of DNA have been reported, with different results [3-13]. As an introduction to the study of this phenomenon, we have carried out at GHz-frequencies (7.3-12.4 GHz), basic microwave measurements of insertion loss and return loss [12-14].

The aim of this paper is to report some of our data on microwave absorption of different DNA-hydration layer systems, as reflected by scalar microwave measurements of insertion loss and return loss. Relaxation processes attributable to the Debye type components of DNA hydration layer system have been found.

[1] National Institute for Research-Development of Isotopic and Molecular Technologies, R-3400 Cluj-Napoca, P. O. 5, Box 700, Romania

[2] National Institute for Research-Development of Materials Physics, P. O. Box MG-7, R-76900 Bucharest-Magurele, Romania

[3] University "Babes-Bolyai", Kogalniceanu Street Nr.1, R-3400 Cluj-Napoca, Romania

[4] Institute of Developmental Biology, Bucharest 77748, Splaiul Independentei 296, Romania

Materials and methods

Basic scalar microwave measurements of insertion loss and return loss were carried out at room temperature, with a Hewlett Packard Network Analyzer. Low-intensity microwaves (TE10 mode) were used. A teflon sample holder was placed in the X-band waveguide, in a configuration of weak electric field. An impedance bridge was used to monitor the power reflected from the sample. The combined mismatches of the sample holder with and without test samples were considered small, with less than 1% of the incident power being reflected in almost all the experimental frequency range (7.3-12.4 GHz). For a given sample, microwave insertion loss and return loss were taken simultaneously. A signal mediated over 16 scans was considered. A schematic diagram of the experimental microwave system used in these experiments is presented in Fig. 1 [15].

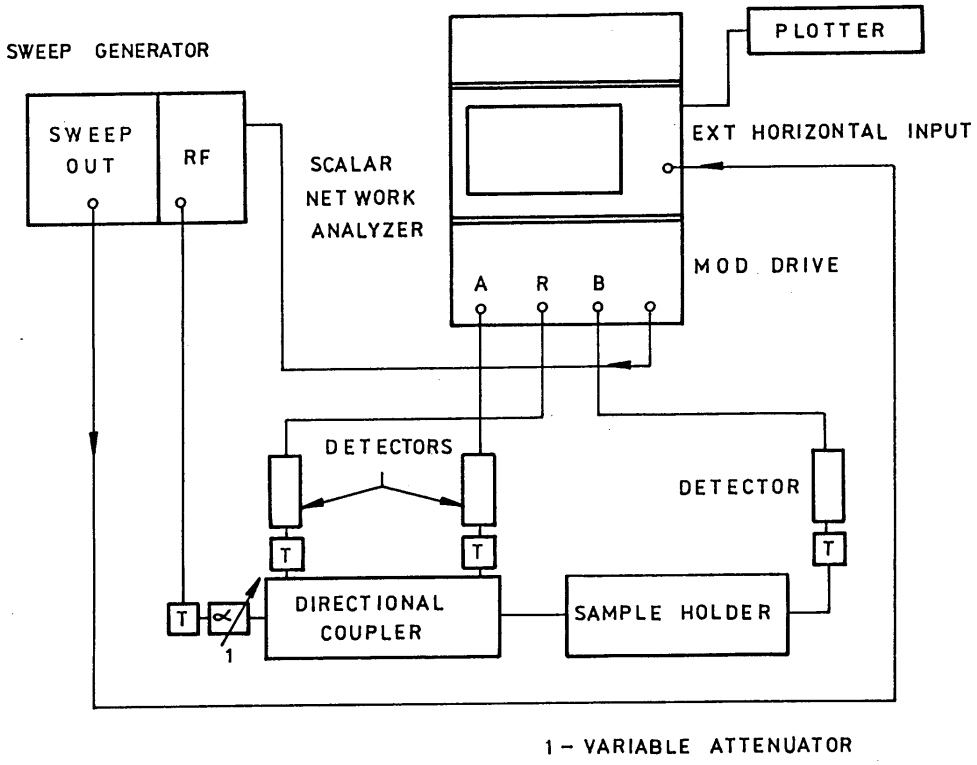

Fig. 1. Schematic diagram of the experimental microwave system.

Insertion loss (M_I) and return loss (M_R) are measured in dB and are defined as follows [20]: M_I = 1o $\log_{10}$ (Pi/Pt) and M_R = 10 $\log_{10}$ (Pi/Pr). Here, Pi is the incident power, Pt is the transmitted power through the tested aqueous solution and Pr is, respectively, the reflected power from the sample holder and the liquid sample.

We have investigated several chromosomal and total DNA samples, extracted by standard techniques from different types of bacterial cells cultures. Samples were isolated and purified in our laboratories. Commercial DNA has also been used. After each extraction, DNA molecules were dissolved in a storage buffer (10 mM Tris-HCl, 1 mM EDTA, pH = 8) and the sample quality was checked by UV spectrophotometric method. For this purpose a Specord UV-VIS with a pair of tandem cells was used. Agarose gel electrophoresis with standard markers has also been used in some cases. Our samples were nonuniform ones, including molecular fragments of a statistic length distribution.

Microwave response of a given aqueous solution of DNA was compared with the microwave response of the standard storage buffer, respectively, considered for the same volume. On the basis of the measured quantities of insertion loss and return loss, we have estimated for each DNA sample the relative electric-field attenuation constants [13] and the ratio $\Delta P_{abs} / P_i$, between the difference in the absorption of DNA solution $P_{DNA\ solution}$ and that in free buffer P_{buffer} and the incident power, which was the same for the compared samples [20]. This calculation is based on a data analysis developed in our laboratories [12-15]. Here, $P_{DNA\ solution}$ includes the microwave power absorbed in each of the three component volumes - solute volume, hydration layer volume and free solvent volume [10, 13]. $\Delta P_{abs} = P_{DNA\ solution} - P_{buffer}$ is the microwave power absorbed in DNA-hydration layer system.

In order to compare our results with the data published in the literature, we have calculated the relative attenuation constants of all the samples investigated by us. The relative attenuation constants were estimated for each sample in three distinct ways, the data reflecting the differences which might appear in the reported values of the attenuation parameter, because of the definition used for it by the investigators or due to the measurement method and not to the sample itself. No significant differences have been found in the values of these attenuation parameters.

Results and Discussion

In this work microwave absorption signatures of DNA-hydration layer systems have been calculated between 7.3-12.4 GHz, starting with the physics analysis of the measured quantities of insertion loss and return loss [12-15]. The interaction mechanisms of chromosomal and total DNA molecules with a microwave field, are of interest. The microwave absorption of an aqueous solution of DNA polymers is composed of three parts: absorption in free water, absorption in the substance and absorption in the hydration layer.

The results of our calculations, attributable from this data analysis to the DNA-hydration layer systems are shown in Fig. 2-3, for some distinct chromosomal or total DNAs.

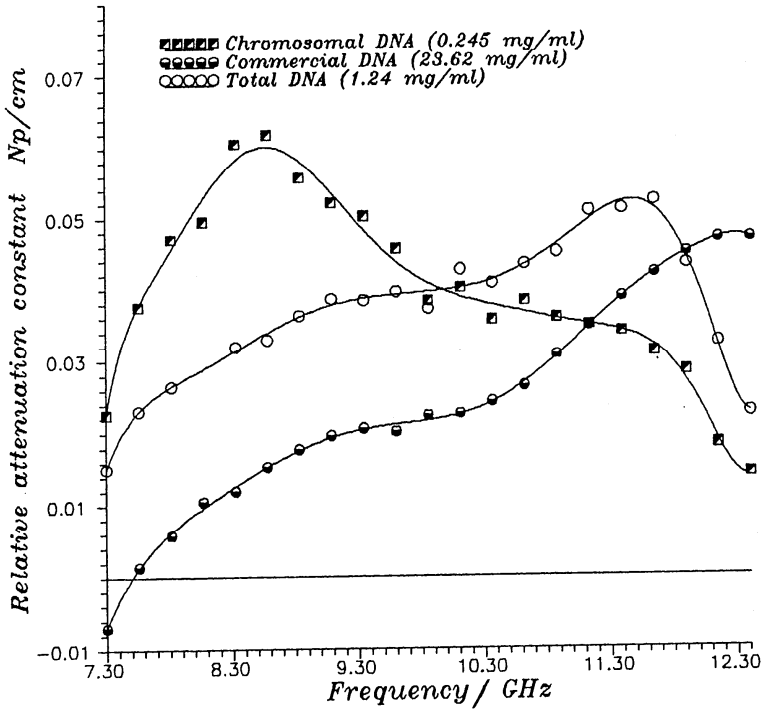

Fig. 2. The frequency-dependence of the relative electric field attenuation constant for chromosomal and total DNAs, dissolved in standard storage buffer (10 mM Tris-HCl, 1 mM EDTA, pH=8).

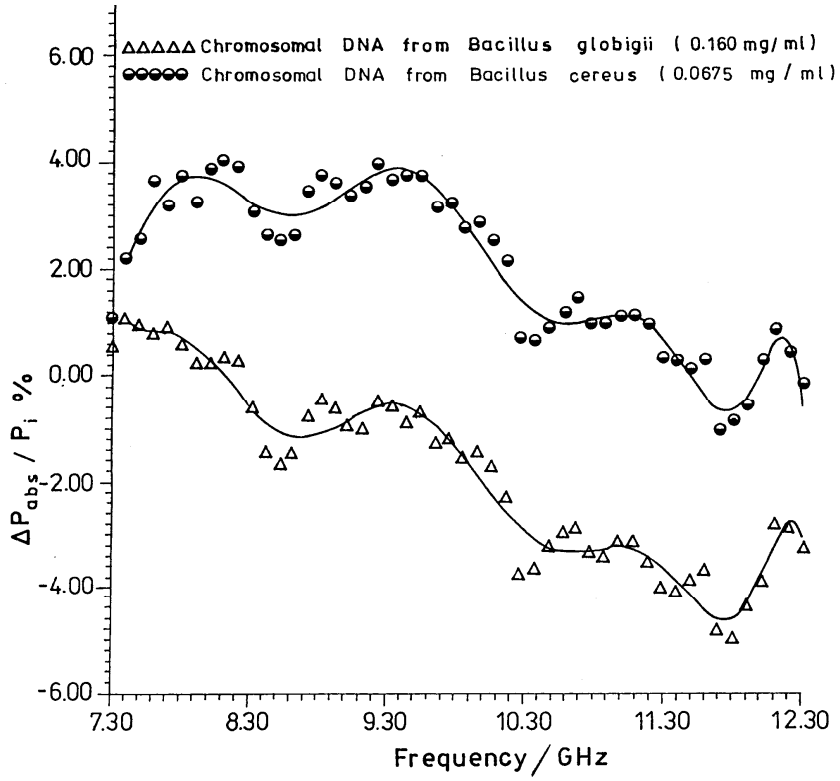

Fig. 3. The frequency-dependence of the percentage of microwave absorption attributed to different DNA-hydration layer systems: chromosomal DNA from Bacillus globigii (0.160 mg/ml); chromosomal DNA from Bacillus cereus (0.0675 mg/ml). DNA was dissolved in a standard storage buffer (10 mM Tris-HCl, 1 mM EDTA, pH = 8). A fitting routine based on polynomial technique has been used.

A broadband influence of low-intensity microwaves is reported here for all the molecular systems investigated by us, over the entire experimental frequency range. In some cases, microwave absorption curves seem to be composed of two or more distinct broad bands. This might be due to the presence of two or more different distributions of DNA chains, inside the solution. We didn't observe for these types of samples any sharp feature which might prove the participation of acoustic modes to DNA dynamics.

These data, characterizing different DNA-hydration layer systems, offer information about dielectric relaxation processes at GHz frequencies. On the basis of the Debye model of dielectric constants, it would be possible in the future to calculate the hydration layer thickness and its relaxation time [10, 13].

In this study we calculate the microwave absorption of some systems containing double helical DNA, water molecules and ions. Our systems are inhomogeneous ones, being characterized by large dipole fluctuations of their molecular groups. Dielectric characteristics of different regions inside the DNA-hydration layer system are due to the dipole moments of its components. These are modestly polar bases, less polar sugars, negatively charged phosphates and water molecules [14-16]. However, experimental measurements of the dielectric properties of biopolymers are tipically limited to the overall response of the sample to the applied external field. Decomposition of the dielectric characteristics for a DNA-water system is usually possible from MD simulations. The water molecules in such a system exhibit a dielectric constant that have a smaller value than that of pure water, because of the presence of DNA and of ionic species, which restrict the motion of water [14-16].

Acknowledgements

The authors wish to thank to Mr. O. Petrean for writing the computing algorithm of the attenuation and absorption parameters and to Mrs. Dorica Vintila for help in sample preparation. We acknowledge fruitful discussions on microwave measurements with Dr. Gabriela Nicoara from the National Institute for Research-Development of Materials Physics, Bucharest-Magurele, Romania.

REFERENCES

1. Koschnitzke, C., Kremer, F., Santo, L., Quick, P., Poglitsch, A., Z. Naturforsch. 38 c, 883 (1983).
2. Belyaev, I.Ya., Alipov, D., Shcheglov, V.S., Electro- and Magnetobiology 11, 97, (1992).
3. Edwards, G.S., Davis, C.C., Saffer, J.D., Swicord, M.L., Phys. Rev. Lett. 53, 1284 (1984).
4. Edwards, G.S., Lindsay, M., Prohofsky, E.W., Phys. Rev. Lett. 54, 607 (1985).

5. Edwards, G.S., Davis, C.C., Saffer, J.D., Swicord, M.L., Biophys. J., 47, 799 (1985).
6. Davis, C.C., Edwards, G.S., Swicord, M.L., Sagripanti, J., Saffer, J., Bioelectrochem. Bioenergetics, 16, 63 (1986).
7. Sagripanti, J.L., Swicord, M.L., Int. Radiat. Biol. 50, 47 (1986).
8. Gabriel, C., Grant, E.H., Tata, R., Brown, P.R., Gestblom, B., Noreland, E., Nature 328, 145 (1987).
9. Foster, K.R., Epstein, B.R., Gealt, M.A., Biophys. J. 52, 421 (1987).
10. Garner, H.R., Ohkawa, T., Tuason, O., Lee, R.L., Phys. Rev. A 42, 7264 (1990).
11. Bigio, I.J., Gosnell, T.R., Mukherjee, P., Saffer, J.D., Biopolymers 33, 147 (1993).
12. Muntean, C., Ioachim, A., Cornea, C., Fifth International Conference on the Spectroscopy of Biological Molecules Proc., T. Theophanides, Jane Anastassopoulou, N. Fotopoulos (Eds.), Kluwer Academic Publishers, Dordrecht, the Netherlands, p. 71 (1993).
13. Muntean, C., Ioachim, A., Petrean, O., 6th European Conference on the Spectroscopy of Biological Molecules Proc., Jean Claude Merlin, Sylvia Turrell and Jean Pierre Huvenne (Eds.), Kluwer Academic Publishers, Dordrecht, the Netherlands, p. 333 (1995).
14. Muntean, C.M., Banciu, G., Cozar, O., Ioachim, A., Spectroscopy of Biological Molecules: New Directions, J. Greve, G. J. Puppels and C. Otto (Eds.), Kluwer Academic Publishers, Dordrecht, the Netherlands, p. 223 (1999).
15. Muntean, C.M., Cozar, O., Banciu, G., Pop, S., Proc. Suppl. Balkan Phys. Lett. 5, 211 (1997).
16. Yang, L., Weerasinghe, S., Smith, P.E., Pettitt, B.M., Biophys. J. 69, 1519 (1995).
17. Davis, M.E., VanZandt, L.L., Phys. Rev. A 37, 888 (1988).
18. Fisun, O.I., Katanaev, M.O., Makromol. Chem. 192, 2191 (1991).
19. Edwards, G., Ying, G., Tribble, J., Phys. Rev. A 45, R8344 (1992).
20. Muntean, C.M., Ioachim, A., Report I.I.M.T. (1989).

STUDIA UNIVERSITATIS BABEŞ-BOLYAI, PHYSICA, XLV, 2, 2000

LOW pH-INDUCED DNA STRUCTURAL CHANGES: A RAMAN MICROSPECTROSCOPIC STUDY

C. M. MUNTEAN[1], G. J. PUPPELS[2], J. GREVE[3], G. M. J. SEGERS-NOLTEN[3], O. COZAR[4]

ABSTRACT. In this work, a confocal Raman microspectrometer was used to investigate low pH-induced DNA structural changes. Measurements were carried out on calf-thymus DNA, at neutral pH and at pH 3. Raman spectra of calf-thymus DNA in the interval 440-1680 cm^{-1} are presented. The intensities of the Raman bands of the ring breathing vibrations of the guanine (681 cm^{-1}), adenine (727 cm^{-1}), thymine (749 cm^{-1}) and cytosine (784 cm^{-1}) are discussed. Besides, the B-form marker near 834 cm^{-1} and the base vibrations in the higher wavenumber region (1200-1680 cm^{-1}) are analysed. Effects of low pH upon protonation mechanism of opening AT- and changing the protonation of GC base pairs in DNA are considered.

Introduction

Several mechanisms involving DNA, might be explained as a consequence of structural transitions from B-form to protonated forms, at low pH. It has been found an equilibrium mixture of B-DNA, the altered conformation and intermediate structure, proving the possible significance of alternative DNA structures for biological processes [1]. In such mechanisms, pH manifests itself as a powerful and sensitive lever of regulation [2].

In a protonated GC base pair, protonation of cytosine is accompanied by a conformational change of the guanine from the C2'-*endo*-anti to C2'-*endo*-syn [3-5]. This conformational change enables hydrogen bonding of the N(7) of guanine and the cytosine N(3) in a Hoogsteen base pair [1, 3-6]. This new pair is less stable (two instead of

[1] National Institute for Research and Development of Isotopic and Molecular Technologies, R-3400 Cluj-Napoca,P.O. 5, Box 700, Romania
[2] Rotterdam University Hospital "Dijkzigt", General Surgery 10M, 3015 GD Rotterdam, The Netherlands
[3] Department of Applied Physics, University of Twente, P.O. Box 217, 7500 AE Enschede, The Netherlands
[4] University “Babeş-Bolyai", Kogălniceanu Street Nr. 1, R-3400 Cluj-Napoca, Romania

three H-bonds) than Watson-Crick base pair [3], but the secondary structure is not destroyed by protonation [7]. The proposed protonated Hoogsteen type G·CH$^+$ (protonated GC) pair would tighten the helix and slightly untwist it, in the screw sense similar to the intercalation of dyes in DNA. Hoogsteen base pairs should be stabilized at low pH [8,9].

It is shown that the AT pairs are protonated just before the denaturation and that their behaviour seems to be different from that of protonated GC pairs. AT pairs seem to be unable to assume a new pairing when protonated. Only one H-bond remains between A$^+$ and T, i.e., between the 6-NH_2 of adenine and the 4-C=O of thymine. This pairing must be more unstable than that of the protonated GC pairs, in which two H-bonds remain [7]. It is shown that just before the acidic denaturation, the most unstable regions in DNA are the AT-richest ones.

As a conclusion, binding of H$^+$ to DNA, leads reversibly, to alternative DNA structures, especially to disrupted AT base pairs and to Hoogsteen *syn* dG:dCH$^+$ base pairs [1, 3, 6], which exist in the opinion of some authors, under physiological conditions, in purified and chromosomal DNA [1]. Besides, irreversible changes in DNA occur, when at low pH, upon further protonation, the disruption of not only AT but also of protonated Hoogsteen GC base pairs take place [1].

However, in the literature there is no consensus on the precise nature of the changes, that occur in DNA as the pH is lowered. It seems that a subtle interplay between chemical parameters (pH and ion concentration) may result in appreciable changes in DNA conformation [6]. The elucidation of the nature of these changes, in the case of calf-thymus DNA, is the topic of this paper.

In this work, vibrational markers of protonated DNA base pairs are analysed by use of Raman microspectroscopy. Effects of lowering the pH upon protonation mechanism of opening AT and changing the protonation of GC base pairs in DNA are discussed.

Materials and methods

Preparation of DNA molecules at neutral pH and at low pH

Calf-thymus DNA (Sigma Type I, D-1501, St. Louis, MO, USA) at a concentration of 15 mg/ml was dialysed against glycine buffer (50 mM glycine, 10 mM NaCl) to obtain the protonated DNA molecules at pH 3. Reference sample at neutral pH was obtained in phosphate buffer for the same DNA and monovalent cations concentrations. pHs were measured in the dialysing buffer and in the DNA sample, respectively.

Experimental

All Raman experiments with DNA molecules were carried out on a confocal Raman microspectrometer developed in the Biophysical Technology group, Department of Aplied Physics, University of Twente, Enschede, the Netherlands. This instrument was largely identical with a first developed micro Raman set up [1]. The microscope was equipped with a 63x Zeiss Plan Neofluar water immersion objective. Laser light of 514.5 nm from an Argon ion laser was used for excitation.

The spectra have been processed by means of the software package RAMPAC [10]. Each measurement on a DNA sample was followed by a second one (background signal measurement), just next to that of DNA, in order to determine the signal contributions from buffer, which were then substracted from the resulting DNA sample spectrum.

Each spectrum is the result of 12-35 measurements, which were then averaged (Figure 1). The averaged spectra thus obtained showed only minor variations, not of any consequence for the interpretations given bellow. The wavenumber calibration of the Raman spectra was recorded with the same instrument setting on the basis of an indene. The spectra were corrected for the wavenumber dependent detection efficiency of the confocal Raman microspectrometer [1].

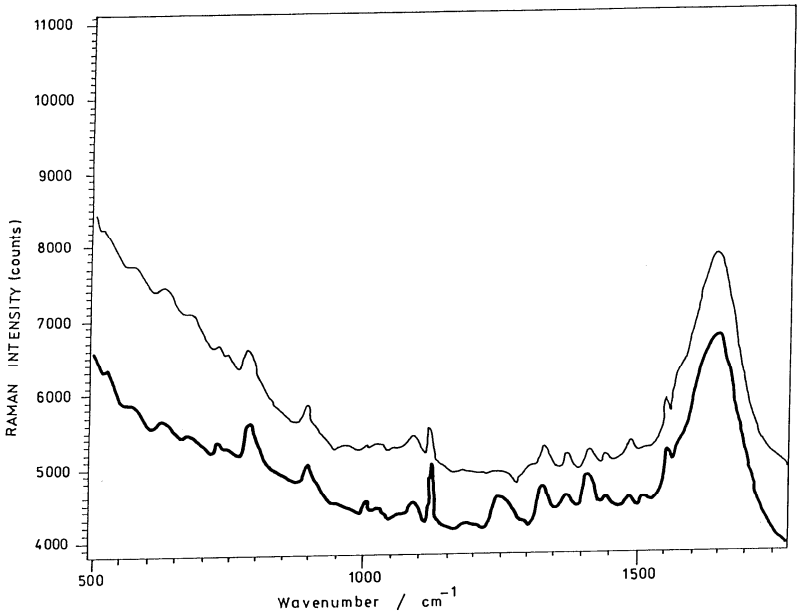

Fig. 1. Acquisition Raman spectra of calf-thymus DNA in aqueous solution, at neutral pH, in the presence of 10 mM Na^+. The macromolecular concentration is 15 mg / ml. The two spectra are differentiated. by their characteristic acquisition times. Data include the background signal.

Difference spectra

The events occuring in the samples upon lowering the pH are clarified by the difference spectra. An internal intensity calibration was needed to scale the measured spectra, in order to compute difference spectra [1]. The spectra were scaled to have equal intensity in the 1094 cm^{-1} band of the DNA backbone PO_2^- symmetric stretching vibration. The intensity of this band is not sensitive to DNA protonation down to at least pH 2.35 [11]. Protonation of the DNA backbone phosphate groups occurs around pH 1. Besides, in the conditions employed for the present experiments, the interactions between divalent metal cations and the phosphodioxy anions should be dominated by electrostatics [12].

The events occuring in the DNA systems upon lowering the pH, were monitored also by a comparative analysis of the spectra obtained for samples with different stages of DNA protonation.

Results and discussion

Measurements were made on calf-thymus DNA at neutral pH and at low pH (around pH 3), in the presence of low concentrations of Na^+ ions. Some of the spectra obtained by us are presented in Figures 1-3.

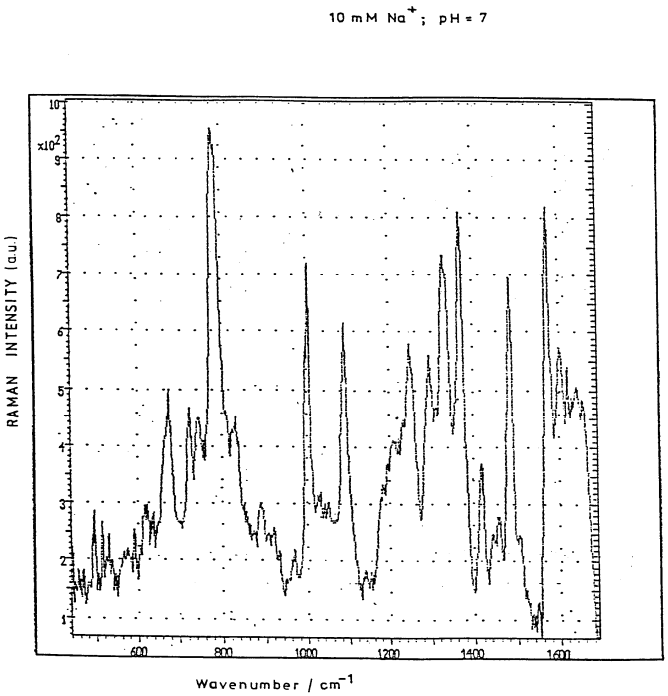

Fig. 2. Raman spectrum of calf-thymus DNA at neutral pH, in the presence of 10 mM Na^+. The macromolecular concentration is 15 mg / ml. Data have background signal substracted.

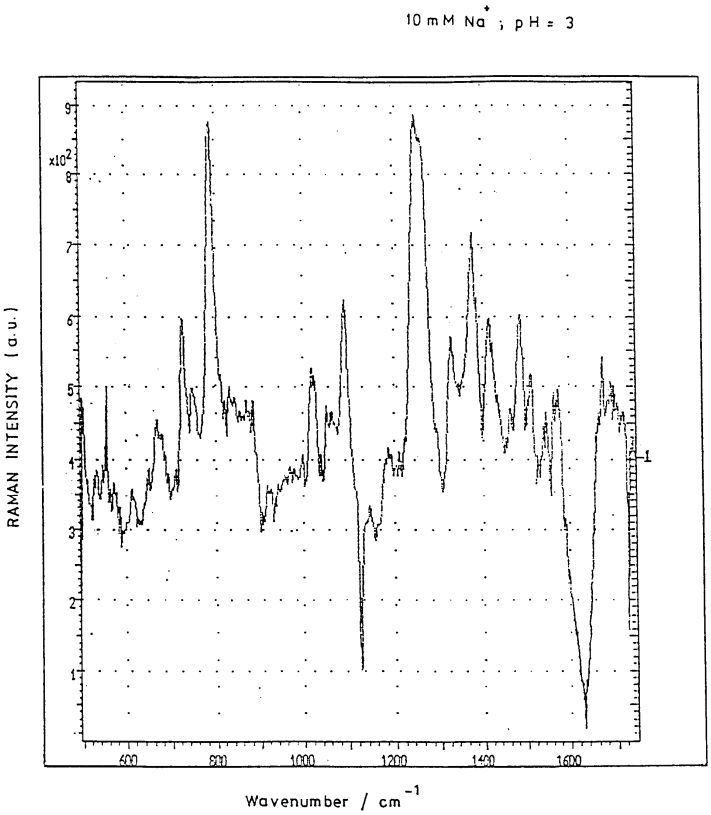

Fig. 3. Raman spectrum of calf-thymus DNA at pH 3, in the presence of 10 mM Na^+. The macromolecular concentration is 15 mg / ml. Wavenumber regions describing nucleoside conformation, backbone geometry, PO_2^- interaction, base electronic structures and base pairing are presented.
Data have background signal substracted.

Raman data presented in this work are useful for the study of low pH-induced DNA structural changes. Large changes in the Raman spectra of calf-thymus DNA were observed upon lowering the pH. These are due to protonation and unstacking of the DNA bases and to changes in DNA backbone conformation. The Raman bands of the ring breathing vibrations of the guanine (681 cm^{-1}) [1, 6, 13], adenine (729 cm^{-1}) [1, 13], thymine (749 cm^{-1}) [1, 13] and cytosine (784 cm^{-1}) [1, 6, 13] are markers for the C2'-*endo*-anti conformation of the nucleotides, typical of B-DNA [1, 13]. Their intensities do respond to unstacking of the bases [11].

The guanine line is hypochromic, its intensity decreases upon unstacking of bases or during DNA melting. The other bands show a hyperchromic behaviour (present an increase in intensity), especially the adenine band shows a large increase in intensity upon unstacking. Further information is obtained from the band centered around 830 cm^{-1} [1, 6, 13], which is ascribed to an antisymmetric PO_2^- - stretching mode of the B-form DNA backbone [1,6].

The base vibrations in the higher wavenumber region (1200-1700 cm^{-1}) are sensitive to both protonation and unstacking [11]. Raman bands of thymine (1241 cm^{-1}) and protonated cytosine (1262 cm^{-1}) are hyperchromic (present an increase in intensity) upon binding of H^+ to DNA molecule [1, 13]. The adenine bands at 1304 and 1341 cm^{-1} [1] decrease in intensity because of DNA melting at A+T regions, due to protonation. In the same time, the protonated adenine Raman band at 1409 cm^{-1} [1] have a hyperchromic behaviour. The band at 1488 cm^{-1}, which obtains most of its intensity from a guanine vibration [1, 6, 13] was found to loose intensity upon protonation of the GC base pairs. This vibration is known to be very sensitive to any ligation or complexation involving the guanine N7 [1, 13]. The band at 1578 cm^{-1}, attributed to both guanine and adenine [1, 6] has a hypochromic behaviour (presents a decrease in intensity) upon binding of H^+ to DNA.

Conclusions

We have obtained Raman spectra of excellent quality for calf-thymus DNA, at neutral pH and at low pH.

A possible conformational transition of the guanine from the C2'-*endo*-anti to C2'-*endo*-syn, followed by hydrogen bonding between N(7) of guanine and cytosine N(3) is not sustained in our data, due to the unusual behaviour of the cytosine Raman band at 785 cm^{-1}, upon lowering the pH. However, the other Raman bands, characteristic for the Hoogsteen model of the protonated GC base pairs, like the guanine band at 681 cm^{-1}, the band of protonated cytosine at 1262 cm^{-1} and the guanine band at 1488 cm^{-1} have the expected behaviour of their intensities at pH 3, as compared to neutral pH.

Other changes occurring in DNA structure at pH 3 are: adenine protonation, adenine and thymine unstacking, AT unpairing, DNA backbone conformational change.

REFERENCES

1. Puppels, G. J., Otto, C., Greve, J., Robert-Nicoud, M., Arndt-Jovin, D. J., and Jovin, T. M., 33, 3386, 1994.
2. Muntean, C., European Community Report, Brussels, 1994: pp 40.
3. Saenger, W., *Principles of Nucleic Acid Structure*, C.R. Cantor (ed.), Springer-Verlag, New York (1984).
4. Sarma, R.H. (ed.), *Nucleic Acid Geometry and Dynamics*, Pergamon Press, New York (1980).
5. Muntean, C. M., *Raman Spectroscopy of DNA Molecules. Applications and Perspectives*, Doctoral Report University "Babes -Bolyai" from Cluj-Napoca, Faculty of Physics, Romania, pp 136 (1996).
6. Segers-Nolten, G. M. J., Sijtsema, N. M., and Otto, C., Biochemistry, 36, 13241, 1997.
7. Hermann, P., and Fredericq, E., Nucleic Acids Res., 4, 2939, 1977.
8. Courtois, Y., Fromageot, P., and Guschlbauer, W., Eur. J. Biochem., 6, 493.
9. Hanvey, J. C., Klysik, J., and Wells, R. D., J. Biol. Chem., 263, 7386, 1988.
10. De Mul, F. F. M., and Greve, J., J., Raman Spectrosc., 24, 245, 1993.
11. O'Connor, T., and Scovell, W. M., Biopolymers, 20, 2351, 1981.
12. Duguid, J., Bloomfield, V. A., Benevides, J., and Thomas, G. J., Jr., Biophys. J., 65, 1916, 1993.
13. Thomas, G. J., Jr., Benevides, J. M., Duguid, J., and Bloomfield, V. A., in T. Theophanides et al. (eds.), *Fifth International Conference on the Spectroscopy of Biological Molecules*, Kluwer Academic Publishers, Dordrecht, p. 39 (1993).
14. Guschlbauer, W., and Courtois, Y., FEBS (Fed. Eur. Biochem. Soc.) Lett., 1, 183, 1968.
15. Muntean, C. M., Puppels, G. J., Greve, J., Segers-Nolten, G. M. J., Otto, C., in 8th European Conference on the Spectroscopy of Biological Molecules Proc., (29 August - 2 September 1999, Enschede, the Netherlands), J. Greve, G. J. Puppels, C. Otto Eds., Kluwer Academic Publishers, Dordrecht (1999), the Netherlands, p. 221.

Acknowledgements

This work was supported in part by a CEC grant, under contract nr. ERB-CIPA-CT-92-2223. EC financial support and research experience gained at the University of Twente, Enschede, the Netherlands, are greatfully acknowledged by one of us (C.M.M.).

STUDIA UNIVERSITATIS BABEŞ-BOLYAI, PHYSICA, XLV, 2, 2000

VIBRATIONAL ANALYSIS AND SPECTRA OF N-HYDROXYUREA AND ITS DEUTERATED HOMOLOGUE– AN HIV AND ONCOSTATIC DRUG

S. D. SILAGHI[1], O. COZAR[1], A. HERNANZ[2], I. BRATU[3]

ABSTRACT. The FT-IR and FT-Raman spectra of the solid N-Hydroxyurea and its partially deuterated homologue are given. The assignments of the vibrational modes are done in comparison with those of the similar molecular structures such as urea (H_2NCONH_2) and hydroxamic (R–CO–NHOH) acids.
The 1Za conformer of the amidic tautomer of N-HU molecule prevails in the obtained spectra. This suggests the presence of intramolecular H-bonding between the O atom of the carbonyl and the H atom of the hydroxyl groups.

Introduction

Hydroxyurea or aminoformohydroxamic acid (HU) as a representative of the hydroxamic acids has several interesting properties as a specific inhibitor of the urea activity for patients with chronic leukemia, a complement to radiation treatment in a number of diseases, a selective agent against the episome responsible for drug resistance, stimulators for fetal hemoglobin synthesis reducing the sickle cell anemia episomes etc. [1]. It plays an important role of compact packaging of the high molecular weight DNA in prokaryotic cells, and its specific function as well as the structure have drawn attention not only from biochemical but also from physico-chemical points of view [2].

In HIV disease HU appears to work by inhibiting a cellular enzyme called ribonucleotide reductose, which reduces the amount of DNA building blocks which are necessary for cell replication but impact of HU on HIV remains still undetermined [3].

In this paper we present an analysis of the vibrational spectra of the solid N-hydroxyurea and its partially deuterated form. The assignments of

[1] "Babes-Bolyai" University, Faculty of Physics, Kogalniceanu 1, Cluj-Napoca, Romania
[2] UNED, Depto. CCyTT, Fisicoquimicas, Senda del Rey 9, Madrid, Spain
[3] National Institute for R&D of Isotopic and Molecular Technologies, P.O. Box 700, Cluj-Napoca 5, Romania

the vibrational modes are done in comparison with those of the similar molecular structures such as urea (H_2NCONH_2) and hydroxamic acids (R-CO-NHOH). The vibrational wavenumbers of the solid N-Hydroxyurea reported previously [4,5] were used.

N-Hydroxyurea ($N_2NCONHOH$) can exist in both keto and iminol tautomeric forms [Fig.1]. In both forms the hydroxyl group can be present in either trans or cis orientation, denoted by E and Z respectively [Fig.2]. The molecular structure of N-Hydroxyurea was investigated by La Manna and Barone performing "ab initio" calculations on the tautomers and conformers of this molecule [6].

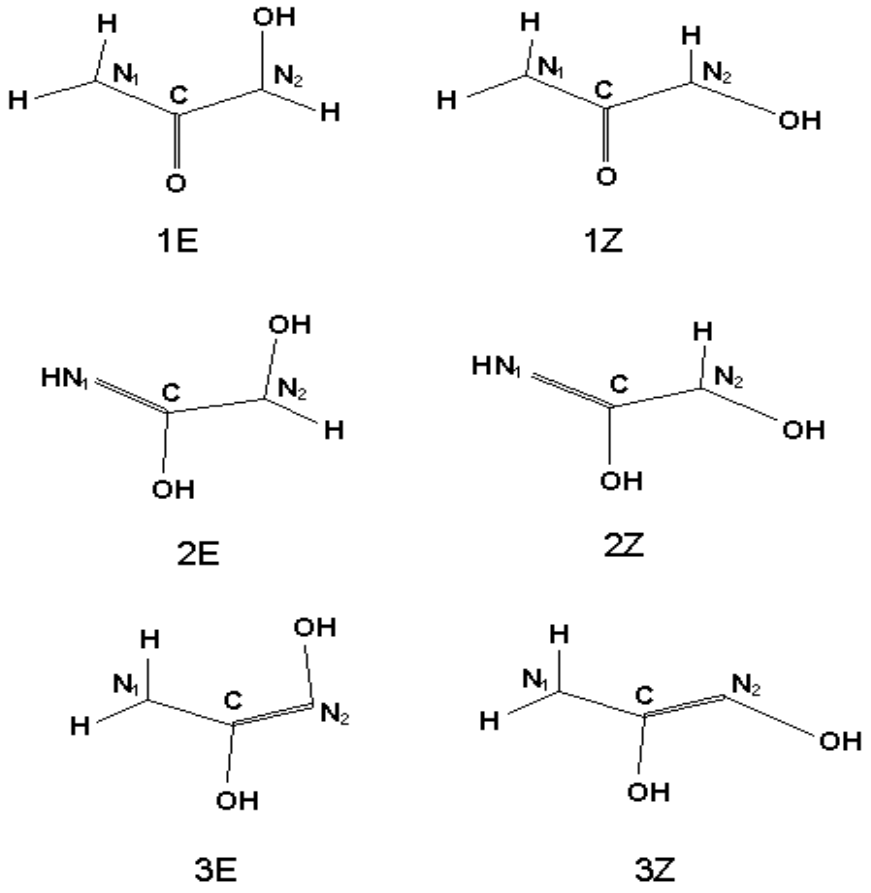

Fig. 1. The tautomeric forms of N–Hydroxyurea in their E and Z conformations

Also the X-Ray diffraction data showed that all atoms of the N-HU molecule lie in the same plane [7,8] except the hydrogen atom of the OH group.

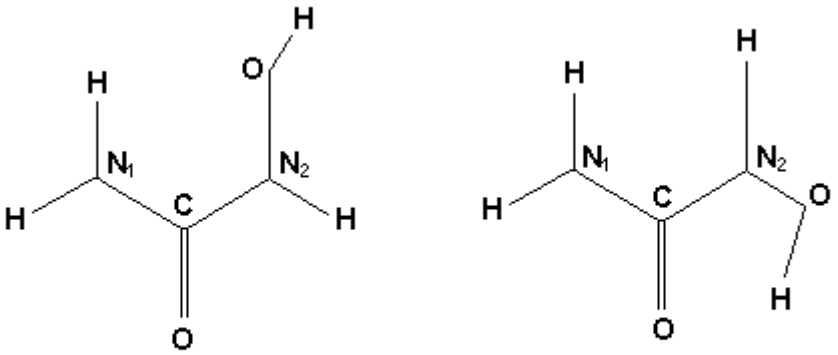

Fig. 2. The 1Ea and 1Za conformers of the amidic tautomer of N–Hydroxyurea

Materials and Methods

The FT-IR and FT-Raman spectra of the solid N-HU and its partially deuterated form were recorded with a BOMEM DA_3/DA_8 FT-IR /FT-Raman spectrometer. The mid region spectrum was recorded using a Globar source, a MCT detector (77K) and a KBr beam splitter. The resolution was S = 2 cm^{-1} (Hamming apodizing function and 500 interferograms were coadded. The FT-Raman spectra were recorded in the 3000 – 50 cm^{-1} region, using a Nd^{3+} - YAG laser (λ = 1064 nm, P=1W), an InGaAs detector (77 K) and a quartz beam splitter. The resolution was S = 4 cm^{-1} (Hamming apodizing function) and 500 interferograms were coadded. All FT-IR and FT-Raman spectra were recorded at room temperature.

The deuteration samples helped us to propose an adequate assignment of vibrational modes. N-HU was partially (50%) deuterated by solving the compound in heavy water (99,5 at % D) at high temperature (80 ^{0}C) and crystallizing out the deuterated product by cooling (10-15^{0}C).

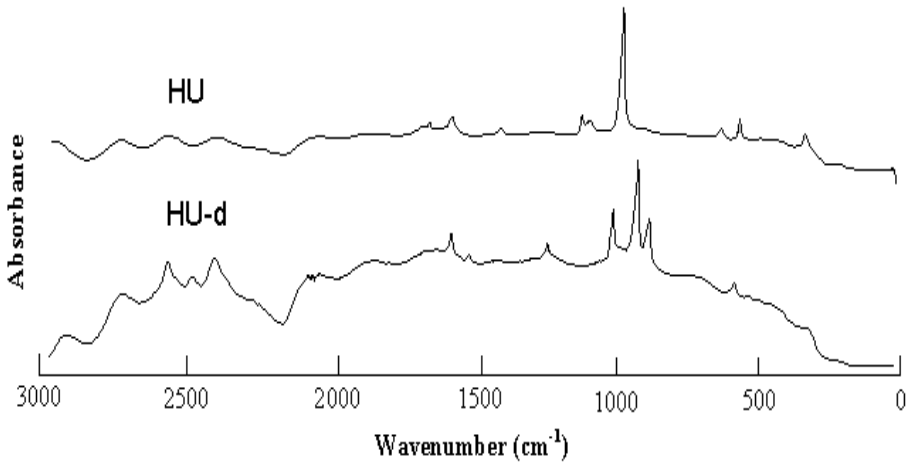

Fig. 3. The FT-IR spectra of N–Hydroxyurea and its deuterated form

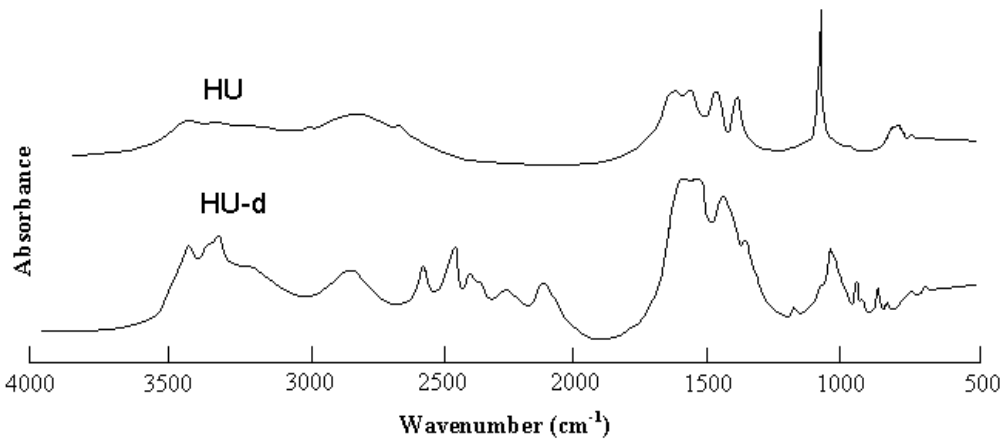

Fig. 4. The FT-Raman spectra of N–Hydroxyurea and its deuterated form

Results and Discussion

N-Hydroxyurea molecule ($H_2NCONHOH$) belongs to the C_1 point group symmetry and has 21 normal vibrations, all of these being active in infrared and Raman.

a) 3500-2000 cm^{-1} Spectral Region

In this region four absorption bands are expected: the antisymmetrical and symmetrical NH_2 – stretching vibrations and the NH and OH stretching vibrations. Sarukhanov et al. [4] have observed these four bands at υ_a (NH_2) = 3430 cm^{-1}, υ(NH) = 3325 cm^{-1}, υ_s (NH_2) = 3200 cm^{-1} and υ (OH) = 2830 cm^{-1}, respectively. Davies and Spiers [5] have observed two clear peaks at 3413 cm^{-1} and 3306 cm^{-1} superimposed upon a broad absorption extended from about 3400 cm^{-1} to 2400 cm^{-1} with a shoulder near 3180 cm^{-1} and a distinct maximum at 2805 cm^{-1}.

The assignment of the O-H and N-H stretching bands is rather difficult. The OH and NH groups in crystalline N-HU are joined by strong hydrogen bonds, so that the corresponding absorption bands in the infrared spectra are very broad, with poorly defined maxima.

We assigned these four absorption bands from 3440, 3320, 3200 and 2808 cm^{-1}, to the stretching vibrations $\upsilon_{as}(NH_2)$, υ(NH), $\upsilon_s(NH_2)$ and υ(OH), respectively. The mean of the antisymmetrical and symmetrical NH_2 stretching vibrations, 3320 cm^{-1}, is estimated as the position at which the uncoupled υ(NH) vibration of component bands should occurs. Thus the absorption at 3320 cm^{-1} in solid N-HU is assigned to this mode.

The very low frequency υ(OH) = 2808 cm^{-1} is characteristic for hydroxamic acids which seems to be due to the intramolecular hydrogen bonding [10]. The difference between the absorption frequency υ(OH) =2830 cm^{-1} observed by Sarukhanov et al. [4] and our value υ(OH) = 2808 cm^{-1} indicates that the 1Za conformer of the amidic tautomer of N-HU molecule prevails in our spectra in comparison with the 1Ea conformers reported by Sarukhanov [4]. There is a linear relationship between OH…O distance and the wavenumber υ(OH). X-Ray diffraction gives the value of r(OH…O) = 2,646 Å for the 1Ea conformer [9].

After deuteration these four bands shift to 2579, 2468, 2410 and 2137 cm^{-1}, respectively. The average ratios : [$\upsilon_a(NH_2)$ / $\upsilon_a(ND_2)$] ~ 1,33 ; [(υ (NH) / υ (ND)] ~ 1,34; [$\upsilon_s(NH_2)$ / $\upsilon_s(ND_2)$] ~ 1,32; [υ (OH) / υ (OD)] = 1,31 indicate the pure character of these vibrations.

b) 1700 – 1400 cm^{-1} Spectral Region

The bands which appear in this region correspond to the vibrational modes: υ(C = O), δ (NH_2), υ_a(NCN), δ (NH) and δ (OH), which are mainly due to the in-plane vibrations. Davies and Spiers [5] have observed four strong absorption peaks at 1631 cm^{-1} – υ (CO), 1590 cm^{-1} – δ (NH_2), 1488 cm^{-1} - υ (CN) and 1404 cm^{-1} – δ (OH). Sarukhanov et al. [4] have assigned also similar values such as: 1648, 1595, 1498 and 1413 cm^{-1}, to these vibrational modes.

In our infrared spectrum we observed four absorptions bands at υ(CO) = 1630 cm^{-1}, δ (NH_2) = 1580 cm^{-1}, υ_a(NCN) = 1487 cm^{-1}, δ (NH) = 1410 cm^{-1} and a shoulder at 1415 cm^{-1}, which is probably due to the δ (OH) vibration. Similar values have been found in the Raman spectrum.

The effect of intramolecular H-bonding can be seen in the case of the vibrational mode of carbonyl group, υ (CO), which appears at 1630 cm^{-1} in the HU molecule. This frequency shifts at 1597 cm^{-1} in the urea molecule because of the formation of intermolecular H bonding [11].

Among the absorptions at 1630 cm^{-1} and 1580 cm^{-1} the former is undoubtedly υ (C=O) or the amide I band. By deuteration this band becomes a doublet which shifts to 1647 – 1600 cm^{-1} and it is characteristic for the derivatives of the hydroxamic acids, υ (C=O) = 1650 cm^{-1} [10].

c) 1200 – 300 cm^{-1} Spectral Region

A very strong absorption band appears at 1110 cm^{-1}, which is assigned by us to the rocking ρ (NH_2) frequency. In the Raman spectrum this band shifts to 1113 cm $^{-1.}$ Sarukhanov et al. [4] have assigned this absorption at 1115 cm^{-1} and Davies and Spiers [5] at 1109 cm^{-1}.

The next absorption is a very weak band at 975 cm^{-1} in the infrared spectrum and very strong band in the Raman spectrum. By deuteration this band shifts to 932 cm^{-1} and it is assigned as to be a symmetrical NCN stretching vibration. In urea molecule υ_s (NCN) is observed at 1003 cm^{-1} which shifts to 890 cm^{-1} by deuteration [11]. Sarukhanov et al [4] and Davies and Spiers [5] also observe the absorption band at 975 cm-1 in HU molecule.

It is very difficult to assign the vibrational modes in the 815 – 700 cm^{-1} range of the infrared spectrum. By deuteration this region is not changed. This fact suggested that in this region there are the absorption bands due to the skeletal δ (OCN) deformation. In the Raman spectrum we observed three weak absorptions at 625, 564 and 330 cm^{-1}, which may be, assigned to τ(NH_2), γ(CO) and ω(NH_2) vibrations respectively in agreement with the literature data [12,13].

Conclusions

The FT-IR and FT-Raman spectra of the solid N-Hydroxyurea and its deuterated form were recorded and the assignment of the vibrational modes were done according to the literature data.

In our spectra the 1Za conformer of the amidic tautomer of N – HU molecule is prevailing, this suggesting the formation of intramolecular H – bonding between the O atom of carbonyl and the H atom of the hydroxyl group.

More information about the vibrational assignment will be obtained by using a totally deuterated N – HU and ^{15}N – HU species homologues.

REFERENCES

1. Jabalameli, N.U. Zhanpeisov, A. Wowek, R.H. Sullivan, J. Leszczynski, *J. Phys. Chem. A*, 101, 3619 (1997).
2. S. Takoshima, K. Yamooka, *Biophysical Chemistry*, 80, 153 (1999)
3. R. Gamundi, "Hu's impact on HIV remains undeterminated", www.Infind.com.
4. M.A. Sarukhanov, S.A. Slivko, Yu.Ya. Kharitonov, *Russ. Journ. of Inorg. Chem.*, 26(5), 1228 (1981).
5. M. Davies, N.A. Spiers, *Spectrochim. Acta*, 487 (1959).
6. G. La Manna, G. Barone, *Internat. Journ. of Quantum Chem.*, 57, 971 (1996).
7. I.K. Larsen, B. Jerslev, *Acta Chem. Scand.*, 20, 983 (1966).
8. H.M. Bernan, S.M. Kim, *Acta Cryst.*, 23, 180 (1967).
9. N. Armagon, J.P.G. Richards, A.A. Uraz, *Acta Cryst.*, B32, 1042 (1976).
10. D. Hadzi, D. Prevorsek, *Spectrochim. Acta*, 10, 38 (1957).
11. R. Keuleers, H.O. Desseyn, B. Rousseau, C. Van Alsenoy, *J. Phys. Chem. A*, 103, 4621 (1999).
12. G. Socrates "Infrared Characteristic Group Frequencies", Edited by John Wiley & Sons, Ltd., 1980.
13. Noel P.G. Roeges, "A Guide to the Complete Interpretation of Infrared Spectra of Organic Structures", Edited by John Wiley & Sons, Ltd., 1994.

STUDIA UNIVERSITATIS BABEŞ-BOLYAI, PHYSICA, XLV, 2, 2000

RADIOACTIVATION AND DURABILITY OF Y_2O_3-Na_2O-P_2O_5 GLASSES

V. SIMON[1], D. CĂCAINĂ[1], D. ENIU[2], L. DĂRĂBAN[1], S. SIMON[1]

***ABSTRACT*.** Samples of $xY_2O_3(100-x)[\ 3P_2O_5 \cdot Na_2O]$ glass system ($0 \leq x \leq 20$ mol %) were activated by thermal neutron irradiation. The radionuclides occurrence was identified by gamma and beta spectroscopic analyses. The dissolution of activated samples was tested in static regime in desalinized water, physiological serum and chlorine acid (pH = 1.5) solution.

Introduction

Radiotherapy glasses proved to be well suited for radiotherapeutic use in humans. They provide a new and unique method of irradiating diseased internal organs with beta and gamma radiation in amounts which exceed those that can be delivered by other means external beam radiation, due to the major limitation of the maximum dose which can be safely delivered is constrained by the need to protect surrounding healthy tissues [1, 2].

For use as in vivo radiation delivery vehicles, radiotherapy glasses should be biocompatible and nontoxic to the body, chemically insoluble during the time the glass is radioactive and have high chemical purity in order to avoid the activation of unwanted radioisotopes. On the other hand it would be desirable the dissolution and elimination of the radiotherapy glasses from the body after their deactivation. In addition to the in situ irradiation the radiotherapy glasses have the advantage to be nonradiative during the manufacturing process up to the last step consisting in neutron activation of the desired isotopes.

The aim of this study is to induce radioisotopes in the investigated Y_2O_3-Na_2O-P_2O_5 glasses by neutron irradiation, to evidence the activated radioisotopes and to estimate the leaching resistance of the irradiated samples in different solvents simulating biological media.

[1] Babes-Bolyai University, Faculty of Physics, 3400 Cluj-Napoca, Romania
[2] University of Medicine and Pharmacy, Faculty of Pharmacy, 3400 Cluj-Napoca, Romania

Experimental

The investigated $xY_2O_3(100-x)[3P_2O_5 \cdot Na_2O]$ samples were obtained in the composition range $0 \leq x \leq 20$ mol % by melting of Y_2O_3, $(NH_4)_2HPO_4$ and $Na_2CO_3 \cdot 10H_2O$ chemicals of reagent grade purity. The homogenized mixtures were melted at 1000°C for 10 minutes in sintered corundum crucibles in an electric furnace and then the melts were quickly undercooled at room temperature by pouring onto stainless steal plates.

The glass samples were irradiated for 10 days using an activation equipment with two isotopic sources ^{241}Am-^{9}Be of 5 Ci and ^{239}Pu-^{9}Be of 15 Ci providing in the 4π solid angle a total flux of $6 \cdot 10^7$ neutrons/s. The radioisotopes induced by neutron activation were identified by means of a high resolution Ge-Li gamma spectrometer KOVO-RSC. Due to the fact that both ^{90}Y and ^{32}P are preponderantly beta emitters we also used the beta spectrometry based on Fermi-Curie diagrams [3-5] using a 5 mm thick plastic scintillation detector coupled with a ND-206 type photomultiplier tube. All samples were inspected in the same conditions (acquisition time 60 minutes and gain factor 50).The dissolution stability was followed in static regime by immersion of samples in different solvents simulating biological media (desalinized water, physiological serum and chlorine acid solution with pH = 1.5) by measuring the weight of samples maintained in the mentioned solutions at 42°C for different times up to 100 hours. The ratios SA/V between the samples surface area (SA) and solvent volume (V) was about 20 m^{-1}, according to the usual standards of leaching conditions for the incipient stages in testing the dissolution resistance of glasses containing radionuclides [6-9]. The results are expressed in terms of normalized mass loss. The samples mass was determined by using a digital balance sensitive to 0.1mg.

Results and discussion

The elements of the investigated glass system which can be activated by neutron irradiation are Y, P and Na. The radioisotope ^{90}Y ($T_{1/2}$ = 64 hours) emits beta radiations of 0.51 and 2.26 MeV with relative abundance of 0.026 % and 99.98 % respectively and gamma radiation of 1.77 MeV with 100 % abundance. ^{32}P ($T_{1/2}$ = 14.5 days) emits beta radiations of 1.71 MeV with relative abundance of 0.026 % and 99.98 % respectively and gamma radiation of 1.77 MeV with 100 % abundance. ^{24}Na ($T_{1/2}$ = 15 hours) emits beta radiations of 0.34, 1.40 and 4.16 MeV with a relative abundance of 0.05, 99.957 and $3 \cdot 10^{-3}$ % respectively, and gamma radiation of 1.37, 2.75 and 3.815 MeV with relative abundance of 100, near to 100 and 0.05 % respectively [10].

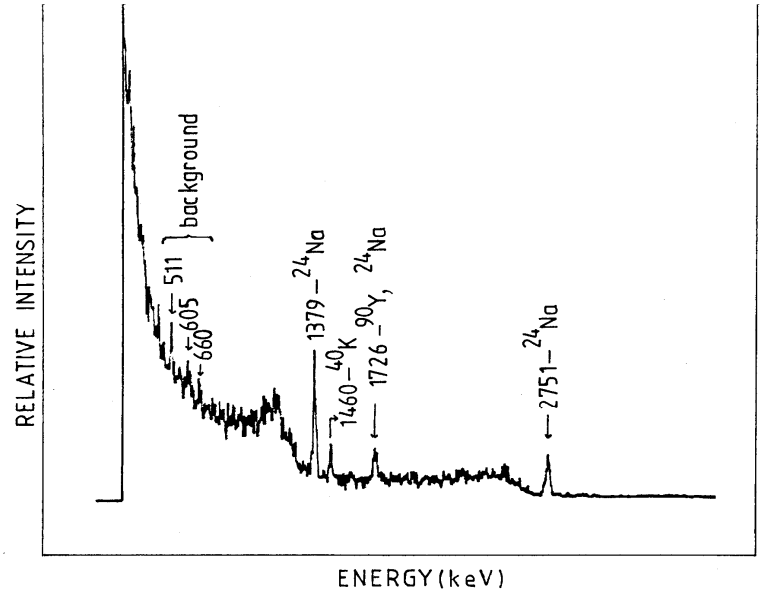

Fig. 1. Gamma spectrum recorded from $20Y_2O_3 \cdot 80[3P_2O_5 \cdot Na_2O]$ neutron activated sample.

For the glasses aimed to be used in radiotherapy it is very important to be insoluble during the time the glass is radioactive and to contain no impurities which could be also activated by the neutron activation of the samples. The radionuclides identified by gamma spectroscopy analyses are summarized in Table 1. For illustration is given in Figure 1 the gamma spectrum of the activated sample containing 20 mol % Y_2O_3. The peak recorded at 1460 keV is assigned to ^{40}K radioisotope arising from the laboratory background. The activation of ^{32}P was evidenced as expected only by beta spectroscopy. The beta spectrometer was calibrated with a ^{90}Y-^{90}Sr laboratory pure source (Fig. 2). The end point of ^{90}Y beta spectrum was the reference for all investigated samples with $x \neq 0$.

In the investigated glass samples were not evidenced other radioisotopes neither by gamma nor by beta spectrometry analyses.

The dissolution static test carried out at 42°C in solutions simulating biological media prove chemical durability only during the first 10 hours and then is observed a fast sample dissolution as shown in Figure 3. After 100 hours of immersion in chlorine acid solution the sample containing 20 mol % Y_2O_3 weights 67 % less than initially. The structural stability of the radioisotopes in glass matrices is correlated with their local symmetry [11]. The decrease of dissolution resistance is also due to the presence of Na_2O in the glass matrix, having in view that the alkali ions diminish the network consistency [12]. Figure 4 illustrates the composition dependence of the relative mass loss determined by leaching in chlorine acid solution.

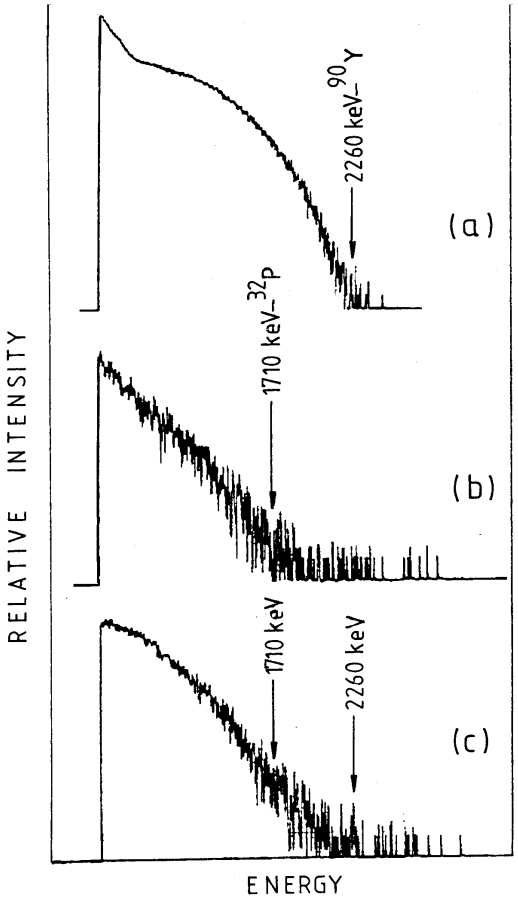

Fig. 2. Beta spectra recorded from: (a) the ^{90}Y-^{90}Sr laboratory pure source, (b) the glass matrix without yttrium (x = 0) and (c) the sample containing 5 mol % Y_2O_3.

The results of chemical durability tests reported for radiotherapy glasses [1, 13–15] indicate a high stability under different leaching conditions, for much longer time than the period the samples are radioactive. Having in view the high dissolution of the investigated samples starting after 10 hours immersion in simulating biological media (Fig. 3) and the half life times of the neutron activated isotopes it is evident that they are not suited in this compopsition range for radiotherapeutic use, being imposed an additional nonradiative component to stabilize the glass matrix for the period the samples are radioactive.

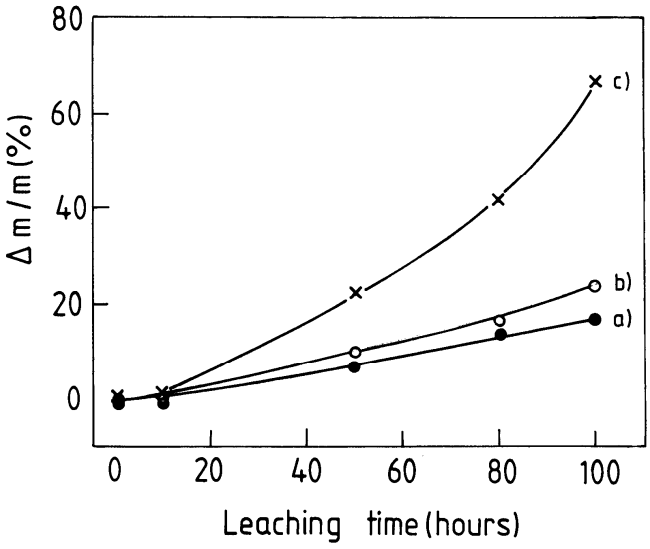

Fig. 3. Relative mass loss of $20Y_2O_3 \cdot 80[3P_2O_5 \cdot Na_2O]$ activated sample leached in: (a) decationised water, (b) physiological serum and (c) chlorine acid (pH=1.5) solution.

Table 1.

The radionuclides identified by gamma spectroscopy analyses in $xY_2O_3(100-x)[3P_2O_5 \cdot Na_2O]$ samples activated by thermal neutrons.

x	Energy (KeV)	Radionuclid	Peak area (pulses/60 minutes)
0	1370	^{24}Na	74.5
	1748	^{90}Y, ^{24}Na*	42
	2758	^{24}Na	0.5
5	1376	^{24}Na	165
	1733	^{90}Y, ^{24}Na*	56.7
	2751	^{24}Na	20
10	1368	^{24}Na	261.6
	1730	^{90}Y, ^{24}Na*	90
	2769	^{24}Na	21
20	1379	^{24}Na	392.7
	1726	^{90}Y, ^{24}Na*	133.7
	2571	^{24}Na	16

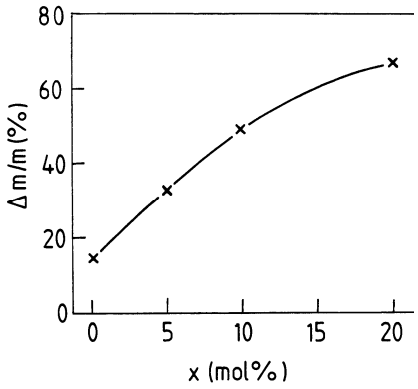

Fig. 4. Relative mass loss of $xY_2O_3(100-x)[3P_2O_5 \cdot Na_2O]$ activated samples leached for 100 hours in chlorine acid (pH = 1.5) solution versus Y_2O_3 content.

Conclusions

The thermal neutron activation applied for 10 days in a $6 \cdot 10^7$ neutron/s flux induces in the $xY_2O_3(100-x)[3P_2O_5 \cdot Na_2O]$ glass samples ^{90}Y, ^{32}P and ^{24}Na radioisotopes as evidenced by gamma and beta spectroscopic analyses. The chemical durability of the activated samples in leaching solutions simulating biological media decreases in all cases with Y_2O_3 content even in the first stage of the experiment, excepting the first 10 hours. The highest dissolution (67 %) in static regime was obtained in chlorine acid solution after an immersion time of 100 hours. These results indicate the necessity to introduce in the $3P_2O_5 \cdot Na_2O$ glass matrix an additional nonradiative component to rise the dissolution resistance during the time the glassees are radioactive in order to obtain a glass system proper for internal radiotherapy.

REFERENCE

1. D.E. Day, Th.E. Day, An Introduction to Bioceramics, eds. L.L. Hench & J. Wilson, World Scientific, 1991, p.305.
2. F.A. Shepherd, L.E. Rotstein, S. Houle, T.K. Yip, K. Paul, K.W. Suderman, Cancer, 70, 2250 (1992).
3. F.K. Wohn, J. R. Clifford, G. H. Carlson, W. L. Tabert, Jr., Nucl. Instr. Meth., 101, 343 (1972).
4. N. Tsoulfanidis, B. W. Wehring and M. E. Wyman, Nucl. Instr. Meth., 73, 98 (1969).
5. P. C. Rogers, G. E. Gordon, Nucl. Instr. Meth., 37, 259 (1965).
6. H.D. Schreiber, G.B. Balazs, T.N. Solberg, Phys. Chem. Glasses, 26, 35 (1985).
7. W.L. Ebert, J.J. Maser, Mater. Res. Soc. Symp. Proc, Mater. Res. Soc., 333, 1994.
8. L.A. Chick, R.O. Lokhin, D.M. Strahan, W.M. Bowen, J. Am. Ceram. Soc., 69, 114 (1986).
9. V. Simon, I.Ardelean, O.Cozar, S.Simon, J. Nucl. Mater., 230, 306 (1996).
10. P. Sandru, A.Topa, Radionuclizii, Ed. Academiei, Bucuresti, 1968.
11. S. Simon, I. Ardelean, D. Eniu, V.Simon, Studia, Physica, XLII, 1, 3 (1997).
12. H. Li, M. Tomozawa, J. Non-Cryst. Solids, 195, 188 (1996).
13. O.H. Andersson, K.H. Karlsson, J. Non-Cryst. Solids, 129, 145 (1991).
14. H.M. Kim, F. Miyaji, T. Kokubo, J. Am. Ceram. Soc. 78, 9, 2405 (1995).
15. M. Kawashita, T. Yao, F. Miyaji, T. Kokubo, G.H. Takaoka, I. Yamada, Radiat. Phys. Chem., 46, 2, 269 (1995).

STUDIA UNIVERSITATIS BABEŞ-BOLYAI, PHYSICA, XLV, 2, 2000

NMR STUDY OF WATER BEHAVIOR INSIDE THE AN69 POLYMERIC MEMBRANE

ALINA BUDA[1], M.TODICA[1], O.COZAR[1]

***ABSTRACT*.** Study of water behavior inside the pores of AN69 polymeric membrane was made using NMR technique. An important change of the shape of the relaxation curves is observed around 265K, which indicates a change of the behavior of the water molecules inside the pores.

INTRODUCTION

In the last years, the behavior of liquid molecules located inside the polymeric membranes is a very important area of study because the special applications of polymeric membranes. Various applications of membranes like catalysis, oil recovery or membrane separation require the understanding of the properties of absorbed liquid molecules, [1, 2].

It is widely accepted that the behaviour of the liquid molecules inside the polymeric pores is different from those of free liquid molecules because of the interaction with the walls of pores. Generally, in these situations, the freezing point is depressed, [3, 4].

There are many techniques used to investigate this behaviour but NMR spectroscopy remains one of the most important non-invasive methods, [5, 6, 7, 8].

The aim of our study is the investigation of the water molecules behaviour inside the pores of the AN69 polymeric membrane, based on the observation of the proton spin-spin relaxation.

EXPERIMENTAL

The AN69 polymeric membrane is a copolymer of acrylonitrile and of sodium methyl solvate and it was supplied by Hospal Industry, Lyon, France. The shape of our samples is that of hollow transparent fibres with an external diameter of 294μm, an inner diameter of 210μm and a thickness of 50μm.

The polymeric fibers were introduced in an inert glass tub and submitted to a flow of water during 5 minutes. During this time the liquid penetrated through the membrane structure. Then, the sample was

[1] "Babeş-Bolyai" University, Faculty of Physics, RO-3400, Cluj-Napoca, Romania

submitted to a drying process in order to eliminate the water content existing outside the membrane pores.

Finally, the fibers were sceled in NMR tubes in order to prevent the water evaporation.

The NMR proton spin-spin relaxation data were recorded in the temperature range 250-300K using a Bruker NMR spectrometer working at 60MHz. The diffusion effect on the relaxation process is eliminated using the Carr-Purcell sequence.

We used two kinds of sample: AN69 membrane in dried state and AN69 membrane containing water molecules inside the pores.

RESULTS AND DISCUSSION

The NMR relaxation curves of AN69 membrane in dried state and of the membrane containing water inside the pores, recorded for many temperatures, are presented in Figure 1.

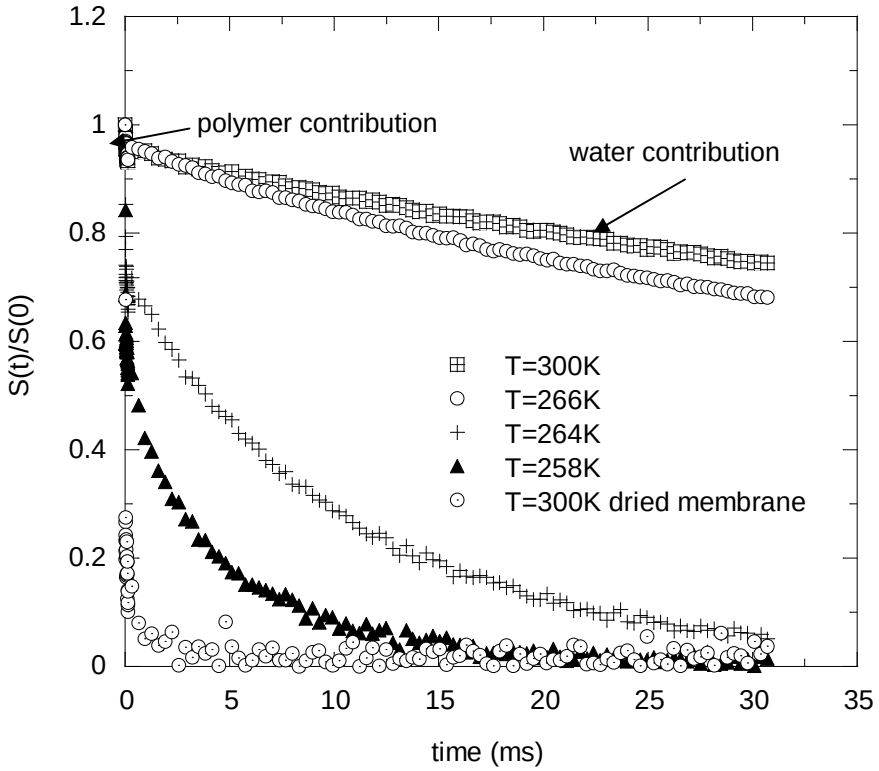

Fig. 1. NMR relaxation curves of AN69 polymeric membrane in dried state and with water content, at different temperatures

Some aspects can be relevated by observing these relaxation curves. First, it can easily see that each relaxation curve contains two distinct parts: a fast decay of the transversal magnetisation located in the 0-1 ms time range of the relaxation process followed by a slow process extended over a large time domain of the order of many tens milliseconds.

We can also observe an evolution with the temperature of the shape of the curves of the AN69 membrane containing water, with an important change of the shape of these relaxation curves around the temperature of 265K.

Concerning to the first aspect, we must take into account the fact that the NMR signal is given also by the protons of the membrane and by the water protons. The spin-spin relaxation of the protons of the polymeric membrane is a fast process extended in the time range 0-1 ms so that these protons will contribute to the total NMR signal only at the beginning of the relaxation of the entire system, [9]. On the other hand, the spin-spin relaxation of the water protons is a very slow process compared with the relaxation of the polymeric protons, being extended over a large time range of many tens ms. The contribution of the water protons to the total magnetisation in the 0-1 ms range can be regarded as a constant amount. In these conditions, it is clearly that the decay of the NMR signal in this time domain is due only to the polymeric protons. After 1 millisecond the transversal magnetisation of the polymeric protons is completely relaxed so that the slowly part of the relaxation process is determined only by the water protons. From this partition of the relaxation curves we can study separately the relaxation behaviour of the two kinds of protons.

Firstly, we analysed the fast decay of each relaxation curves. From Figure 2 we can easily see that, in the time domain 0-1ms, the shape of the relaxation curves of the AN69/water system is practically the same for different temperatures.

No dramatically change of the shape of these curves were observed around 265K and we can also see that there are not a great difference between the shape of the relaxation curves corresponding to the dried membrane and the membrane containing water.

This behavior yields to two conclusions. The first one is that the rapid decay of the relaxation curves is associated with the relaxation of the polymeric protons. The second one is that the presence of the water molecules have not important influence on the relaxation process of the polymeric protons. As a consequence, we can see only a weak variation of the relaxation curves with the temperature, in the time domain 0-1 ms and a similarity between the relaxation curves of the dried membrane and the membrane containing water.

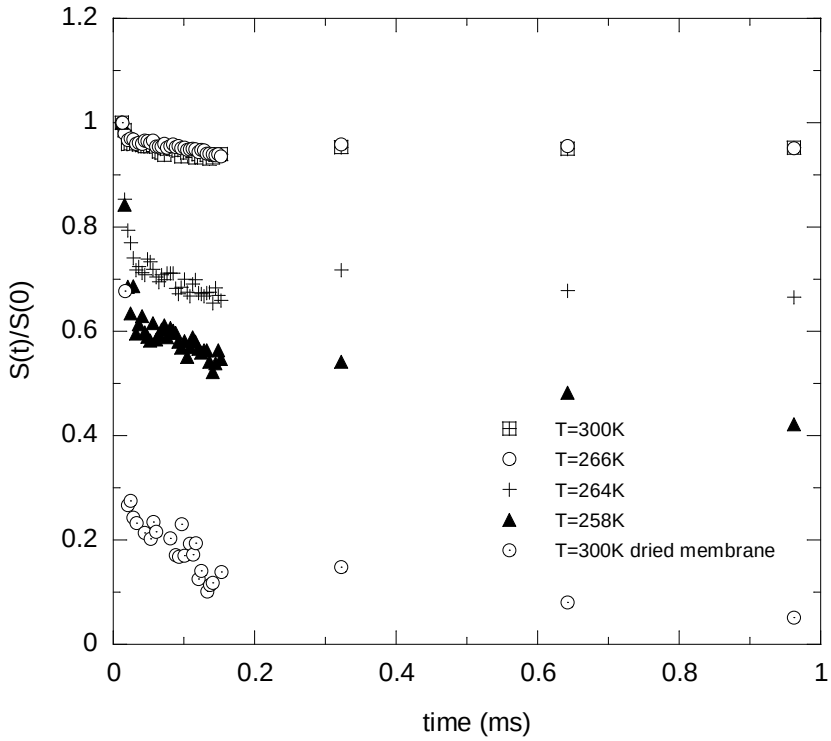

Fig. 2. Evolution of the fast decay of the relaxation signals with the temperature

Regarding to the slow decay of the relaxation curves, as we discussed above, we can assume that the transversal magnetisation of the polymeric protons is completely relaxed after 1 ms and the NMR signal is given only by the water protons. If this assumption is true, we must observe a change of the behaviour of the relaxation curves with the temperature, especially in the vicinity of the freezing point of water. Indeed, an important change of the shape of the relaxation curves is observed around the temperature of 265K, Figure 1. This temperature is different from the normal freezing temperature, 273K, of the water in normal state. The decay of the relaxation curves is slow above 265K and fast under this temperature. This change of shape of the relaxation curves clearly indicates a change of the behaviour of the water molecules inside the pores of polymeric membrane. We can regard this behaviour change like a transition process of the water molecules. When the water molecules are located inside the pores of the polymeric membrane, interactions can occur between the water molecules and the walls of the pores, [10]. In these

conditions, the water molecules are not in the free state (like in normal conditions) which can explain the modification of the transition temperature.

Much clear indications concerning the existence of the transition process must be done comparing the relaxation time of the transversal magnetisation of the protons above and under the temperature of 265K.

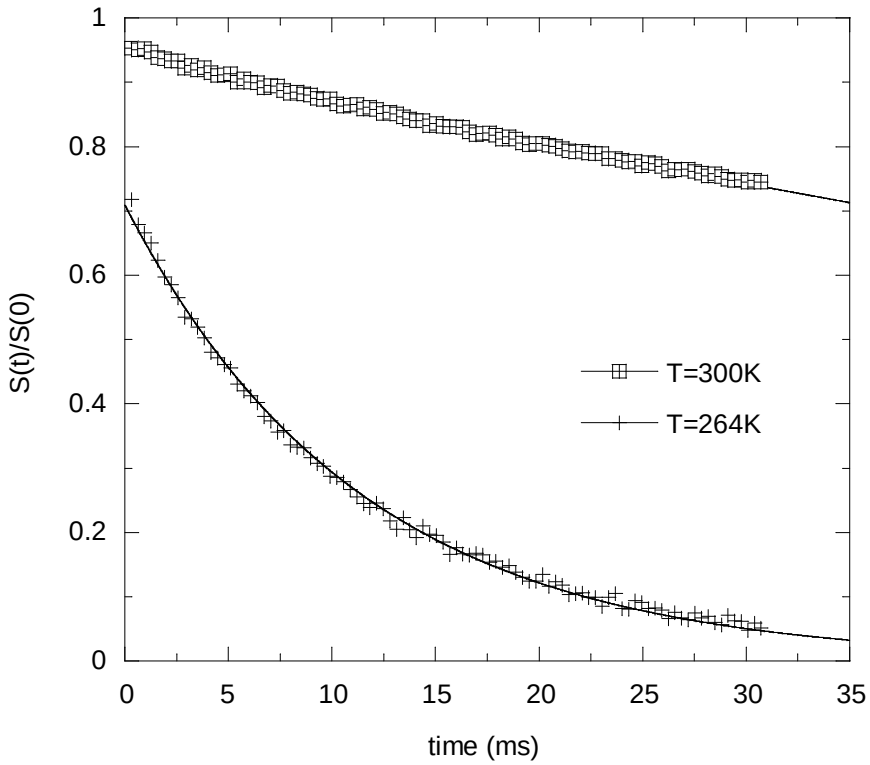

Fig. 3. Single exponential decay of the water protons transversal relaxation signal

Generally, the relaxation of the transversal magnetization of the simple liquids is described by a single exponential function. Supposing that the slow decay of each relaxation curve is due only to the protons of the water molecules, as we discussed previously, we tested each normalized curve using a single exponential function of the form:

$$\frac{S(t)}{S(0)} = \exp\left(-\frac{t}{T_2}\right)$$

where S(t) is the amplitude of the recorded signal at the moment t, S(0) is the amplitude of the recorded signal at the beginning of the relaxation and T_2 is the spin-spin relaxation time of the transversal magnetization. We constated that all the curves can be described by this function, with different values of T_2, Figure 3. From the best fit of each curve we calculated the values of the relaxation time T_2 for each temperature, which are represented in Figure 4. The temperature dependence of the relaxation time T_2 clearly indicates the existence of the transition process around the temperature of 265K. Indeed, the relaxation time increases with increasing the temperature, but its value is of order of few milliseconds below the temperature 265K and of order of few tens milliseconds above 265K. These values of the relaxation time suggest great differences between the state of water molecules above and below 265K. Above this temperature, we can regard the water molecules as in free state and below this temperature the water molecules as in freezing state.

However, an important aspect reveals from the analyze of the value of the relaxation times.

The relaxation times of our system for temperatures greater than 265K are smaller than those corresponding to the normal water at the same temperature. For example, at room temperature, the obtained relaxation time for normal water is 0.26 seconds comparing with the value of 0.125 seconds of our system. For temperatures less than 265K, at 262K for example the obtained values 7.93ms are bigger than that measured for ice which is 13.2μs. The small value of T_2 for temperatures higher than 265K can be explained if we suppose that the water molecules located in the polymeric pores are not completely free, like in the normal water. As a consequence, the relaxation time is shorter.

The behaviour under 265K can be explain if we suppose that a fraction of the total number of water molecules exists in unfreezing state, [10]. These molecules must have great interactions with the polymeric walls, that mean that these molecules are located in small pores, [11]. For these molecules, the freezing point is depressed and the relaxation time is different from those of the normal water at the same temperature. Taking into account the modification of the freezing point of water molecules located inside the pores of the membranes, it is possible to estimate the mean size of these pores. To do this, we will suppose that the water molecules are located inside an ideal pore of spherical shape and we will consider the liquid-solid transition.

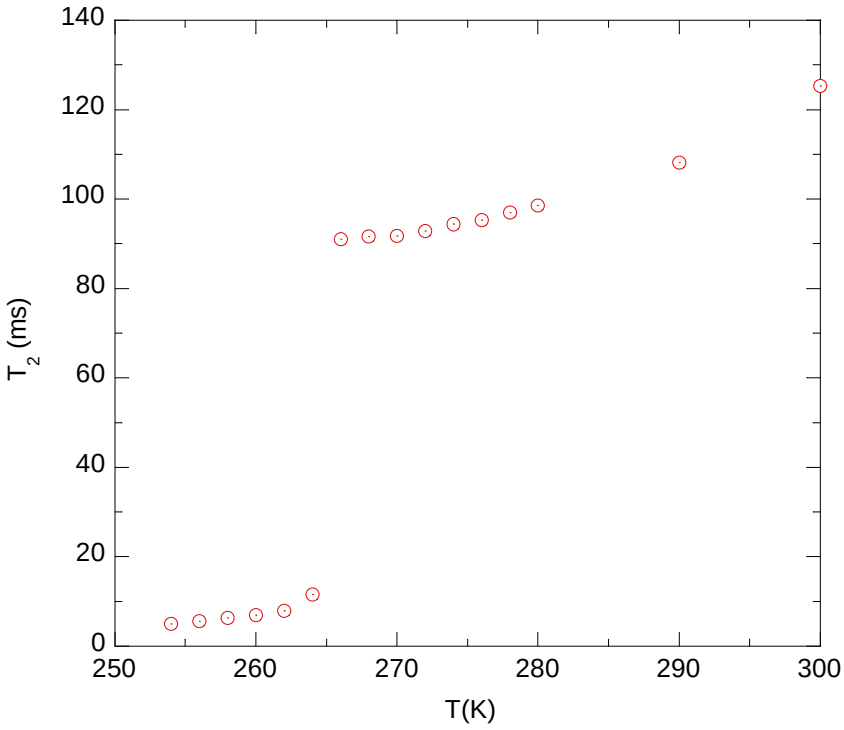

Fig. 4. Temperature dependence of the relaxation times of the water protons located in the pores of AN69 membrane

The free energy ΔG_C for the formation of a solid nucleus inside a sphere of radius r is calculated by simply adding the volume free energy of the nucleus and the free energy of the liquid-solid interface:

$$\Delta G_C = -\frac{4\pi r^3}{3} \cdot \Delta h_f \left(1 - \frac{T}{T_0}\right) + 4\pi r^2 \cdot \gamma$$

where Δh_f is the free enthalpy, T the temperature, T_0 the freezing point of the normal water and γ is the interfacial energy at water/wall interface.

At equilibrium, the radius is obtained from the condition $\frac{d\Delta G_C}{dr} = 0$. We obtain:

$$r = \frac{2\gamma}{\Delta h_f \left(1 - \frac{T}{T_0}\right)}$$

Taking the value of $\gamma = 62.55 * 10^{-4} \frac{J}{m^2}$ for the normal water and the value 333.627*10^6 J/m^3 for the heat of fusion of water molecules inside the pores of the polymeric membrane, we obtained the value of 5.5nm for the radius corresponding to the majority of pores.

CONCLUSION

The analyse of water molecules behaviour inside the AN69 polymeric membrane was made using proton NMR technique. An important change of the shape of the relaxation curves was observed around 265K. This effect was attributed to a change of water behaviour inside the pores, because the interactions betveen the water molecules and walls of the pores. The analyse of the values of the spin-spin relaxation time clearly indicates the existence of a transition process around this temperature. We associated this process with the liquid-solid transition.

The modification of the freezing point of the water inside the pores allowed us to estimate the mean size of the membrane pores. Supposing a spherical shape for the pores, we obtained a value of 5.5nm for the mean radius of the pores.

REFERENCES

1. K. Kaneto, ***J. Membrane Sci*.., 96**, 59 (1994).
2. K. Sakai, ***J. Membrane Sci*.., 96**, 91 (1994).
3. C. L. Jackson, G.B.McKenna, ***J. Chem.Phys*.,93**, 9002 (1990).
4. D. D. Awschalom, J.Warnock, ***Phys.Rev.B***, **35(13)**, 6779(1987).
5. M. C. Bellissent-Funel, J.Lal, L.Bosio, ***J.Chem.Phys***., **98(5),** 4246(1993).
6. R. Ravindra, K.R.Krovvidi, A.A.Khan, A.K.Rao, ***Polymer***, **40**,1159(1999).
7. S. Stapf, R.Kimmich, ***J.Chem.Phys***., **103(6)**,2247(1995).
8. B. MacMillan, A. R. Sharp, R. L. Armstrong, ***Polymer***, **40**,2471(1999).
9. J. P. Cohen-Addad, NMR and Fractal Properties of Polymeric Liquids and Gels, Pergamon Press, London (1992).
10. Alina Buda, J.P.Cohen-Addad, M.Todica, O.Cozar, ***Studia UBB***, Physica, XLIV, **1**(2000).

STUDIA UNIVERSITATIS BABEŞ-BOLYAI, PHYSICA, XLV, 2, 2000

THE QUANTITATIVE DETERMINATION OF ACTIVE PRINCIPLES FROM *HYPPOPHAË RHAMNOIDES L*. OIL BY GC/MS

CARMEN GHERMAN[1], MONICA CULEA[2], O. COZAR[1]

***ABSTRACT*.** The quantitative determination of Vitamin E from *Hyppophaë rhamnoides L.* oil is presented by using GC/MS method. The precision of the extraction method gave relative standard deviation lower than 3%. It has been used a regression curve with cholesterol as internal standard. The results showed that *Hyppophaë rhamnoides L.* oil contains 0.05% Vitamin E.

Introduction

Since some synthetic antioxidants have been found to be toxic to experimental animals, natural plant products began to receive much attention as sources of safe antioxidants. The main source of natural antioxidants is various kinds of plant products such as oil, seeds, cereals, beans, and nuts. Because plant seeds must retain germination ability for long-term preservation, they usually contain effective antioxidants in or around their germs [1].

The therapeutic activities of medicinal plants are gaved by "vegetal active principles" which are some organic compounds existing in plants. They are not depending by form of the plants, but are in strong correlation by the color, smell and taste of the plant source [2-8].

These compounds have the various chemical structures which explain the multiple therapeutic actions of plants**.** It is necessary to take care of their physical and chemical properties when a drug is prepared for a complete extraction of the active principles from plants; otherwise they can be destroyed in the extracting process with the diminution and even the loss of therapeutic activity.

Hyppophaë rhamnoides L plant is also called "the miracle herb", because the amount of the vitamins is very large. This plant is actually a

[1] "Babes-Bolyai" University, Cluj-Napoca
[2] S.C. "Natex" S.R.L., Cluj-Napoca

shrub, wide spread in Central Asia especially. The main part of this plant is the fruits, which are also called "a natural polyvitamin". It was proved the existence of some vitamin: A, B, C, E, F, P. Vitamin E is an antioxidant substance taking an important function in nutrition, cardiovascular diseases, and muscular, nervous and glandular system aging process and preventing coronary heart attacks [5].

The aim of this paper is the identification and determination of Vitamin E from *Hyppophaë rhamnoides L*. oil by using a gas chromatography-mass spectrometric method (GC/MS).

The saturated and unsaturated fatty acids measured as FAME (fatty acid methyl of esters) showed different values in pulps, seeds and integrals fruits [2].

Experimental

2.1. Materials

The vegetable oil of *Hyppophaë rhamnoides L*., was obtained by extraction in dichloroethane and the organic solvents: ethyl acetate, hexane, dichlormethane, cholesterol (the internal standard), were purchased from Chimopar-Bucharest and Vitamin E acetate (α-tocopherol acetate) was purchased from a local chemist's shop.

2.2. Instruments

A Hewlett Packard 6890 gas chromatograph (GC) with flame ionization detector (FID) and a Hewlett Packard 5989B mass spectrometer (MS) were used. A fused silica capillary column (HP-5MS), 30m x 0.32 mm, 0.25 μm film thickness was used in different temperature programs from 70°C with 20°C/min to 100°C, then 30°C/min to 300°C (15min) for Vitamin E determination. The injector and the detector temperature were 250°C and the flow rate of helium was 1ml/min.

The mass spectrometer was operated at electron energies of 70 eV, with 300μA emission current, the ion source temperature 200°C, and the analyzer temperature 100°C. The interface was kept at 280°C.

Results and discussion

The quantitative analysis of Vitamin E from *Hyppophaë rhamnoides L.* oil was determinate by GC/MS method. The *Hyppophaë rhamnoides L*. oil is very rich in unsaturated fatty acids also. We have analyzed as well the saturate and unsaturated fatty acids as FAME (fatty acid methyl esters).

Figure 1 shows the chromatogram obtained from injected of 0,5 μl *Hyppophaë rhamnoides L*. underivatized oil into chromatograph. It was

identified Vitamin E by comparison the obtained mass spectrum with Vitamin E mass spectrum from Wiley library (Fig. 2).

For Vitamin E determination a regression curve was obtained by using known quantites of Vitamin E acetate and the same quantity of 250μg cholesterol as internal standard.

We suppose the GC/MS response of Vitamin E and Vitamin E acetate are very similar. For this reason we have considered regression curve for Vitamin E acetate.

Vitamin E was determined by using a regression curve, with cholesterol as internal standard. The main molecular ions of cholesterol is 386 (m/z). The regression curve was build for different quantites of Vitamin E acetate and the same quantity of cholesterol. Figure 3 shows the chromatogram of the mixture: 250 μg cholesterol to 100 μg Vitamin E acetate.

The ratio m/z 430/386 representing the ratio between a characteristic ion of Vitamin E mass spectrum and the molecular ion of cholesterol (mass spectrum shown in figure 5(b)) was plotted against known quantities of Vitamin E acetate to obtain the regression curve.

The range of Vitamin E acetate in the regression curve was 0-250 μg to a constant quantity of 250 μg of cholesterol, the internal standard.

Figure 4 presents the regression curve, y=0.014x-0.20 and the correlation coefficient of r=0.99 which shows a good linearity. The relative standard deviation values (R.S.D.) for 50μg of Vitamin E (n=4) were lower than 11%.

0,05% of Vitamin E was calculated in *Hyppophaë rhamnoides L.* oil (n=3) by using the regression curve and cholesterol as internal standard.

The biological role of unsaturated fatty acids is more important than Vitamin E. The big quantity of palmitoleic acid in *Hyppophaë rhamnoides L* are very usefull for skin protection and explain their large use in cosmetics. They are carcinogenic and antioxidants. The large amount of unsaturated fatty acids and their quality explain the biological role of *Hyppophaë rhamnoides L.*

The most important fatty acids found in the fruits are polyunsaturated fatty acids (palmitoleic acid, linoleic acids, oleic acid) known as Vitamin F. (table 1).

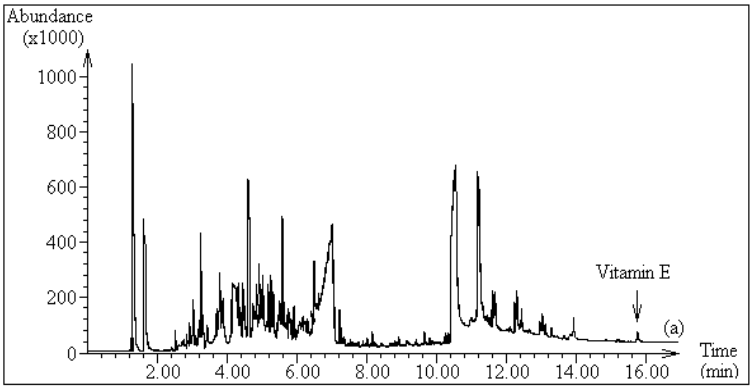

Fig.1 The chromatogram of Hyppophae Rhamnoides L. oil

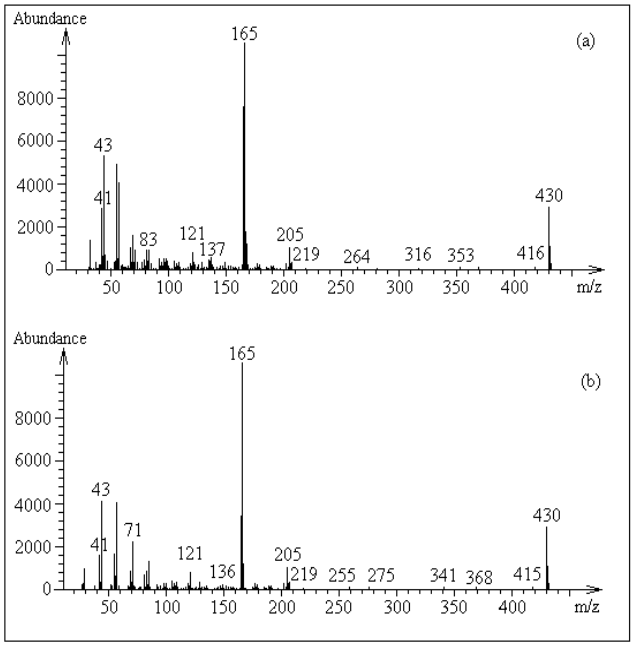

Fig.2 Mass spectra of Vitamin E from Hyppophae Rhamnoides L.oil(a) and Vitamin E mass spectra from the library spectrum (b)

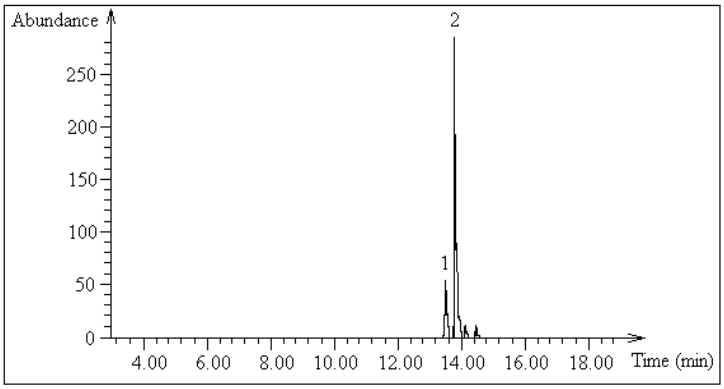

Fig.3 The chromatogram of the mixture of known quantities of cholesterol and Vitamin E acetate. (1-cholesterol, 2-Vitamin E acetate)

m/z (430/386) Vitamin E / cholesterol Y=0.0014X-0.20 r =0.990

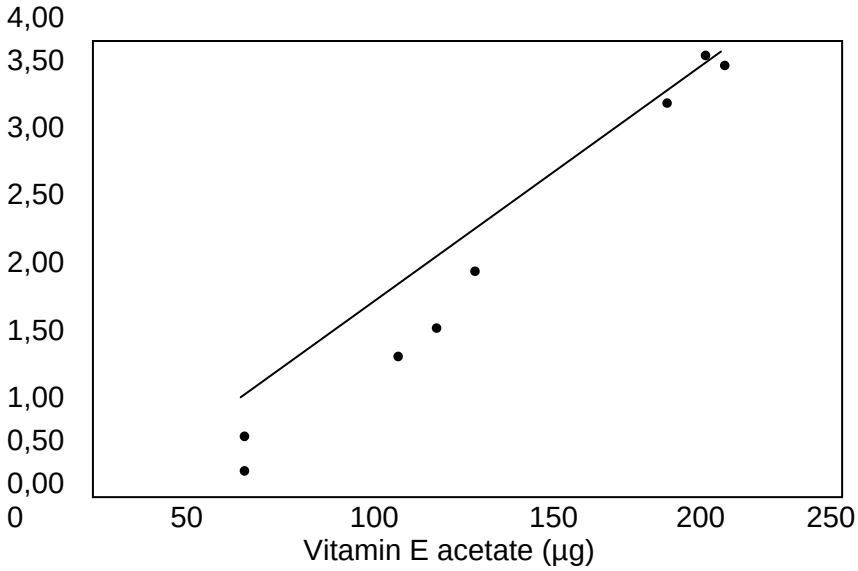

Fig. 4. The regression curve for determination of Vitamin E quantity in *Hyppophaë rhamnoides L* oil.

Table 1

FAME (fatty acids methyl esters)			
Nr. crt.	Compounds	t_R	MS(%)
1	Methyl myristate (C14:0)	13.2	0.4
2	Methyl palmitoleate (C16:1)	15.71	27.7
3	Methyl palmitate (C16:0)	16.01	35.1
4	Methyl heptenoate (C17:1)	16.8	0.1
5	Methyl linoleate (C18:2)	18.0	2.0
6	Methyl oleate (C18:1)	18.07	33.7
7	Methyl stearate (C18:0)	18.25	1.0

The fatty acids from *Hyppophaë rhamnoides L.* oil were analysed after methylation as fatty acids methyl esters (FAME). Derivatization was made at 60℃ for 1 hour, using 3M methanol 1HCl (methano l:acetyl chloride 5:1).

Conclusions

The analitical methods GC and GC/MS are suitable for the quantitative analysis at trace levels. Good linearity and precision were obtained for Vitamin E determination.

The results show that *Hyppophaë rhamnoides L.*oil contains 0,05% Vitamin E which is an antioxidant and takes an important function in nutrition, cardiovascular diseases, and aging processes. The correlation factor r=0.99 and precision of measurements gave a relative standard deviation of 13 % for Vitamin E determination and 20% for unsaturated fatty acids determination from *Hyppophaë rhamnoides L* oil. Unsaturated fatty acids are the most important compounds in the studied plant and explain it name of "the miracle plant".

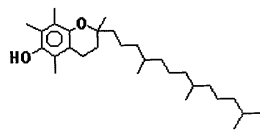

Vitamin E

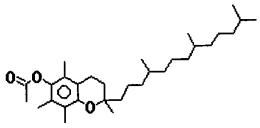

Vitamin E acetate

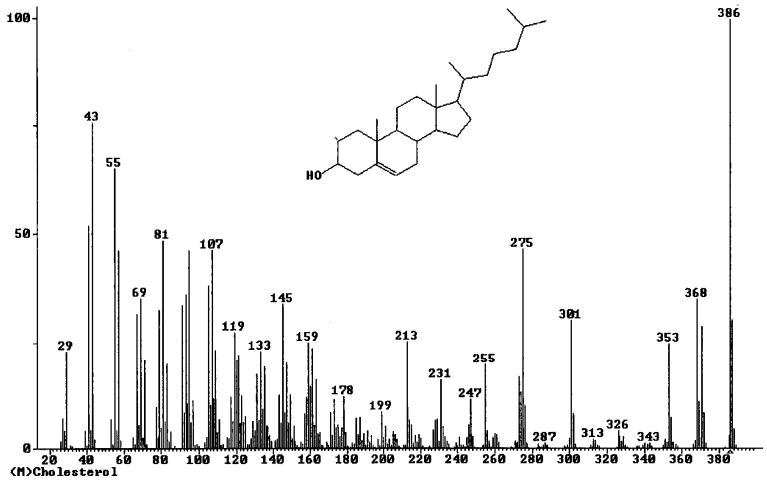

Fig. 5 (a) Vitamin E and Vitamin E acetate chemical formula
(b) Chemical formula and mass spectrum of cholesterol

REFERENCES

1. M. N. Malik, M. D. Fenko, A. M. Shiekh, H. M. Wisniewski- *J. Agric. Food Chem.* 45, 817 (1997).
2. U. Stănescu, R. Morar, G. Neamțu, E. Morar - *Cercetări fitochimice asupra speciei Hyppophaë rhamnoides L.,* Buletinul Institutului Agronomic Cluj-Napoca, seria ZMV, 43, 41 (1989).
3. J. Parcerisa, D. G. Richardson, M. Rafecas, R. Codony, J. Boatella-*Journal of Chromatography A*, 805, 259 (1998)
4. A. von Gadow, E. Joubert, C. F. Hansmann-*J. Agric. Food Chem.* 45, 632 (1997).
5. S. W. Huang, E. N. Frankel, K. Schwarz, J. B. German- *J. Agric. Food Chem.* 44, 2496 (1996).
6. G. Neamțu, U. Stănescu – "*Achievments and perspectives in the Romanian biochemical researche", Cercetări biochimice privind valorificarea unor polivitamine naturale I, pigmenți carotenoidici, acizii graşi şi lipidele totale din patru tipuri morfologice de fructe de Hyppophaë rhamnoides L.,* Symposium "Academical Days of Cluj" 6 December 1989, Academy of Romania, Cluj, pp.1-31.
7. T. Miyake, T. Shibamoto- *J. Agric. Food Chem.* 45, 1819 (1997).
8. Carmen Gherman, Monica Culea, O. Cozar- Talanta 53, 253 (2000).

STUDIA UNIVERSITATIS BABEŞ-BOLYAI, PHYSICA, XLV, 2, 2000

UV RADIATION EFFECTS ON A NEW HYDRAZINO-CARVONE COMPOUND. AN ESR INVESTIGATION.

Abbreviated title: ESR ON UV-IRRADIATED HYDRAZINO-CARVONE

I. BARBUR[1], V.CHIŞ[1], I.BÂTIU[2]

ABSTRACT. The effect of UV-irradiation on a new compound resulting from condensation of hydrazine derivat 2-hydrazino-4hydroxy-6-methylpyrimidine with carvone is reported. The UV induced free radicals are produced by hydrogen abstraction from the C5 carbon atom of the pyrimidinic ring, the unpaired electron being in a highly delocalized orbital. In contrast to gamma-irradiation, the concentration of the UV-induced free radicals is quite rapidly decreasing at room temperature and it is accompanied by the change in color of the sample.

Keywords: UV-irradiation, free radicals, hydrazino-carvone compound

Introduction

The aim of this work was to continue the investigation of the effect of different electromagnetic irradiation on some hydrazine derivates containing the pyridinic or pyrimidinic nuclei in their molecules and on new compounds resulting from the condensation of the hydrazine derivates with terpenoids. This class of compounds is present in some natural products and investigation of their radiolysis products is of interest for radiation processing and sterilization in food and drug production.

In our previous paper (Barbur et al., 1995) an ESR study of gamma-irradiation effect on some hydrazine derivates containing the pyridinic or pyrimidinic nuclei in their molecules: hydrazide of isonicotinic acid, 2-hydrazino-4hydroxy-6-methylpyrimidine, and 2-hydrazino-5-butyl-4-hydroxy-6-methyl-pyrimidine was reported. From condensation of these hydrazine derivates with terpenoids: verbenone, carvone and citral, new condensation products were obtained (Bâtiu 1995) with an important biological activity.

[1] Babeş-Bolyai University, Faculty of Physics, RO-3400 Cluj-Napoca, Romania
[2] Babeş -Bolyai University, Faculty of Chemistry and Chemical Engeneering, RO-3400 Cluj-Napoca, Romania

In this study, we have used 2-hydrazino-4-hydroxy-6-methylpirimidine as hydrazine derivat. From condensation of this sample with carvone, a new condensation product was obtained, according to the reaction given in Fig.1. This new product was exposed to UV-irradiation at different doses.

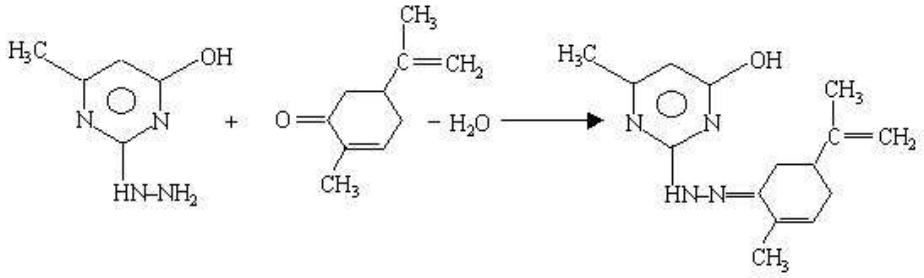

Fig.1. Reaction scheme of producing the condensation compound

Experimental

Both hydrazine derivat (powder form) and carvone (liquid form) were obtained from Bruder Unterweger GmbH&Co and used in the highest available purity (99.9%). ESR spectra were recorded using a JEOL-JES-3B modified X-band spectrometer. The instrument setting were: microwave frequency 9500 MHz, modulation frequency 100 KHz, field scan 200 G, time constant 1 s, cavity TE_{102}, sensitivity $3 \cdot 10^{11}$ spins/gauss and microwave power 10 mW. The calibration of magnetic field for g factor and hyperfine splitting values was performed by using NMR signal of protons (NMR magnetometer of MJ110R type).

The ESR spectrum was simulated using a spin Hamiltonian that contains a g-tensor and up to ten hyperfine tensors for a radical. The program generates the powder pattern by means of Gauss-Legendre numerical quadrature. ESR spectrum is then obtained by convoluting the powder pattern with Lorentzian or Gaussian lineshape functions of convenient widths. More spectra of different radicals can be added together in various ratios.

The new condensation compound sample was used in power form and exposed to UV-irradiation from a conventional source, at room temperature.

Results and discussion

ESR spectra of UV-irradiated condensation compound were recorded at different irradiation times and they do not show qualitative changes by increasing the radiation dose, suggesting that only one type of radicals is formed. These spectra with a total extent of about 40 G are dominated by a central line centered at g=2.0072 which split into poorly resolved hyperfine structure (Fig.2).

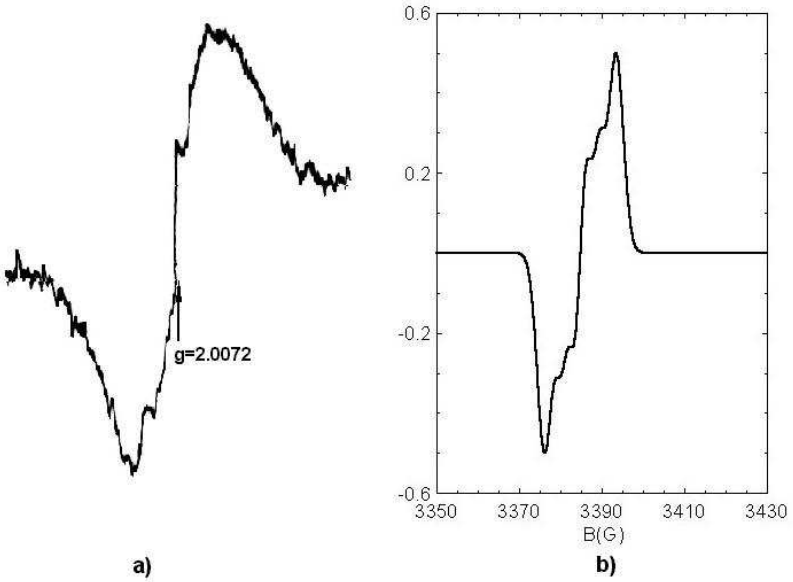

Fig.2. Experimental **(a)** and simulated **(b)** ESR spectra of UV-irradiated condensation compound. Irradiation time was 110 minutes

As mentioned above, the same sample, but gamma-irradiated was the subject of an ESR investigation (Barbur et al. 1995). In that work it was concluded that the γ-induced free radicals are formed by hydrogen abstraction from the nitrogen atom bonded to the C2-carbon atom of the pyrimidinic ring. Corresponding experimental ESR parameters do not fit the ESR spectrum of the UV-irradiated sample so it is clear that another type of radicals are formed in this case.

The spectrum given in Fig.2.a shows a poorly resolved hyperfine structure, which can be interpreted in terms of two triplets of equal size, with small splitting of about 3.6 G, suggesting a π-type radical (Close et al. 1988). The only nuclei, which could give such splittings, are those of ^{14}N. Moreover, the corresponding coupling constant is in a very good agreement

with the isotropic coupling constant in the lumiflavin semiquinone anion (Wertz and Bolton, 1989). Hence the unpaired electron is considered to interact with two nitrogen atoms, N1 and N3. Such interactions would be observed if the radiation removed the hydrogen atom attached to the carbon C5 atom to produce the free radical of the structure given in Fig.3.

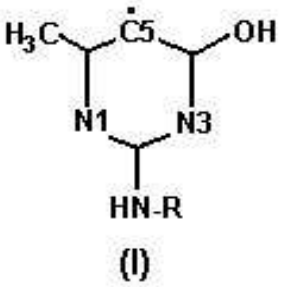

(I)

Fig.3. The structure of the free radical produced by UV-irradiation of the hydrazinocarvone condensation compound at room temperature

The other resonances bond structures possible to be formed from (I) show that the unpaired electron spin density should appear on carbon atoms which does not have a magnetic moment and so will not contribute to the ESR spectrum or on the nitrogen atom bonded to the C2 carbon atom of the ring. In the last case, if appreciable spin density appeared on this atom then the spectrum would have been greatly complicated by additional splittings from interactions with this nucleus and the attached hydrogen atom.

Furthermore, another kind of free radicals, produced by hydrogen addition at one of the carbon atoms of the ring are generally reported for compounds containing aromatic rings (Close et al. 1988, Close and Nelson 1989, Cook at el. 1967, Cozar et al., 1997, Sagstuen et al. 1988). However, in our case there is no evidence for this kind of radicals since they should exhibit large splittings from -hydrogens.

The experimental spectrum given in Fig.2.a was simulated assuming that it is due the radical (I) with equal N1 and N3 splittings. The best agreement between the simulated spectrum (Fig.2.b) and the experimental one was obtained based upon the following parameters: $A_{N2}=A_{N4}=3.57$ G, g=2.0072, $\Delta H_{pp}=2.35$ G. Hence, the unpaired electron probably occupies a highly delocalized orbital, the splittings arising from unpaired spin densities on two central nitrogen atoms.

With a Q value of -28.6G in the McConnell relation the unpaired spin densities on N2 and N4 were calculated to be 0.125, in very good

agreement with other reported values corresponding to the nitrogen atoms in similar free radicals (Close et al., 1988, Close and Nelson 1989, Sagstuen et al., 1988).

It has to be mentioned that no ESR signal was obtained from UV-irradiated hydrazine derivat 2-hydrazino-4-hydroxy-6-methylpirimidine.

The concentration of the UV-induced free radicals is proportional to the ESR signal amplitude (peak-to-peak relative to the central line) and as shown in Fig.4 it is rapidly increasing by increasing the UV absorbed dose. It may be observed that no saturation of the free radical concentration is reached after two hours of exposure to UV irradiation. This is in contrast with some results reported by Gibella *et al.* (Gibela et al., 1994) regarding the accumulation of the UV-induced free radicals in other molecular solids.

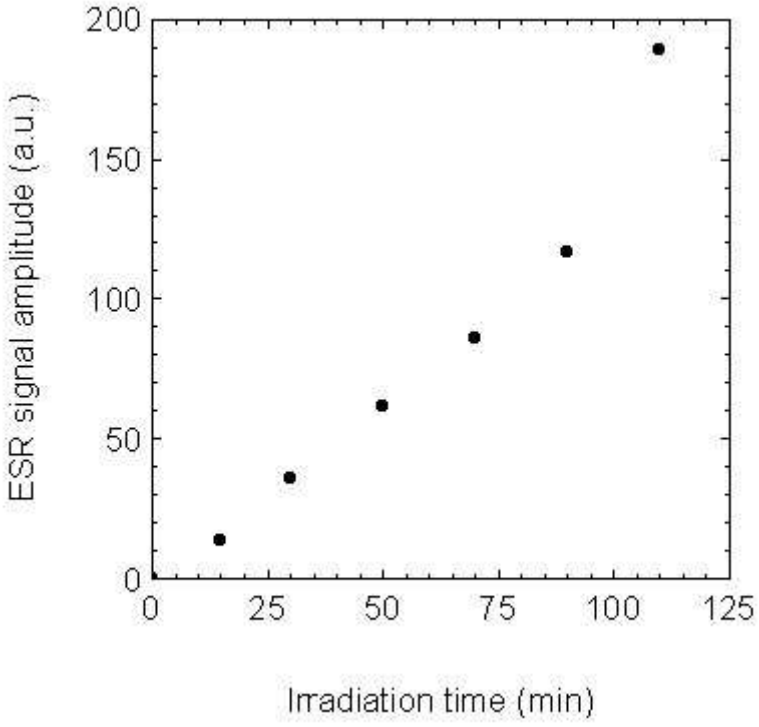

Fig.4. ESR signal amplitude as a function of UV-irradiation time.

Moreover, the UV-induced free radicals are nor stable paramagnetic species at room temperature due to their recombination process. In addition, the decreasing of the free radical concentration is accompanied by the change in color of the sample, from white to yellow. This process could be due to the photolysis of the carvone complex induced by UV radiation or

to intramolecular photocycloaddition of carvone complex as it was reported in other studies (Malatesta et al., 1982). Relative decreasing of the concentration of the free radicals (Fig.5) was estimated by the ESR signal amplitude attenuation with time after UV-irradiation.

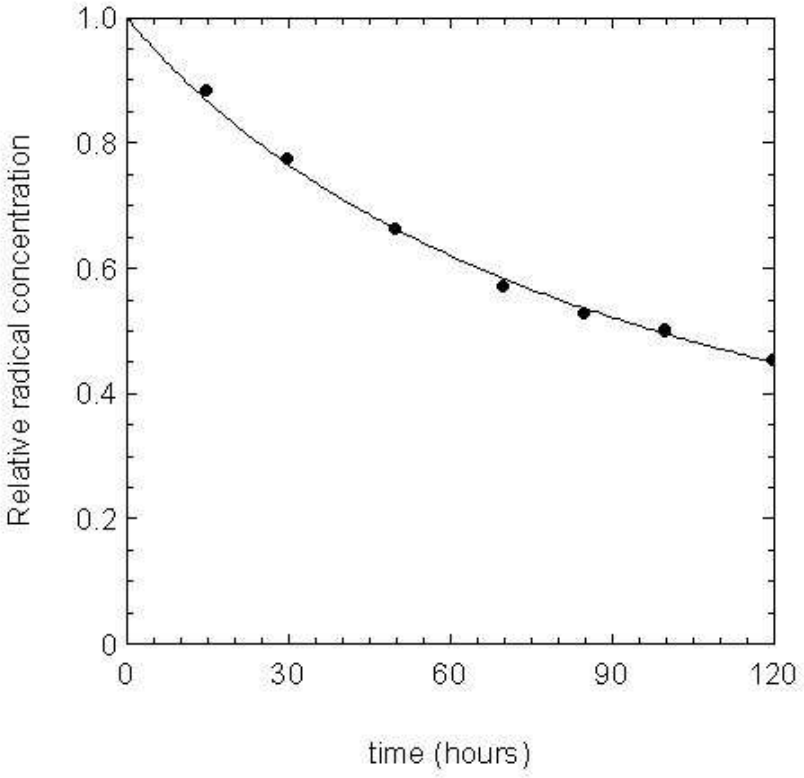

Fig.5. Decay of the ESR signal amplitude as a function of time after UV-irradiation. The continuos line represents the best-fit calculated values.

Experimental data shown in Fig.5 were fitted by a function given by: (Pchjetckii et al., 1972)

$$\frac{1}{R} - \frac{1}{R_0} = kt \qquad (1)$$

where R_0 is the initial concentration of the free radicals, R is the concentration at a time t and k is the rate constant. A value of $2.8 \cdot 10^{-6}$ was obtained for k, in good agreement with other values corresponding to free radicals in solid state (Pchjetckii et al., 1972).

Conclusions

The shape of the ESR spectrum corresponding to the UV irradiated hydrazino-carvone compound doesn't change by increasing the irradiation dose, suggesting that only one radical is produced by UV rays in this sample at room temperature. The free radicals are formed by hydrogen abstraction from the C5 carbon atom of the pyrimidinic ring and the unpaired electron has a coupling constant of about 3.6 G with the two nitrogen atoms of the ring.

The rate constant of the free radicals recombination process is in good agreement with other values corresponding to the free radicals in solid state.

REFERENCES

1. Barbur, I., Bâtiu, I., Simon, V., 1995. ESR Study of free radicals in some new hydrazones of terpenoids class. Journal of Radioanalytical and Nuclear Chemistry, Articles, 196, 153-160.
2. Bâtiu, I., 1995. Ph.D. Thesis, "Babeş-Bolyai" University, Cluj-Napoca, Romania.
3. Close, D.M., Nelson, W.H., 1989. ESR and ENDOR study of adenosine single crystals X-irradiated at 10 K. Radiation Research, 117, 367-377.
4. Close, D.M., Sagstuen, E., W.H.Nelson, W.H., 1988. Radical formation in X-irradiated single crystals of guanine hydrochloride monohydrate. Radiation Research, 116, 379-392.
5. Cook, J.B., Eliot, J.P., Wyard, S.J., 1967. Electron spin resonance of an irradiated single crystal af cytosine. Molecular Physics, 13, 49-64.
6. Cozar, O., Chiş, V., David, L., Damian, G., Barbur, I., 1997. ESR investigation of gamma irradiated aspirin. Journal of Radioanalytical and Nuclear Chemistry, 220, 241-244
7. Gibella, M., Pronce, T., Tilquin, T., 1994. Etude RPE de medicaments ionises et photolyses. Journal de Chimie Physique, 91, 1868-1872.
8. Malatesta, V., Willis, C., Hackett, P.A., 1982. Laser-induced cycloadditions: the carvone photoisomerization. Journal of Organic Chemistry, 47, 3117-3121.
9. Pchejetckii, C.I., Kotor, A.G., Milinciuc, V.K., Roginskii, B.A., Tyrikov, V.I., 1972. EPR svobodnih radicalov v radiationoi himii, Moskva Izdatelstvo Himia, pp.339.
10. Sagstuen, E., E.O.Hole, E.O., W.H.Nelson, W.H., D.M.Close, D.M., 1988. ESR/ENDOR study of guanosine 5'-monophosphate (free acid) single crystals X-irradiated at 10 K. Radiation Research, 116, 196-209.

STUDIA UNIVERSITATIS BABEŞ-BOLYAI, PHYSICA, XLV, 2, 2000

STRUCTURAL CHARACTERIZATION OF CdSe:In EPITAXIAL LAYERS

G. CERBANIC[1], S. SIMON[1], P. GASHIN[2], A. FOCSHA[2], C. ROTARU[2]

***ABSTRACT*.** The CdSe:In layers have been deposited on (001) oriented mica substrates by vapor phase transport method. Information about growth conditions structure and the crystalline quality has been obtained from micrographs and X-ray diffraction (XRD) analyses.

Introduction

Due to their high photosensitivity and high luminescence quantum efficiency, the thin layers of CdSe semiconductor compounds are very attractive for the manufacturing of solar cells [1,2]. Such epitaxial layers with monocrystal properties are of great interest [3-6]. As these compounds are polymorph materials, it is important to know the growth conditions of homogeneous and oriented epitaxial layers.

The paper reports the influence of growth conditions on the structure and the morphology of the CdSe:In layers.

Experimental

The CdSe layers were grown onto (001) oriented mica substrates by vapor phase transport method at a remanent gas-pressure of $2 \cdot 10^{-5}$ torr. The vapor phase transport method consists in the transport of source material from the region with high temperature, where CdSe thoroughly dissociates in Cd and Se atoms, to the region with low temperatures, due to the temperature gradient. Information on layers structure and crystal quality were obtained from the analysis of optical micrographs obtained by means of a metallographic microscope MMR-2R and X-ray diffraction patterns of the samples recorded with a Dron 2 type diffractometer (λ=0.154nm).

[1] Babes-Bolyai University, Faculty of Physics, 3400 Cluj-Napoca, Romania
[2] State University of Moldova, Faculty of Physics, 2009 Chisinau, Republic of Moldova

Results and discussion

The scheme of the equipment used to obtaine CdSe:In layer samples in presented in Figure 1.

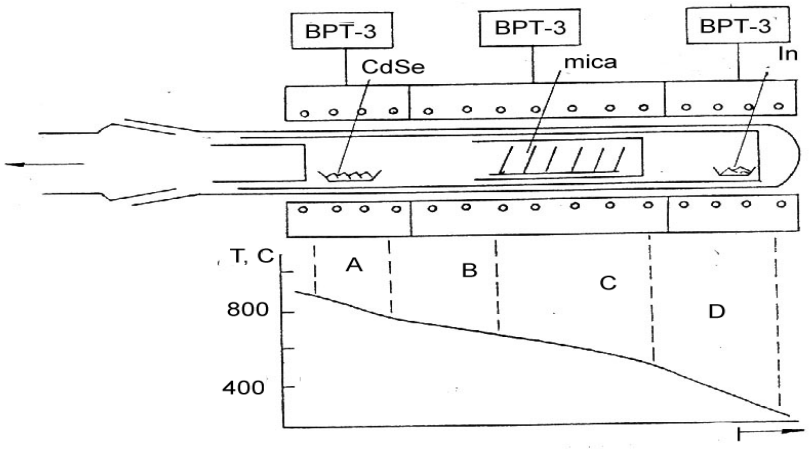

Fig.1. Scheme of the epitaxial growth equipment.

A quartz tube with a diameter of 60 mm was used as reactor, being connected to the vacuum system. The source, CdSe powder, and the mica substrate are loaded here. The quartz tube is disposed in horizontal position in an electric oven, where four temperature regimes are developed, as illustrated in Figure 1. The range denoted with A corresponds to source's high temperature region (780-800)°C, B corresponds to mixing temperature region (780-660)°C, C to deposition region (660-538)°C and D to impurities doping region (250-300)°C. The oven is provided with wheels, which allow to select any temperature region from A to D along the quartz tube. After evacuating the quartz tube up to a pressure of $5 \cdot 10^{-5}$ mm/Hg and installing the desired temperature, the oven is planed in the working regime. The supply of the oven is ensured by BPT-3 device, which maintains a constant temperature with a precision of $\pm 0.5^{o}$C. The temperature value is controlled by a platinum-platinum-rhodium thermocouple.

During the evaporation, CdSe dissociates according to the equation [7]:

$$CdSe_{(sol)} \Leftrightarrow Cd_{(vap)} + \frac{1}{2} Se_{2(vap)} \qquad (1)$$

Due to the temperature gradient in vapor phase Cd and Se_2 are transported from region A to region B. The doping impurity In is transported from the region of doping impurities D, to mixing region B. Thus, in B region, the vapor fluxes of Cd, Se_2 and In mix together and they are transported to C region, where the deposition of CdSe:In layers takes place. The concentration of doping impurity depends on source temperature in the D region. The epitaxy time and the substrate temperature are changed according to the desired thickness of the layer. As evaporation sources were used CdSe polycrystals heated at 800°C.

In Figure 2 are presented the micrographs of the surface of CdSe layers grown on (001) oriented mica at various substrate temperatures. The micrographs show that growth figures observed on the surface of CdSe are regular hexagons or cut off hexagonal pyramids. On the other hand, the micrographs clearly demonstrate a complex correlation between the crystalline quality of the layers and the deposition quality temperature. Thus, the size of the crystallites increased from 30 μm to 60 μm and their density decreased from $8 \cdot 10^4$ cm^{-2} to $2.5 \cdot 10^4$ cm^{-2} (Fig.2 a,c) when the deposition temperature varied from 672°C to 565°C. As the temperature was furtherly reduced to 542°C, the crystallites site diminishes to 2-4 μm and their density increases to $4 \cdot 10^6$ cm^{-2} (Fig.2 d).

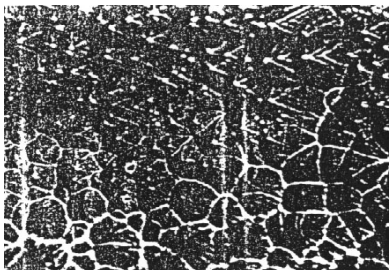

a)

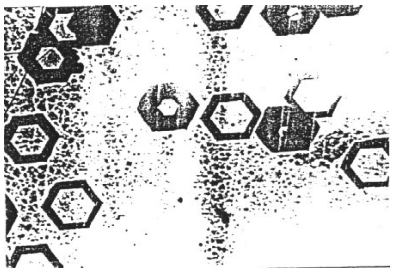

b)

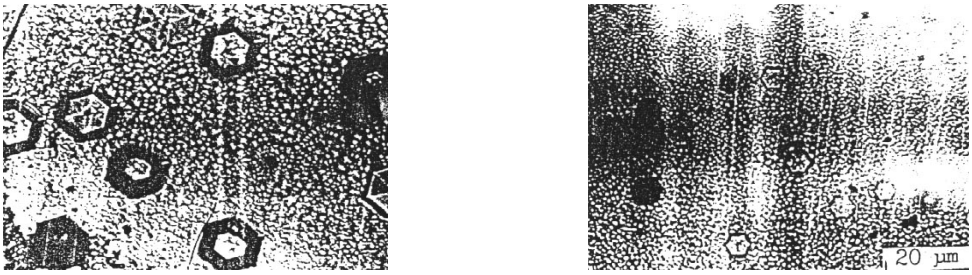

c) d)

Fig. 2. Optical micrographs of CdS epitaxial layers obtained at various substrate temperatures
a) 672°C, b) 584°C, c) 565°C, d) 542°C.

One remarks from Figure 2 that the optimum growth temperature is 584^{o}C, at which the growth figures have clear edges. This means that the growth of crystallites occurs according to vapor-crystal mechanism [8]. The hexagonal growth patterns obtained for the investigated CdSe:In layers correspond to (001) plane that is, from structural point of view, characteristic to CdSe hexagonal modification.

The obtained results indicate that the deposition rate of the CdSe layers strongly depended on substrate temperature and varied from 0.02 to 0.5 µm/min for substrate temperatures ranging from 672°C to 542°C.

Figure 3 shows the X-ray diffraction pattern of CdSe:In layer grown at 584°C.

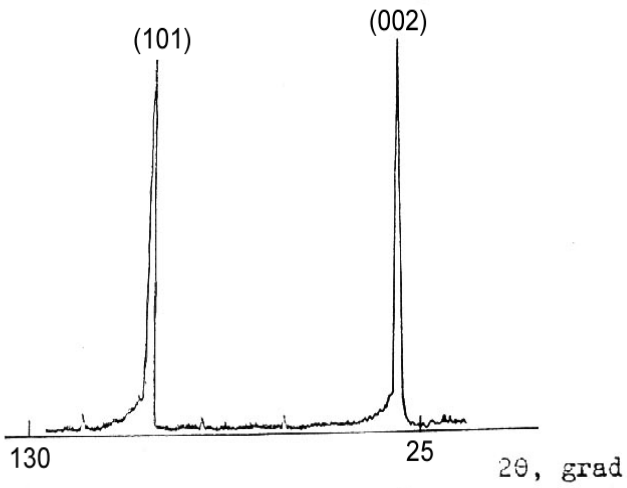

Fig. 3. X-ray diffraction patterns of CdSe:In.

The maximum diffraction intensities in this case correspond to (002) and (101) reflexion plane, which indicate that the growth of crystallites from CdSe layers correspond to hexagonal modification [9].

Conclusions

CdSe:In layers were grown onto (001) oriented mica substrates by vapor phase transport method. The micrographs recorded from the surface of CdSe layers show that the grown crystallites are regular hexagons with clear edges as the growth temperature is 584^{o}C. The XRD data also support the CdSe hexagonal structure for CdSe:In layers obtained at this optimal grown temperature.

REFERENCES

1. M. Usman Kham, Shahzad Naseem, M. Iqbal Munawwar and E. M. Nazar, Modern Physics Letters B, Vol. 13, No. 26 (1999) 953-959.
2. Fizica soedinenii $A^{II}B^{VI}$, Nauka Publishing House, Moscow, 1986.
3. D.M. Basko, V.M. Agranovich, F. Bassani, G.C. La Rocca, Eur. Phys. J. B 13, 4, 653-659 (2000).
4. S. Pokrant, K.B. Whaley, Eur. Phys. J. D 6, 2, 255-267 (1999).

5. Shang-Fen Ren and Jason Stanfield, International Journal of Modern Physics B, Vol. 12, Nos. 29, 30 & 31 (1998) 3137-3140.
6. Kalinkin I.P., Aleskovsky V.B., Simashkevich A.V., $A^{II}B^{VI}$ Epitaxial Films, Leningrad, 1978.
7. Verbitskii O.P., Koseacenko P.A., Mahnii V.P., Rijikov V.D., Svoistva sistemi stintileator-fotodiod na osnove structuri selenid-tellurid zinca. //Pisima v JTF. –1988.- T.14., vip. 8.
8. Aleksandrov L.N., Growth and Doping of semiconductor Crystals and films, pp.5, Novosibirsk ,1977.
9. Mirkin L.I., Spravocinic po rentghenostructurnomu analizu policristalov. M. izd. Fiz. Mat. Literatura. 1961.